TEC | Tecnológico de Costa Rica

UNA Universidad Nacional Costa Rica

UNED Universidad Estatal a Distancia

DOCINADE
Doctorado en Ciencias Naturales para el Desarrollo
Énfasis en Tecnologías Electrónicas Aplicadas

Doctoral Thesis

A port-Hamiltonian system modelling approach and passivity-based nonlinear control design for photovoltaic energy harvesting

Hayden Anthony Phillips Brenes

Dr. Roberto Pereira Arroyo
Director de Tesis

Dr. Mauricio Muñoz Arias
Asesor de Tesis

Dr. Renato Rímolo Donadío
Asesor de Tesis

Cartago, Costa Rica, October 4, 2023

MIEMBROS DEL TRIBUNAL EXAMINADOR

Dr. Víctor Granados Fernández
Representante de la Coordinación General de DOCINADE

Dr. Saúl Guadamuz Brenes
Representante de la Dirección de Posgrados TEC

Dr. Roberto Pereira Arroyo
Director de tesis

Dr. Mauricio Muñoz Arias
Miembro del Comité Asesor

Dr. Renato Rímolo Donadío
Miembro del Comité Asesor

Declaración de Autenticidad

Yo Hayden Anthony Phillips Brenes, estudiante del Doctorado en Ciencias Naturales para el Desarrollo, declaro que la Tesis Doctoral que presento para su exposición y defensa titulada "A port-Hamiltonian system modelling approach and passivity-based nonlinear control design for photovoltaic energy harvesting" y comité asesor de tesis son el Dr. Roberto Pereira Arroyo (director de tesis), Dr. Mauricio Muñoz Arias (asesor), y el Dr. Renato Rímolo Donadío (asesor), es original y que todas las fuentes utilizadas para su realización han sido debidamente citadas en el mismo. Este material no lo he presentado, en forma parcial o total, como una tesis en esta u otra institución.

Heredia, Costa Rica a 26 de julio de 2023.

Hayden Anthony Phillips Brenes

"En cuestiones de cultura y de saber, solo se pierde lo que se guarda; solo se gana lo que se da"
Antonio Machado

Dedications

To Jackeline and André, my family, for being the driving force behind this project...

Acknowledgments

Thanks to the Doctorado en Ciencias Naturales para el Desarrollo (DOCINADE) program for allowing me to pursue this advanced postgraduate degree.

Thank the Instituto Tecnológico de Costa Rica for their financial assistance.

All my gratitude to Dr. Roberto Pereira Arroyo, Dr. Mauricio Muñoz Arias, and Dr. Renato Rímolo Donadío, my supervising and reading team, for their invaluable advice, which contributed to the success of this project.

Thanks to the University of Groningen's research group of Discrete Technology and Production Automation (DTPA), led by Prof.Jacquelien Scherpen, for the opportunity and support provided during my internship.

I want to thank the Unidad Desconcentrada de Ingeniería Electrónica, Campus Tecnológico San Carlos, for their support and for granting me access to their laboratory resources.

I sincerely appreciate the support of all the participants of the clean energy research project developed in Unidad Desconcentrada de Ingeniería Electrónica, Centro Académico de Alajuela, to which this thesis belongs.

I would like to express my gratitude to Dr. Dunstano del Puerto Flores and Dr. Pablo Borja Rosales for their valuable feedback during the various stages of my thesis development.

Finally, thanks to my family, friends, and collaborators for making this project a reality.

Abstract

This work involves designing and evaluating novel nonlinear control laws to solve the maximum power point tracking and voltage regulation problems by governing a DC-DC converter stage's switching states that connect a photovoltaic cell system to a consumption load.

To design the mathematical model of the systems, we utilize the port-Hamiltonian framework energy-based approach. To verify the capabilities of the port-Hamiltonian framework in terms of its simplicity, reflected in the physical interpretations of the mathematical structure, we propose the design of a nonlinear model of a multi-physical solar-powered pumped-hydro storage system that consists of a photovoltaic cell stage, a DC-DC buck converter, an electrical pump, and a recovery pipe that impulses water into a storage reservoir.

This system interconnects three different physical domains: electrical, mechanical, and hydraulic; hence, it becomes a suitable case to demonstrate that the port-Hamiltonian framework can display the interconnection between the physical stages transparently, allowing to identify quick the equivalent physical parameters, the state variables, and the energy dissipation and storage elements. The designed pumped-hydro storage system model is validated by simulation under several DC-DC converter switching state fluctuations.

Moreover, nonlinear control strategies are proposed and evaluated based on the transparency of the port-Hamiltonian framework modeling. Firstly, a photovoltaic cell stage connected to a DC-DC boost converter to feed a resistive load is designed and controlled to solve the maximum power point racking issue. We propose an interconnection and damping assignment passivity-based control strategy in electrical current monitoring sensorless topology to give a non-invasive control solution. We evaluate its performance against a Sliding Mode Control strategy via simulation. Furthermore, the system is implemented in a simple controlled physical prototype.

Finally, we design a double-switching, highly nonlinear control law to solve the maximum power point tracking and voltage regulation issues of a system that interconnects a photovoltaic cell stage to a battery load across the DC-DC buck-boost own design converter.

Once more, we utilize the port-Hamiltonian framework and the interconnection and damping assignment passivity-based control strategies to design the system model and the control stage. The design is implemented in a prototype and validated in terms of power consumption efficiency by comparing its performance against a commercial device.

The interconnection and damping assignment passivity-based control strategy was selected as it can shape the potential and kinetic energy function without relying on Casimir functions or overcoming the dissipation obstacle while preserving the port-Hamiltonian attributes. Hence, this strategy is suitable for reaching global stability in photovoltaic cell systems.

Resumen

En este trabajo se diseñan y evaluan nuevas leyes de control no lineal para el rastreo del punto de máxima potencia y la regulación de voltaje, mediante el control de los estados de conmutación de una etapa de convertidor DC-DC, que interconecta un sistema de celdas fotovoltaicas a una carga de consumo de energía.

El modelo matemático de los sistemas se diseña bajo el enfoque energético del marco port-Hamiltoniano, cuya simplicidad para las interpretaciones físicas de la estructura matemática es verificada a través del diseño de un modelo no lineal de un sistema multifísico de almacenamiento hidroeléctrico por bombeo alimentado con energía solar, que consiste en una etapa de celda fotovoltaica, un convertidor reductor DC-DC, una bomba eléctrica y una tubería de recuperación para transportar el agua hacia un depósito de almacenamiento.

En este sistema se interconectan tres dominios físicos: el eléctrico, el mecánico y el hidráulico, siendo este es un caso idóneo para demostrar como el marco port-Hamiltoniano exhibe la interconexión entre las etapas de forma transparente, permitiendo identificar fácilmente los parámetros físicos del sistema, las variables de estado, y los elementos de disipación y almacenamiento de energía. El modelo diseñado del sistema de almacenamiento hidroeléctrico por bombeo es validado mediante simulación, reflejando los efectos de fluctuaciones de los estados de conmutación del convertidor DC-DC sobre otras variables del sistema.

Además, se proponen y evalúan estrategias de control no lineal que se basan en la transparencia del modelo del marco port-Hamiltoniano. Primeramente, se diseña y controla el rastreo del punto de máxima potencia de una etapa de una celda fotovoltaica conectada a un convertidor elevador DC-DC que alimenta una carga resistiva. Se propone una estrategia de control basado en pasividad por transferencia de interconexión y amortiguamiento, sobre una topología sin sensores de corriente eléctrica, convirtiéndose en una solución de control no invasiva. Su rendimiento es evaluado al compararlo mediante simulación con una estrategia de control de modo deslizante. Además, el sistema es implementado en un prototipo físico con una plataforma sencilla.

Finalmente, se diseña una ley de control de doble conmutación altamente no lineal, tanto para el rastreo del punto de máxima potencia como para la regulación de voltaje de un sistema que interconecta una celda fotovoltaica a una batería de carga, a través de un convertidor reductor-elevador DC-DC de diseño propio.

Nuevamente, se utiliza el marco port-Hamiltoniano y la estrategia de control basado en pasividad por transferencia de interconexión y amortiguamiento, para diseñar el modelo del sistema y la etapa de control. El diseño se implementa en un prototipo y se valida en cuanto a eficiencia energética, comparando su desempeño con un dispositivo comercial.

La estrategia de control basado en pasividad por transferencia de interconexión y amortiguamiento es seleccionada, porque modifica la función de energía potencial y cinética sin depender de las funciones de Casimir ni de superar obstáculos de disipación, preservando al mismo tiempo los atributos port-Hamiltonianos. Por consiguiente, esta estrategia es conveniente para asegurar la estabilidad global en los sistemas de celdas fotovoltaicas.

Contents

List of Figures

List of Tables

Notations

Without loss of generality, for a given smooth function $f : \mathbb{R}^n \to \mathbb{R}$, we denote $\nabla_x f(x)$ as the differential expression $\dfrac{\partial f(x)}{\partial x}$.

Similarly, we denote $\nabla_x^n f(x)$ as the n^{th} term of the differential expression $\dfrac{\partial^n f(x)}{\partial x^n}$.

The time derivative of the function $f(t)$, i.e., $\dfrac{\mathrm{d}f(t)}{\mathrm{d}t}$, is expressed as $\dot{f}$.

All vectors are considered column vectors.

For a given vector $x \in \mathbb{R}^n$ and a matrix $A \in \mathbb{R}^{nxn}$, A is positive definite (or semi-definite), denoted as $A \succ 0$ (or $A \succcurlyeq 0$), if $A = A^\top$ and $x^\top A x > 0$ (or $x^\top A x \geqslant 0$) for all $x \in \mathbb{R}^n - \{0_n\}$ (or $x \in \mathbb{R}^n$).

For a given vector $x \in \mathbb{R}^n$ and a matrix $B \in \mathbb{R}^{nxn}$, the matrix B is skew-symmetric (or anti-symmetric), if $B = -B^\top$ and $x^\top B x = 0$ for all $x \in \mathbb{R}^n - \{0_n\}$.

For a given vector $x \in \mathbb{R}^n$, x^* denotes the equilibrium states of a system $f(x)$ if the system dynamics $\dot{x} = 0 \ \forall \ x = x^*$.

We denote R^+ as the set of strictly real numbers $\geqslant 0$.

Given an electrical circuit, the *Kirchhoff's Current Law* states: the sum of the n currents i_i flowing into a node equals the sum of the m currents i_j flowing out of the same node, i.e.,

$$\sum_{i=1}^{n} i_i = \sum_{j=1}^{m} i_j.$$

Given an electrical circuit, the *Kirchhoff's Voltage Law* states: the sum of the l voltages v_k around a close loop is zero, i.e.,

$$\sum_{k=1}^{l} v_k = 0.$$

Caveat: When possible, we omit the arguments to simplify the notation.

Acronyms

CFAI Curve Fitting with Artificial Intelligence. 26, 27

DCL-OSP DC-Link Output Side Parameters. 26, 27

EL Euler-Lagrange. 32

FI Flyback Inverter. 26, 27

IDA-PBC Interconnection and Damping Assignment Passivity-Based Control. 13, 23, 24, 32, 49, 55, 58–69, 74, 77, 84, 86

IFI Interleaved Flyback Inverter. 26, 27

KCL Kirchhoff's Current Law. 36, 38, 50, 53, 69, 71, 72

KVL Kirchhoff's Voltage Law. 38, 40, 50, 53, 69, 71, 72

MIC Module Integrated Converter. 26, 27

MPP Maximum Power Point. 12, 21, 22, 25, 26, 49, 52, 57–60, 63, 64, 66, 67, 76

MPPT Maximum Power Point Tracking. 13, 15, 21–27, 48, 49, 55, 58, 59, 61, 66–87, 95

PBC Passivity-Based Control. 32

PDE Partial Differential Equation. 32, 57, 58, 77, 78, 87, 95

PH port-Hamiltonian. 23–25, 31–33, 36, 38–40, 42, 44, 48, 49, 51–54, 58, 59, 68, 70, 72–74, 78, 84, 86, 87

PHS Pumped-Hydro Storage. 15, 35, 36, 38, 44, 46, 48, 87

PS Partial Shading. 25

PV Photovoltaic. 12, 13, 20–28, 35–38, 45–54, 58–61, 63–70, 74, 76, 79–84, 86, 87, 95

QDBBC Quasi-Double Boost Based Converter. 26, 27

SDGs Sustainable Development Goals. 19

SMC Sliding Mode Control. 13, 49, 58–62, 64, 66, 67, 95

TRM Temperature or Radiation Monitoring. 26, 27

VOB-MPPT Voltage Open Based MPPT. 26, 27

VR Voltage Regulation. 13, 15, 22–24, 48, 68, 69, 73, 74, 77, 79, 80, 82–84, 86, 87

Chapter 1

Introduction

During the last century, governments had mainly focused on developing isolated progress plans to fight poverty and inequality. But today's reality shows that inequalities within countries are on the rise, and people and communities across the globe are feeling the climate change effects and environmental degradation. For this reason, in 2015, the United Nations General Assembly proposed the Agenda 2030, which defines a route to fight extreme poverty, inequality, and injustice, and protect the planet's environment, centering the success in energy sustainability [2], supported by 17 Sustainable Development Goals (SDGs) and 169 targets.

Researchers have demonstrated that renewable energy technologies can supply two-thirds of the total global energy demand, enable an inclusive and equitable social-economic development, and attenuate global warming to 1.5°C [2, 3]. Added, empirical analysis has confirmed a positive impact on the economic growth of 58% for several countries with the green energy transition due to the strong relationship between renewable energy consumption and economic growth [4]; i.e., the impact of renewable energy generation on sustainable development is more significant than the impact of non-renewable energy [5, 6].

There is a global consensus on replacing fossil fuels as the primary sources for generating electrical energy, transportation, and consumption for the following decades. The increasing penetration of renewable energy sources aims to become the best option to support the fleet of hybrid and electric vehicles, together with households and industry consumption, which will require a much more dynamic electrical infrastructure [7, 8, 6].

The amount of energy that can be provided by a system powered with intermittent sources, such as solar or wind, faces up technical and economic limits that respond to two main factors: *a)* coincidence of production with the energy demand, and *b)* the ability to reduce the production of conventional generators or storage the excess of produced energy [8]. Solutions to efficiently implement renewable energy technologies are globally critical, as these technologies are expected to take the lead role in the following power generation portfolio and achieve sustainable power generation. With increased energy storage techniques, prices, and efficiencies become more favorable, reflected in cheaper energy storage and production systems [6].

1.1 Electrical Energy in Costa Rica

In 2022, 98.7% of Costa Rica's electric power demand was supported by renewable sources, and 1.3% was produced from non-renewable sources (thermal energy from internal and external suppliers) [1], as shown in Fig. 1.1.

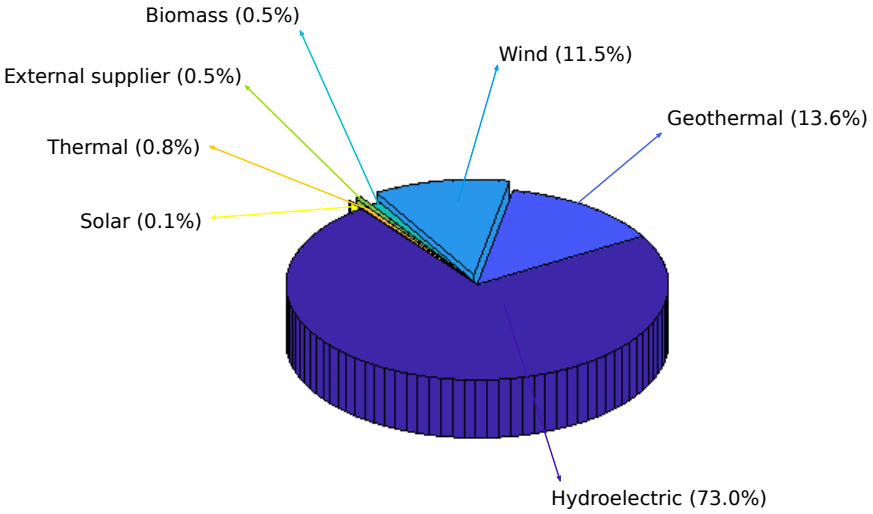

Figure 1.1: Ratio of the energy sources that covered the electric power demand in 2022, Costa Rica [1].

Thermal energy implies using fossil fuels to support the energy deficit during peak hours, mainly in the dry season. The efforts to reduce fossil fuel use are threatened since the historical projection of electrical demand foresees a rise of 26% in 2040 compared to 2022 [9].

Conversely, Fig. 1.2 compares a typical Friday's electrical energy demand trend in the rainy and dry seasons. From 5 to 23 hours, the energy increases almost twice that of the rest of the day, with clear peaks at 12 and 18 hours, coincidentally with lunch and dinner time. Furthermore, the wet season demand (March) is higher than the dry season (September) due to air conditioners, chillers, and fans compromising the installed hydroelectric capacity.

Since the highest level of solar irradiance in Costa Rica reaches a daily average of 5kWh/m^2 [10] from 10 to 15 hours, matching the highest demand peak on Fig. 1.1, it remains a feasible alternative to cover the leak of future energy requirements on grid-connected or stand-alone home and industrial solar energy harvest systems. However, the intermittent characteristic of Photovoltaic (PV) power generation and the low-efficiency performance of the PV cells due to the dependence on climatic conditions, such as irradiance and temperature [11], have become a drawback to increasing its penetration in the country.

1.2 Reliability Improvements on Solar Energy

Science and industry have dabbled with more technologically efficient solutions to harness the available resources [12, 13], looking forward to improving the throughput of the renewable

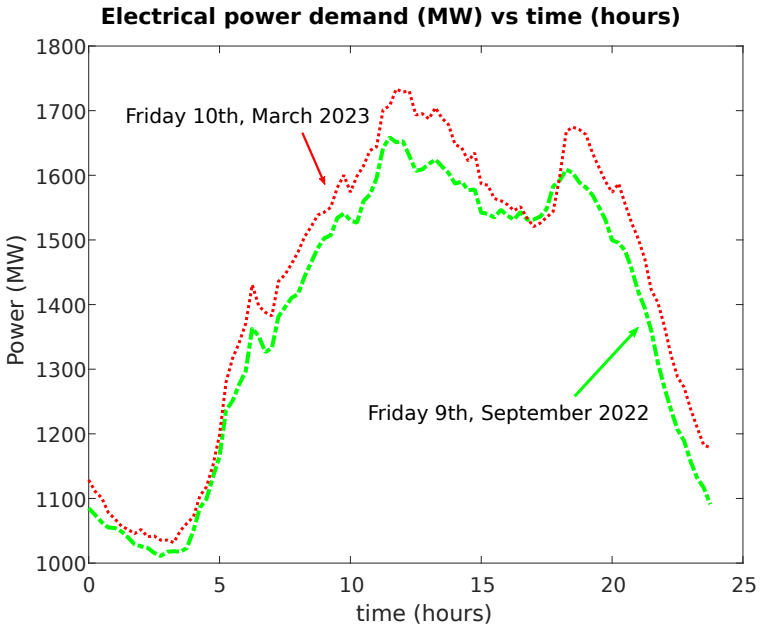

Figure 1.2: Daily demand comparison trend of energy in rainy vs dry season, captured from the Real Time Operation of the National Electricity Control Center of the ICE Group, Costa Rica.

energy devices and the system's performance to harvested energy and enhancing it according to the final consumption load [14].

Solar energy technology is the most suitable substitute for fossil fuels and most household products [15]. PV cells convert solar energy into electricity, but a significant amount of the radiation passes through the cell or is reflected by the surface. Furthermore, the physical characteristics of the PV cell structure prompt several losses in energy generation, e.g., the optical absorption edge, the charges recombination into the material layers, the radiative events, the temperature disturbances, and the optical band gap of the specific technology [16, 17, 18, 19].

1.2.1 Maximum Power Point Tracking Approach

Efficiency improvements to extract the Maximum Power Point (MPP) of the solar PV cell systems have become a key challenge in renewable energy research [20]. On this wise, numerous control strategies have been extensively proposed to solve the issue of the Maximum Power Point Tracking (MPPT) of PV cell arrays. Several control algorithms have been previously proposed to improve the performance of the PV arrays in terms of the MPP and have been classified under different criteria [21, 22, 23, 20, 24, 25, 26, 27, 28, 29] as tabulated in Appendix A., e.g.:

- Conventional methods
- Mathematical based methods
- Measurement and Comparison based methods

- Constant Parameter based methods
- Trial and Error based methods
- Numerical based methods
- Intelligent Prediction and Iterative in Nature based methods

Passivity-based Controllers (PBC) have not been referred to in reviews' classifications, even when their reliability has been documented in several articles, such as [30, 31, 32, 33, 34, 35, 36, 37, 38, 39, 40, 41]. Moreover, hybrid and combined algorithms have been proposed to overcome the intrinsic concerns of the specific methods to track the MPP. See Appendix B for further information.

1.2.2 MPPT and Voltage Regulation Unified Control

The MPPT of PV cells and the Voltage Regulation (VR) of the load issues have been addressed by advanced algorithms for either grid-tied or stand-alone PV systems, as detailed in Appendix C. The referred controllers have been essentially analyzed via simulation resources; in some cases, the test was extended to hardware emulators under laboratory-controlled conditions. Furthermore, the controller's power consumption and the comparison to commercial devices' performance have been neglected from the test scopes.

1.2.3 Current Sensorsless Control Approach

The sensors for electrical current monitoring usually present disadvantages due to the complexity and the loss of connections, replacement complexity, inconsistent sensibility and resolution at low current, the parasitic magnetic energy remanence in the cores, periodical calibration requirements, erratic frequency response, and other inconveniences thoroughly discussed in [42, 43, 44]. Moreover, current sensors are usually expensive, which increases the inherent cost of the PV power system and, eventually, reduces its reliability by increasing the number of components and losses [43, 25, 45]. Consequently, the elimination of the current sensor to track the MPP has been proposed as an alternative option to increase the cost benefits of PV systems in many different configurations, mainly related to the MPPT of a single stage of PV cells approach [43, 46, 42, 45, 47, 48, 49, 50, 51, 52, 53, 54, 55, 56, 34, 57, 58, 59, 60, 61, 62, 63, 64, 65, 66, 67, 68, 69, 70, 71, 72]. The validity of the controllers mentioned above has been confirmed and compared to other methods by extensive simulation and experimental results.

1.3 Problem Formulation

Costa Rica suffered an energy leak of around 1.3% of the total production in 2022. Thermal sources supply this energy leak every year, which becomes more significant during the dry season due to the activation of air conditioners, fans, and chillers in houses and industries. This situation would worsen over the following years with the incursion of electric mobility to comply with the SDGs of the Agenda 2030. Moreover, the internal politics of energy

expansion haven't stimulated the penetration of solar energy technologies in the country. Consequently, solar production reached only 0.1% of the total electrical generation in 2022.

On the other hand, several areas of the country receive a daily irradiation average of $5kWh/m^2$ during the dry season, in a period that matches the maximum demand of daily energy consumption. According to the Costa Rican solar systems suppliers, the cost of electricity has increased an average of 12% year to year in the last 25 years. In contrast, the return on the investment of a traditional family house stand-alone system ranges from 6 to 14 years [73, 74]. Hence, solar energy becomes an attractive solution for stand-alone or grid-connected users.

There has been a significant amount of proposals for MPPT and VR controllers, designed and validated primarily via simulation or emulated in laboratories, but, to the best of our knowledge, it is required a unified solution for MPPT and output-load VR issues with a low power consumption of the control stage to improve the development of the home systems PV cell generation and the storage of energy in batteries, based on a non-invasive monitoring strategy with a reduced amount of sensors. Thus, this thesis aims to fill this gap by fulfilling the following goal:

"provide a dependable DC-DC converter prototype to resolve the MPPT and Output Load VR problems, created on a nonlinear model framework and controlled by a cost-effective algorithm. It should be designed for a non-invasive monitoring system that requires less power consumption than a typical commercial device"

Our primary concern is implementing a current-sensorless prototype to be validated under natural irradiation conditions, able to reach the MPPT under input fluctuations. At the same time, the output voltage remains stable on a defined equilibrium state, i.e., a voltage battery charging level, operating with a lower energy consumption than a rated commercial device.

1.4 Contributions and Outline of this thesis

In this thesis, we propose, design, implement and evaluate novel nonlinear control laws to solve the MPPT and VR issues of a PV cell system connected to a load across a DC-DC conversion stage.

To establish the strategies lines of this document, in Chapter 2, we deepen in preliminary technical and theoretical information related to PV cell models, MPPT control methods, DC-DC converters generalities, the port-Hamiltonian (PH) modeling framework, and the Interconnection and Damping Assignment Passivity-Based Control (IDA-PBC) strategy, to define the survey limits of the subsequent chapters.

Once the scope is delimited, in Chapter 3 we propose the design and simulation of a nonlinear model of a Solar-Powered Pumped-Hydro Storage System made up of a PV cell stage, a DC-DC buck converter, an electrical pump, and a pipe to impulse recovery water into a reservoir. This complex multi-physical system lies between the electrical, mechanical, and hydraulic domains, becoming a suitable example to confirm the capabilities of the PH modeling framework in terms of its simplicity, which benefits literal interpretations from the physical to the mathematical structure. Moreover, the designed system model is validated

via simulation under several DC-DC converter switching state fluctuations.

Further, we focus on the MPPT issue of a PV cell stage connected to a DC-DC boost converter to feed a resistive load. To solve it, we propose an IDA-PBC strategy in Chapter 4. The system is designed in a current sensor-less topology under the PH framework. Its performance is evaluated firstly via simulation with a comparison to a Sliding Mode control strategy. Then, the system is implemented in a simple controlled physical prototype.

Likewise, in Chapter 5, a system of a PV cell stage feeding a battery with a DC-DC buck-boost own design converter is controlled to solve the MPPT and the VR issue by a double switching highly nonlinear control law. Once again, the system and the control follow the PH framework and the IDA-PBC strategy. The designed system and the control law are validated by comparing the performance of an own designed prototype against a commercial device in terms of power consumption efficiency.

Finally, we recapitulate the results and specific conclusions from the proposed systems along this thesis in Chapter 6, giving the general concluding remarks and some outlook conducted to suggest future lines of research starting from our results.

1.5 Published Contents

The following articles represent essential contributions to this thesis:

1.5.1 Main Articles

Hayden Phillips-Brenes, Roberto Pereira-Arroyo, and Mauricio Muñoz-Arias. Energy-based model of a solar-powered pumped-hydro storage system. In*2019 IEEE 39th Central America and Panama Convention (CONCAPAN XXXIX)*, pages 1–6, 2019.

Hayden Phillips-Brenes, Roberto Pereira-Arroyo, Renato Rímolo-Donadío, and Mauricio Muñoz-Arias. Current-Sensorless Control Strategy for the MPPT of a PV Cell: An Energy-Based Approach. *International Journal of Photoenergy*, 2022:1747533, 2022.

Hayden Phillips-Brenes, Mauricio Muñoz-Arias, Roberto Pereira-Arroyo, Renato Rímolo-Donadío, and Luis Miguel Esquivel-Sancho. Interconnection and Damping Assignment Energy Control for Photovoltaic dc-dc Conversion and Output Voltage Regulation. *IEEE Transactions on control System Technology*, Submitted

1.5.2 Other Articles

Luis Miguel Esquivel-Sancho, Mauricio Muñoz-Arias, Hayden Phillips-Brenes, and Roberto Pereira-Arroyo. A Reversible Hydropump–Turbine System. *Applied Sciences*, 2022, 12(18):9086.

Chapter 2

Preliminaries

In this Chapter, we provide the theoretical background employed during the development of this thesis. Firstly, section 2.1 presents a general overview of the MPPT methods scope, followed by a more specific current-sensorless classification in section 2.2, suitable to determine the selection of the MPPT method in Chapters 3, 4 and 5. The conceptual model and the equivalent physical equations of the DC-DC converters and the PV cell to develop the proposed systems in Chapters 3, 4 and 5 are deeply explained in sections 2.3 and 2.4. The so-called PH mathematical framework is also introduced in section 2.5 as a tool to establish the state equations that describe the systems covered in this thesis. Finally, the statements and requirements to design the control strategy implemented to govern the systems in Chapters 4 and 5 are fully detailed and linked to the PH mathematical framework in sections 2.6.

2.1 Overview of MPPT Methods

The objective and scope of the MPPT control techniques exposed in section 1.2.1 can address a different approach based on the application requirements and system constraints [26]. A first approach is centered on extracting the *MPP of a single stage of PV cells* (or a single PV Cell) under any environmental condition in a relatively small area. The stage works specifically over a single block exposed to local disturbances, independently from the rest of the PV cell array, e.g., passivity-based controllers, conventional, mathematics based, measurement and comparison based, constant parameters based, trial and error based, and numerical based methods. Since the objective of this approach relies on tracking a local MPP of a specific area of PV cells, its robustness depends on the control effectiveness under input and output over the controlled stage, i.e., radiation or output load. Consequently, the shading issue over different PV cell blocks of the array is neglected from this scope. Although the effectiveness of several Intelligent Prediction and Iterative Nature methods has been verified by simulation and experiments to solve the single-stage approach, such algorithms imply high complexity and slow convergence speed [75]. Moreover, the local MPPT approach is suitable in applications of small areas, such as solar vehicles, space satellites, and solar water pump systems [24].

On the other hand, a second approach conducts on the *Global MPP of extensive PV cells array*, where Partial Shading (PS) over a section of the array area has an appreciable

effect due to the dimensions of the whole array. The acrshortps on a single block distorts the Global MPP of the PV cell array due to the impact of the power-voltage characteristics of any single shaded block over the features of the whole PV cell stage, leading to multiple spikes that confused the MPPT control unit, while it remains in a local MPP instead of a global one [76, 77, 78, 79, 80, 81, 82, 83, 84, 85, 86]. This approach is based on the flexibility to modify the architecture of the PV cell array to balance the power distribution between fully illuminated, partially shaded, and shaded blocks over the area of the whole array [78]. Intelligent Prediction and Iterative in Nature methods have the advantage of working with imprecise inputs, becoming more suitable for applications where acrshortps over extensive areas represents a critical issue [26].

The classification of the MPPT methods according to the scope is summarized in Table 2.1

Table 2.1: MPPT Scope Classification

Local MPP of a single PV cell stage	**Global MPP of extensive PV cell array**
Passivity-based controllers, Mathematics based, Conventional, Measurement and comparison based, Constant parameters based, Trial and error based, Numerical based	Intelligent prediction and iterative in nature

2.2 Current Sensorless Control Classification

The several indirect current-sensorless-based MPPT technologies cited in section 1.2.3 can be classified according to the control technique and the converter topology [20, 24, 25, 26], i.e., Module Integrated Converter (MIC), Voltage Open Based MPPT (VOB-MPPT), DC-Link Output Side Parameters (DCL-OSP), Curve Fitting with Artificial Intelligence (CFAI), Temperature or Radiation Monitoring (TRM), Quasi-Double Boost Based Converter (QDBBC), Flyback Inverter (FI), and Interleaved Flyback Inverter (IFI). To outline the relevance of the current-sensorless based MPPT techniques, in Table 2.2 it has evaluated their dependence on the topology and the monitoring requirements [21, 22, 23, 20, 24, 25, 26, 27, 28].

Although either VOB-MPPT or TRM has demonstrated a low dependence on the topology type, VOB-MPPT implies a more complex process to determine the voltage on the MPP, while it requires constantly measuring the open voltage of the PV cell array. Controllers that sense radiation instead of electric current are considered an effective solution for MPPT control due to their economic advantage and faster and minimally invasive characteristics. Additionally, a single radiation sensor is helpful to drive several controllers governing PV cell arrays that are exposed to the same radiation circumstances.

Table 2.2: MPPT Control Techniques Comparison

MPPT Technique	**Requiered Sensors**[a]	***Topology Dependence***
MIC	nV[b]	High
VOB-MPPT	V	Low
DCL-OSP	2V	High
CFAI	2V	Medium
TRM	V, T, R	Low
QDBBC	2V	High
FI	2V	High
IFI	3V	High

[a]V: voltage; T: temperature; R: radiation.
[b]n: amount of single modules in a serial connection.

2.3 Photovoltaic Cell Description

A PV cell is a superposition of layers of two dissimilar materials that transform light radiation into electric energy. Usually, one is an elemental metal that works as electrode contact (positive and negative), and the other is a solid compound of two semiconductors: a p-type and an n-type doped [87]. This configuration behaves like a diode D_1 connected to an equivalent array of parallel and serial output resistors R_p and R_s. The equivalent circuit of the PV cell stage is depicted in Fig. 2.1.

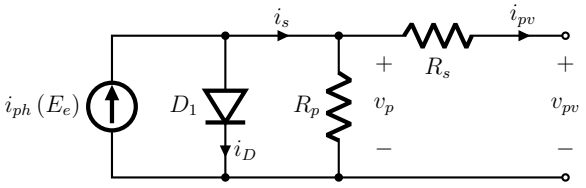

Figure 2.1: Electric diagram of a two layers PV cell.

The electrical behaviour of the PV cell current source $i_{ph}(E_e)$ and the current i_D across the diode are accurately described in the *five-parameter model* approach [88, 89, 90, 91, 92, 93, 94] as

$$i_{ph}(E_e) = N_p\left(I_{SC,nom} + K_0\Delta T\right)\frac{E_e}{E_{nom}}, \tag{2.1}$$

where N_p corresponds to the amount of similar PV cells in a parallel connection into the same stage ($N_p = 1$ for a single PV cell stage), E_{nom} is the nominal irradiance given by the manufacturer in the PV cell information, E_e the instantaneous solar irradiance, $\Delta T = T - T_v$ with T_{nom} the manufacturer reference temperature and T_v the instantaneous PV cell temperature, $I_{SC,nom}$ the output short-circuit current measured at $\{E_{nom}, T_{nom}\}$, K_0 the PV

cell thermal correction factor for $I_{SC,nom}$, and

$$i_D\left(v_{pv}, i_{pv}\right) = N_p i_0 \left(\exp\left(\frac{v_{pv} + i_{pv}\frac{N_s}{N_p}R_s}{N_s\alpha} \right) - 1 \right)$$
$$= N_p i_0 \left(\exp\left(\frac{v_p}{N_s\alpha} \right) - 1 \right), \tag{2.2}$$

with i_0 the p-n diode saturation current, N_s the amount of similar series-connected PV cells, $\alpha = nV_t$ where n the pn junction ideal factor and V_t the thermal voltage of the p-n diode. i_0 of (2.2) is defined as

$$i_0 = i_\alpha \left(\frac{T_{nom}}{T_v} \right)^{\frac{3}{n}} \exp\left(\frac{-V_g}{nk} \left(\frac{1}{T_{nom}} - \frac{1}{T_{pv}} \right) \right), \tag{2.3}$$

i_α a constant value, V_g the band-gap of silicon and k the Boltzmann constant. The i_α constant is given by

$$i_\alpha = \frac{I_{SC,nom}}{\exp\left(\frac{V_{OC,nom}}{nV_t} \right) - 1}, \tag{2.4}$$

where $V_{OC,nom}$ represents the output-open voltage of the PV cell measured at $\{E_{nom}, T_{nom}\}$.

2.4 DC-DC Converters Features

Power DC-DC converters are the most accepted solution to improve the systems' efficiency of green sources where isolation is unrestricted, such as DC motor drives, computers, cars, ships, aircraft, PV systems, and others [95, 96]. Transformer-less converters with single-switched configurations are the preferred selection for design due to their cost, size, lightweight, efficiency, energy flow, and reliability features at any input variations [97, 98]. Moreover, the DC-DC converters' performance depends on voltage or current stress on semiconductors (transistors and diodes), voltage gain, overall efficiency, input current ripple, and output voltage ripple [95, 98]. Therefore, they demand a high-performance control algorithm design to overcome the nonlinear and time-varying behavior of the switched structure. A sturdy design leads the controller to accomplish system stability with satisfactory dynamic response in the presence of external disturbances, parametric uncertainties, and load variations [99, 96].

2.4.1 Topologies

Many DC–DC converter topologies have been proposed and implemented to solve several applications, such as buck, boost, buck–boost, sepic, cuk, and zeta configurations. Improvements to those conventional topologies to reach more stable designs have been reported in several surveys; however, only the gain, the ripple, or the power can be substantially improved, while the efficiency and the switching frequency remain near the same ranges, e.g., [100, 101].

A comparison of several documented features of the main DC-DC converters configurations has been summarized in Table 2.3 [102, 103, 98, 100, 101, 104].

Table 2.3: DC-DC Converters Topology Comparison

Topology	**Voltage Gain** G_v	**Advantages**	***Disadvantages***
buck	$0 < G_v < 1$	Medium complexity High conversion efficiency	High ripple Medium cost Medium tracking efficiency
boost	$G_v > 1$	Low cost Medium complexity High conversion efficiency	High ripple Low tracking efficiency
buck-boost	$-\infty < G_v < 0$	Low ripple Low cost Medium complexity High tracking efficiency	Medium conversion efficiency
sepic	$0 < G_v < +\infty$	Low ripple High tracking efficiency	High complexity Medium cost Medium conversion efficiency
cuk	$-\infty < G_v < 0$	Low ripple High tracking efficiency	High complexity Medium cost Medium conversion efficiency
zeta	$0 < G_v < +\infty$	Low ripple High tracking efficiency	High complexity Medium cost Medium conversion efficiency

According to Table 2.3, the buck-boost converter topology has demonstrated the most advantageous design regarding advantage-disadvantage comparisons.

2.4.2 Electric Diagrams

The electric diagrams of the primary DC-DC converters are shown in Fig. 2.2, where $\{v_{in}, i_{in}\}$ are the input voltage and current of the stage, and $\{v_{out}, i_{out}\}$ the output voltage and current [99].

From Fig. 2.2, it can be determined that the buck, boost, and buck-boost DC-DC converters demand fewer components than the remaining topologies.

2.4.3 General Equations

The equations of gain and input resistance R_{in} of the DC-DC converters are shown in Table 2.4. The duty cycle D is define like the ratio between the close state period T_{rise} and the open state period T_{fall} of the DC-DC converter switch S, i.e.,

$$D = \frac{T_{rise}}{T_{rise} - T_{fall}}. \tag{2.5}$$

The voltage gain of the DC-DC boost converter holds a low efficiency when the magnitude of the duty cycle $D \to 1$ [95, 105, 106]. Hence, control strategies designed to consistently

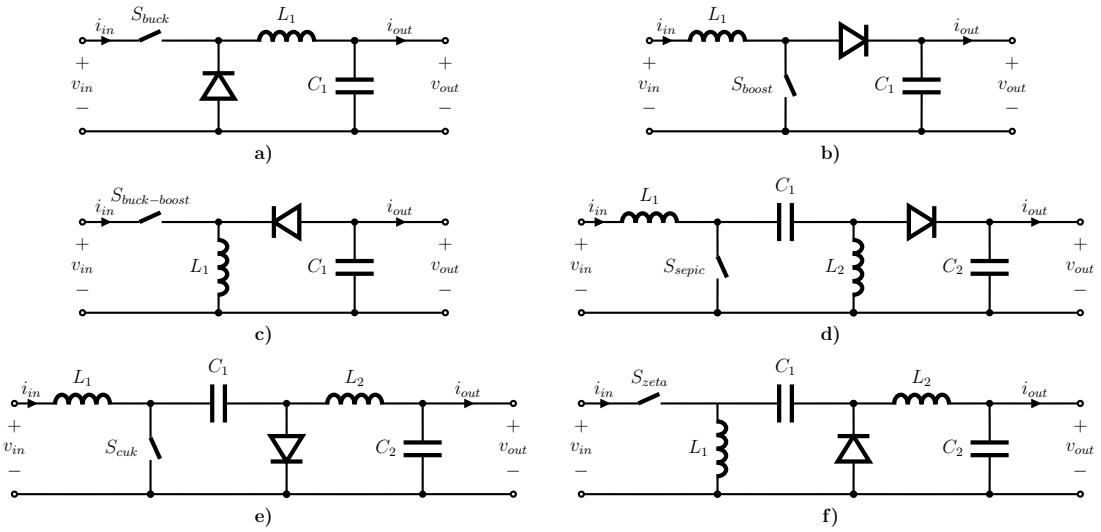

Figure 2.2: Electric diagram of DC-DC converters: **a)** buck, **b)** boost, **c)** buck-boost, **d)** sepic, **e)** cuk, **f)** zeta.

Table 2.4: DC-DC Converters Main Equations

Topology	**Voltage Gain**[a]	**Input Resistance**
buck	$\frac{v_{out}}{v_{in}} = D$	$R_{in} = \frac{R_{load}}{D^2}$
boost	$\frac{v_{out}}{v_{in}} = \frac{1}{1-D}$	$R_{in} = R_{load}\left(1-D\right)^2$
buck-boost	$\frac{v_{out}}{v_{in}} = -\frac{D}{1-D}$	$R_{in} = R_{load}\frac{\left(1-D\right)^2}{D^2}$
sepic	$\frac{v_{out}}{v_{in}} = \frac{D}{1-D}$	-
cuk	–	-
zeta	–	-

[a] D: Duty Cycle

provide constant output voltage across the load, despite input voltage and load fluctuation, is the major challenge of researchers of DC-DC boost converters [106, 107, 99, 108, 109].

2.5 Port-Hamiltonian Framework

This section introduces the PH framework for a general class of (non)linear physical systems which is based on the description of their energy (Hamiltonian) function, interconnection structure, dissipating elements, and power port-pairs (inputs and outputs) [110, 111, 112]. The dynamics of (non)linear mechanical, electrical, hydraulic, thermal, and electromechanical systems can be modeled and controlled via the PH formalism. A characteristic of the PH framework is how it clearly shows the energy transfer between the physical system and the environment is modeled via the energy storage and dissipation elements and their power-preserving ports, [110, 111].

A time-invariant PH system is given by

$$\Sigma_{PH} \begin{cases} \dot{x} = \left[\mathcal{J}\left(x\right) - \mathcal{R}\left(x\right)\right] \nabla_x H\left(x\right) + g\left(x\right) u, \\ y = g\left(x\right)^\top \nabla_x H\left(x\right), \end{cases} \tag{2.6}$$

where the state variable is given by $x \in \mathbb{R}^{\mathcal{N}}$, and the input-output port-pair $\{u, y\}$ representing flows and efforts are given by

$$u \in \mathbb{R}^{\mathcal{N}}, \tag{2.7}$$

$$y \in \mathbb{R}^{\mathcal{M}}. \tag{2.8}$$

Furthermore, the input, interconnection, and dissipation matrices of (2.6) are given by

$$g\left(x\right) \in \mathbb{R}^{\mathcal{N}\times\mathcal{M}}, \tag{2.9}$$

$$\mathcal{J}\left(x\right) = -\mathcal{J}\left(x\right)^\top,\ \mathcal{J}\left(x\right) \in \mathbb{R}^{\mathcal{N}\times\mathcal{N}}, \tag{2.10}$$

$$\mathcal{R}\left(x\right) = \mathcal{R}\left(x\right)^\top \succcurlyeq 0,\ \mathcal{R}\left(x\right) \in \mathbb{R}^{\mathcal{N}\times\mathcal{N}}, \tag{2.11}$$

where $\mathcal{M} \leq \mathcal{N}$ being $\mathcal{M} = \mathcal{N}$ a fully actuated system, and $\mathcal{M} < \mathcal{N}$ an under-actuated one. It follows that the energy function of the system (2.6) is

$$H\left(x\right) \in \mathbb{R}. \tag{2.12}$$

If the Hamiltonian function is solved along the trajectories of $\dot{x}$ as in (2.6), i.e., (2.12) is differentiated concerning time, it follows that

$$\begin{aligned} \dot{H}\left(x\right) &= \nabla_x^\top H\left(x\right) \dot{x} = \nabla_x^\top H\left(x\right) \left[\mathcal{J}\left(x\right) - \mathcal{R}\left(x\right)\right] \nabla_x H\left(x\right) + \nabla_x^\top H\left(x\right) g\left(x\right) u \\ &= \nabla_x^\top H\left(x\right) \mathcal{J}\left(x\right) \nabla_x H\left(x\right) - \nabla_x^\top H\left(x\right) \mathcal{R}\left(x\right) \nabla_x H\left(x\right) + \nabla_x^\top H\left(x\right) g\left(x\right) u, \end{aligned} \tag{2.13}$$

since $\mathcal{J}\left(x\right)$ is skew-symmetric as in (2.10) and $\mathcal{R}\left(x\right)$ is a positive semi-definite matrix as in (2.11), then $\nabla_x^\top H\left(x\right) \mathcal{J}\left(x\right) \nabla_x H\left(x\right) = 0$ and $\nabla_x^\top H\left(x\right) \mathcal{R}\left(x\right) \nabla_x H\left(x\right) \geq 0$. Furthermore,

the output complies $y = g(x)^\top \nabla_x H(x)$ as in (2.6) and we recover the power balance $\dot{H}(x)$ in (2.13) as

$$\dot{H}(x) = -\nabla_x^\top H(x) \mathcal{R}(x) \nabla_x H(x) + y^\top u \leq y^\top u, \tag{2.14}$$

where we see how (2.6) complies with the description of a conservative system.

2.6 Interconnection and Damping Assignment Passivity-Based Control

The Passivity-Based Control (PBC) strategy was introduced in [113] to define a controller design methodology that achieves stabilization by passivation of the system regarding a storage function that has a minimum at the desired equilibrium point. The idea has succeeded in simple mechanical systems described in the classical Euler-Lagrange (EL) model that can be stabilized, shaping only the potential energy. However, applications that involve modifying kinetic energy cannot utilize the closed loop system as it is no longer considered an EL system. Even though it operates passively, the quadratic storage function for the passive map lacks an interpretation for total energy as these designs perform an inversion of the system along the reference trajectories [114, 115].

Hence, the IDA-PBC strategy introduced in [115] offers a methodology able to shape the overall energy of a (non)linear system, particularly advantageous for underactuated systems. It extends to a broader class of systems in applications that usually require kinetic and potential energy shaping to achieve the desired stable equilibrium points [116]. IDA-PBC can shape the energy function without the need for Casimir functions or overcoming the Dissipation Obstacle [117].

The IDA-PBC adjusts the potential energy shape using a closed-loop function that considers the disparity between the system's energy and the energy supplied by the controller. The energy shape is modified by transforming (assigning) the interaction between different subsystems (Interconnection) or the rate at which energy dissipates or decays in a system (damping). This modification should preserve the system's structure and inherent passivity properties. Hence, the equilibrium point of the system is reached through energy stabilization, [117, 115, 118]. This strategy is compatible with the concept of PH, as it preserves the physical (Hamiltonian) structure within a closed loop. Additionally, the passive map's storage function is accurately represented by the total energy of the closed-loop system.

The IDA-PBC process design ensures that the internal energy exchanges of the PH systems occur in the interconnection and damping matrices. Consequently, the system is transformed into a new structure with new desired matrices, described by critical parameters to be solved from a Partial Differential Equation (PDE). The solution of this PDE contains a set of energy functions that can be assigned to characterize the new system [112, 115]. Moreover, a solution that satisfies the minimum requirements is chosen to solve the control function u, and (2.6) became in new static state feedback closed-loop system

$$\dot{x} = \left[\mathcal{J}_d(x) - \mathcal{R}_d(x)\right] \nabla_x H_d(x), \tag{2.15}$$

with $\mathcal{J}_d(x) = -\mathcal{J}_d(x)^\top$, $\mathcal{R}_d(x) = \mathcal{R}_d(x)^\top \succcurlyeq 0$ the desired interconnection and damping matrices, and $H_d(x)$ a resultant energy function, containing a strict local minimum at the

desired equilibrium state x_0, Hence, the desired system's dissipative performance is preserved in the desired system (2.15). To ensure that the designed control strategy stabilizes the overall system and achieves the desired stability and performance goals, the structure of the desired new system is designed and analyzed under Lyapunov Theory (see Appendix D about Nonlinear Stability and Appendix E about Lyapunov Function for more details).

The mathematical statements that satisfy the coherence of the passive system are described in the following proposition.

Proposition 1. [115]

Given a general time-dependant system of the form (2.6)*, such that* $\mathcal{J}_d(x,u)$*,* $\mathcal{R}_d(x,u)$*,* $H(x)$*,* $g(x,u)$ *and the desired equilibrium state* $x_0 \in \mathbb{R}^{\mathcal{N}}$*, to be stabilized. Let assume the functions* $\beta(x) = u$*,* $\mathcal{J}_a(x)$*,* $\mathcal{R}_a(x)$*, and a vector function* $\mathcal{K}(x)$ *that satisfy*

$$\begin{aligned}&\{[\mathcal{J}(x,\beta(x)) + \mathcal{J}_a(x)] - [\mathcal{R}(x) + \mathcal{R}_a(x)]\}\,\mathcal{K}(x) = \\ &-[\mathcal{J}_a(x) - \mathcal{R}_a(x)]\,\nabla_x H(x) + g(x,\beta(x))\end{aligned} \tag{2.16}$$

defining the new desired matrices $\mathcal{J}_d(x)$*, and* $\mathcal{R}_d(x)$ *as*

$$\begin{aligned}\mathcal{J}_d(x) &:= \mathcal{J}(x,\beta(x)) + \mathcal{J}_a(x),\\ \mathcal{R}_d(x) &:= \mathcal{R}(x) + \mathcal{R}_a(x),\end{aligned} \tag{2.17}$$

it follows that the vector function $\mathcal{K}(x)$ *should be found to obtain a controller function* $\beta(x)$*, which meets several requirements defined later on to keep mathematical consistence.* ■

To preserve the PH structure of the closed-loop system, it must first be satisfied with an *structure preservation* of the damping and interconnection matrix properties. Further, the vector function $\mathcal{K}(x)$ should meet *integrability statement*, that describes a transpose property of its differential expression, where the control function $\beta(x)$ can be solved. Subsequently, the control function stability is defined from an *equilibrium assignment* condition, follow by a *Lyapunov Stability* analysis. Henceforth, each statement is mathematically described as in [118]

(i) Structure preservation: Assume we can find functions $\beta(x)$, $\mathcal{J}_a(x)$, and $\mathcal{R}_a(x)$ that satisfy

$$\begin{aligned}\mathcal{J}_d(x) &= -[\mathcal{J}_d(x)]^\top\\ \mathcal{R}_d(x) &= [\mathcal{R}_d(x)]^\top \succcurlyeq 0,\end{aligned} \tag{2.18}$$

such that the PH properties of system (2.15) are preserved.

(ii) Integrability: Poincare's lemma states the following equivalence [119]:

$$[\exists\ H_a(x) : \mathbb{R}^n \to \mathbb{R} \text{ such that } \mathcal{K}(x) = \nabla_x H_a(x)]. \tag{2.19}$$

If the system matrix $[\mathcal{J}_d(x) - \mathcal{R}_d(x)]$ is invertible, then the system in (2.15) has a solution if and only if the integrability conditions complies [117]

$$\nabla_x \mathcal{K}(x) = \nabla_x \mathcal{K}(x)^\top. \tag{2.20}$$

(*iii*) Equilibrium assignment: If x_0 is a state value at a (locally) stable equilibrium, it can be verified that

$$\mathcal{K}(x_0) = -\nabla_x H(x_0) \tag{2.21}$$

(*iv*) *Lyapunov stability:* At x_0, the Jacobian of $\mathcal{K}(x)$ meets the condition of the inequality

$$\nabla_x \mathcal{K}(x_0) > -\nabla_x^2 H(x_0). \tag{2.22}$$

When the given conditions are met, the closed-loop system where $u = \beta(x)$ becomes a port-controlled Hamiltonian system with dissipation, as shown in equation (2.15). In terms of energy, it can be defined

$$H_d(x) := H(x) + H_a(x), \tag{2.23}$$

Furthermore, $x*$ is a (locally) stable equilibrium of the closed loop. If the largest invariant set under the closed-loop dynamics contained in

$$\{x \in \mathbb{R}^n | \nabla_x H_d(x)^\top \mathcal{R}_d(x) \nabla_x H_d(x)^\top = 0\}, \tag{2.24}$$

is equal then $x*$, it will be asymptotically stable.

Based on the power balance of (2.14), we can calculate

$$\dot{H}_d = \underbrace{u^\top y - \nabla_x H(x)^\top \mathcal{R}(x) \nabla_x H(x)}_{\dot{H}} + \dot{H}_a = -\nabla_x H_d(x)^\top \mathcal{R}_d(x) \nabla_x H_d(x), \tag{2.25}$$

given $\mathcal{R}_d(x) = \mathcal{R}_a(x) + \mathcal{R}(x)$, and assuming only the effect of the natural damping over the system (2.15), i.e., $\mathcal{R}_a(x) = 0$, we have that

$$\mathcal{R}(x) \nabla_x H_a(x) = 0, \tag{2.26}$$

we demonstrate a passivity-based controlled system.

We have introduced several preliminary theoretical based here, suitable for the mathematical development of the system's models and controllers designed in Chapters 3, 4 and 5, that we recapitulate as follows.

Chapter 3

Energy-Based Model of a Solar-Powered Pumped-Hydro Storage System

A Pumped-Hydro Storage (PHS) is an energy storage technology widely used for over a hundred years, reaching an efficiency round trip up to 80% [120]. For large-scale energy storage, it is the most cost-effective solution for utility grids. The concept of the system is shown in Fig. 3.1.

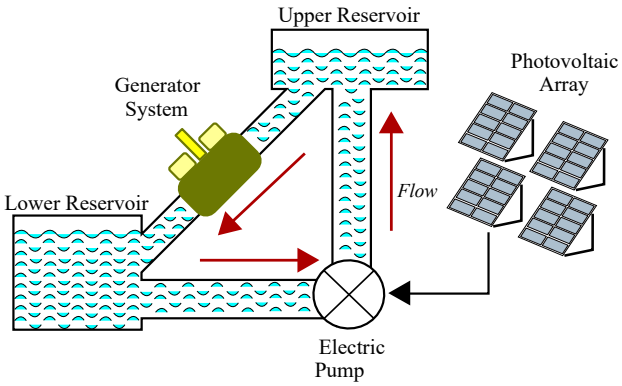

Figure 3.1: Conceptual diagram of the solar-powered pumped-hydro system for energy storage.

In this section, we proposed a port-Hamiltonian model of a pumped-hydro storage system, employing a PV cell as the primary source, as in [121]. The PV cell is connected to a DC motor pump across a DC-DC buck converter. Finally, water is pumped from a lower reservoir to an upper reservoir, as depicted in Fig. 3.1. We confirmed the model's functionality via simulation results under ideal conditions of constant solar radiation. The relationship between input solar irradiance and the energy stored at the upper reservoir is graphically demonstrated.

3.1 Mathematical Modeling of the PHS

Our model is based on the results of [122] and [123], rewriting the system on the PH framework due to the straightforward interpretation of the physical interconnection of multiple systems domains via power-ports and energy-storing and dissipating elements [111, 112, 110]. The PH design representation of the PHS clearly shows how the system's internal energy flows transversely over different physical domains. The PHS system has different stages that convert solar radiation into hydro-potential energy. A PV cell is an energy source transformed by a DC-DC buck converter to feed an electro-mechanical pumped-hydro stage. Subsequently, the pump system raises a water column via a water recovery pipe from a lower to an upper storage reservoir. A detailed block diagram of the different stages of the PHS system is shown in Fig. 3.2, where the inputs and outputs of each block are represented. Added, the stages are sorted in the respective physical domain, and we see how the system has the irradiance of the sun E_e as the input and the hydraulic flow Q_c as the output.

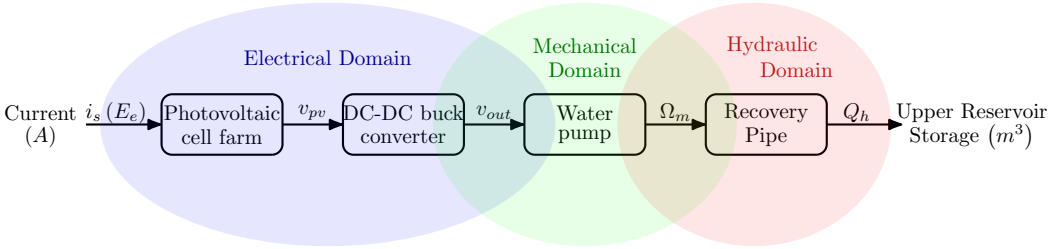

Figure 3.2: Energy storage system's block-diagram and related physical domains.

3.1.1 Photovoltaic Cell PH Modeling

The equivalent circuit of the PV cell is based on [90] and is shown in Fig. 3.3. This version includes a capacitor C_p connected in a parallel configuration to the resistor R_P, representing the parasitic load charging effects between the semiconductor layers. A serial resistor R_s is also included in the system's output power.

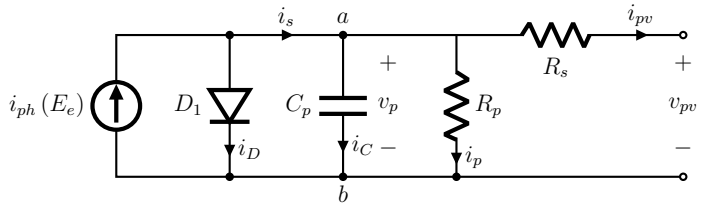

Figure 3.3: Electric diagram of the PV cell with an equivalent internal capacitor C_p.

The PV cell's output current i_{pv} depends on the switch function S_{buck} at the input of the DC-DC buck converter module of the subsequent stage that we introduce later on. By Kirchhoff's Current Law (KCL) in Fig. 3.3, it follows that

$$i_C = -i_p + i_s\,(E_e) - i_{pv}, \tag{3.1}$$

where $i_{pv} = S_{buck} i_{bc}$ according to the DC-DC buck converter stage explained in the next subsection, and

$$i_s\left(E_e\right) = i_{ph}\left(E_e\right) - i_D\left(v_{pv}, i_{pv}\right), \tag{3.2}$$

both currents i_{ph} and i_D explained in (2.1) and (2.2), and

$$i_p = \frac{v_p}{R_p}, \tag{3.3}$$

$$i_C = C_p \dot{v}_p. \tag{3.4}$$

We introduce the electrical charge q_p as a state variable in terms of the voltage v_p and the equivalents circuit's capacitance C_p such that

$$q_p = C_p v_p, \tag{3.5}$$

whose dynamics in (3.1) can be rewritten in terms of (3.5) to obtain

$$\dot{q}_p = -\frac{1}{R_p C_p} q_p + i_s\left(E_e\right) - S_{buck} i_{bc}. \tag{3.6}$$

We define now the dynamics of a second state variable of the system that represents the electrical flux, i.e., ϕ_{pv}, given by

$$\dot{\phi}_p = \frac{q_p}{C_p}, \tag{3.7}$$

and since the only energy-storing element of the system is the charge $_{pv}$ in the capacitor C_p, the Hamiltonian function $H_p\left(q_p, \phi_p\right)$ of the PV cell stage is given by

$$H_p\left(q_p, \phi_p\right) = \frac{1}{2C_p} q_p^2. \tag{3.8}$$

Hence, we solve from (3.8) the Hamiltonian function's partial-derivatives in terms of the state variables q_p and ϕ_p as

$$\nabla_{q_p} H_p\left(q_p, \phi_p\right) = \frac{q_p}{C_p}, \quad \nabla_{\phi_p} H_p\left(q_p, \phi_p\right) = 0, \tag{3.9}$$

and the dynamics in (3.6) and (3.7) in terms of the derivatives of (3.9) can be redefined as

$$\dot{q}_p = -\frac{1}{R_p} \nabla_{q_p} H_p + k \nabla_{\phi_p} H_p + i_s\left(E_e\right) - S_{buck} i_{bc} \tag{3.10}$$

$$\dot{\phi}_p = \nabla_{q_p} H_p, \tag{3.11}$$

where k represents a constant that is being conveniently chosen as equal to -1 to keep the skew-symmetric properties of the $\mathcal{J}\left(x_p\right)$ matrix to be defined in (3.12) later on.

Now, the PH formulation Σ_p of a PV cell stage in terms of the dynamics (3.10) and (3.11), together with the Hamiltonian function (3.8), is given by

$$\Sigma_p \begin{cases} \underbrace{\begin{bmatrix} \dot{q}_p \\ \dot{\phi}_p \end{bmatrix}}_{\dot{x}_p} = \underbrace{\begin{bmatrix} \frac{-1}{R_p} & -1 \\ 1 & 0 \end{bmatrix}}_{\mathcal{J}(x_p)-\mathcal{R}(x_p)} \underbrace{\begin{bmatrix} \nabla_{q_p} H_p\left(q_p, \phi_p\right) \\ \nabla_{\phi_p} H_p\left(q_p, \phi_p\right) \end{bmatrix}}_{\nabla_{x_p} H_p(x_p)} \\ \qquad\qquad + \underbrace{\begin{bmatrix} 1 \\ 0 \end{bmatrix}}_{g(x_p)} i_s\left(E_e\right) + \begin{bmatrix} -S_{buck} \\ 0 \end{bmatrix} i_{bc}, \\ y_p = g^{\top}\left(x_p\right) \nabla_{x_p} H_p\left(x_p\right) = v_p, \end{cases} \tag{3.12}$$

where the power balance in (2.14) for the system in (3.12) clearly holds since $R_p \geq 0$. The input-output port-pair of the system in (3.12) is established as $(u, y) = (i_s, v_p)$.

In the following subsections, we introduce the PH formulation for the DC-DC buck converter, the electro-mechanical stage, and the hydraulic system to connect the recovery pipe.

3.1.2 DC-DC Buck Converter PH Modeling

We defined the input voltage level of the hydro-pump DC motor as lower than the output voltage of the PV cell. Thus, the PHS system requires a DC-DC buck converter to reduce the PV cell's output voltage v_{pv} to a suitable voltage for the DC motor. Fig. 3.4 depicts the equivalent circuit of the DC-DC buck converter, based on the results of [124].

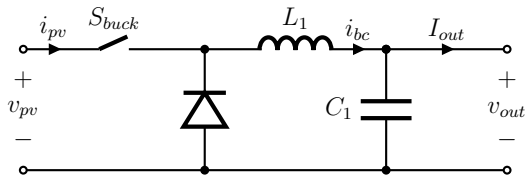

Figure 3.4: Electric diagram of the DC-DC buck converter governed by a normally open (NO) switch S_{buck}.

The discrete switch S_{buck} describes a function that activates and deactivates the input voltage of the equivalent circuit in Fig. 3.4, and the state variables (q_C, ϕ_L) being the charge of the capacitor C_1, and the flux in the inductor L_1 of the DC-DC buck converter. Based on the dynamics from KCL, we know that

$$C_1 \dot{v}_{out} = i_{bc} - i_{out}. \tag{3.13}$$

On the other hand, by Kirchhoff's Voltage Law (KVL) it follows that

$$L_1 \dot{i}_{bc} = -v_{out} + S_{buck} v_{pv}, \tag{3.14}$$

since v_{pv} in Fig. 3.3 can be solved

$$v_{pv} = v_p - R_s i_{pv}, \tag{3.15}$$

where $i_{pv} = S_{buck} i_{bc}$, then (3.14) can be rewritten

$$L_1 \dot{i}_{bc} = -v_{out} + S_{buck} v_p - S_{buck} R_p i_{bc}. \tag{3.16}$$

Furthermore, (v_{out}, i_{bc}) are defined in terms of the state variables (q_C, ϕ_L)

$$q_C = C_1 v_{out}, \quad \phi_L = L_1 i_{bc}, \tag{3.17}$$

given the Hamiltonian function $H_b(q_C, \phi_L)$ of the DC-DC buck converter

$$H_b(q_C, \phi_L) = \frac{1}{2C_1} q_C^2 + \frac{1}{2L_1} \phi_L^2. \tag{3.18}$$

The partial-derivatives of the Hamiltonian function (3.18) are solved in terms of the state variables q_C and ϕ_L as

$$\nabla_{q_C} H_b(q_C, \phi_L) = \frac{q_C}{C_1}, \quad \nabla_{\phi_L} H_b(q_C, \phi_L) = \frac{\phi_L}{L_1}, \tag{3.19}$$

thus, (3.13) and (3.16) become

$$\dot{q}_C = \nabla_{\phi_L} H_b(q_C, \phi_L) - i_{out}, \tag{3.20}$$

$$\dot{\phi}_L = -\nabla_{q_C} H_b(q_C, \phi_L) - S_{buck} R_p \nabla_{\phi_L} H_b(q_C, \phi_L) + S_{buck} v_p \tag{3.21}$$

and consequently, the PH system Σ_b of the DC-DC buck converter can be formulated from (3.20), (3.21) and (3.18) as

$$\Sigma_b \begin{cases} \underbrace{\begin{bmatrix} \dot{q}_C \\ \dot{\phi}_L \end{bmatrix}}_{\dot{x}_b} = \underbrace{\begin{bmatrix} 0 & 1 \\ -1 & -S_{buck} R_p \end{bmatrix}}_{\mathcal{J}(x_b) - \mathcal{R}(x_b)} \underbrace{\begin{bmatrix} \nabla_{q_C} H_b(q_C, \phi_L) \\ \nabla_{\phi_L} H_b(q_C, \phi_L) \end{bmatrix}}_{\nabla_{x_b} H_b(x_b)} \\ \qquad + \underbrace{\begin{bmatrix} 0 \\ S_{buck} \end{bmatrix}}_{g(x_b)} v_p + \begin{bmatrix} -1 \\ 0 \end{bmatrix} i_{out} \\ y_b = g^\top(x_b) \nabla_{x_b} H_b(x_b) = S_{buck} i_{bc}, \end{cases} \tag{3.22}$$

with $(v_p, S_{buck} i_{bc})$ the input-output port-pair (u_b, y_b) of the system Σ_b. Moreover, $\mathcal{J}(x_b)$ is a skew-symmetric matrix of the form

$$\mathcal{J}(x_b) = \begin{bmatrix} 0 & 1 \\ -1 & 0 \end{bmatrix}, \tag{3.23}$$

$\mathcal{R}(x_b) = 0$ when $S_{buck} = 0$, and $\mathcal{R}(x_b) \succ 0$ when $S_{buck} = 1$, then the power balance in (2.14) is fully complied.

3.1.3 Pumping Electrical-Mechanical PH Modeling

The pumping stage in charge of rising water from the lower to the upper reservoir requires a description in two physic domains. Therefore, Fig. 3.5 depicts the first domain in an electrical equivalent circuit.

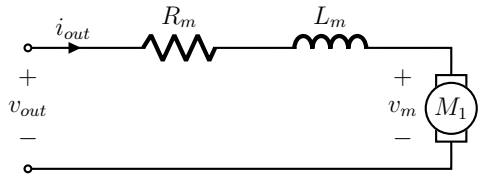

Figure 3.5: Equivalent electric diagram of the pump.

The inductance L_m represents the kinetic stored energy of the magnetic field of the motor engine M_1, and R_m the associated losses. From KVL, the dynamic of the electrical domain is described as

$$L_m \dot{i}_{out} = -R_m i_{out} + v_{out} - v_m. \tag{3.24}$$

We introduce here the magnetic flux ϕ_m as a state variable

$$\phi_m = L_m i_{out}, \tag{3.25}$$

and the dynamic of the charge stored in the circuit q_m

$$\dot{q}_m = \frac{\phi_m}{L_m}. \tag{3.26}$$

Since the components of the circuit 3.5 stored only magnetic field energy, then the Hamiltonian function $H_m(\phi_m, q_m)$ is given by

$$H_m(\phi_m, q_m) = \frac{1}{2L_m}\phi_m^2. \tag{3.27}$$

The Hamiltonian function's partial-derivatives are solved in terms of the state variables ϕ_m and q_m, i.e.,

$$\nabla_{\phi_m} H_m(\phi_m, q_m) = \frac{\phi_m}{L_m}, \quad \nabla_{q_m} H_m(\phi_m, q_m) = 0, \tag{3.28}$$

from (3.25) and (3.28) we redefine the dynamics in (3.24) and (3.26) as

$$\dot{\phi}_m = -R_m \nabla_{\phi_m} H_m + k \nabla_{q_m} H_m + v_{out} - v_m \tag{3.29}$$

$$\dot{q}_m = \nabla_{\phi_m} H_m. \tag{3.30}$$

being $k = -1$ an arbitrary constant that preserves the skew-symmetric properties of the $\mathcal{J}(x_m)$ in (3.31). Thus, the PH system Σ_{m1} of the pump equivalent electric circuit is defined

in terms of (3.24), (3.26), (3.27), (3.29) and (3.30), such that

$$\Sigma_{m1}\begin{cases}\underbrace{\begin{bmatrix}\dot{\phi}_m\\ \dot{q}_m\end{bmatrix}}_{\dot{x}_m} = \underbrace{\begin{bmatrix}-R_m & -1\\ 1 & 0\end{bmatrix}}_{\mathcal{J}(x_m)-\mathcal{R}(x_m)} \underbrace{\begin{bmatrix}\nabla_{\phi_m} H_m(\phi_m, q_m)\\ \nabla_{q_m} H_m(\phi_m, q_m)\end{bmatrix}}_{\nabla_{x_m} H_m(x_m)} \\ \qquad + \underbrace{\begin{bmatrix}1\\ 0\end{bmatrix}}_{g(x_m)} v_{out} + \begin{bmatrix}-1\\ 0\end{bmatrix} v_m \\ y_m = g^\top(x_m)\nabla_{x_m} H_m(x_m) = i_{out},\end{cases} \tag{3.31}$$

with an input-output port-pair $(u, y) = (v_{out}, i_{out})$.

Afterward, we model the mechanical stage of the pump. An equivalent free-body diagram of the pump is shown in Fig. 3.6, whose dynamics are described as

$$J_m\dot{\Omega}_m = -B_m\Omega_m + T_m - T_j, \tag{3.32}$$

where T_m and T_j represent the input and output torque, Ω_m the angular speed, J_m the inertia and B_m a friction losses constant.

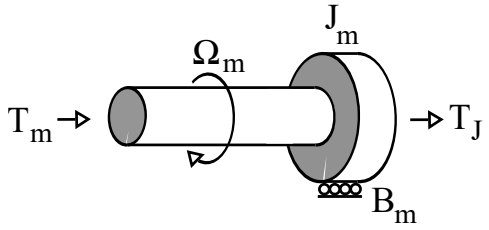

Figure 3.6: Equivalent mechanical diagram of the pump.

The relationship between the electrical and the mechanical domain of the pumping system is given by

$$T_m = K_m i_{out}, \qquad v_m = K_e\Omega_m \tag{3.33}$$

with K_m, K_e constant parameters of the pump. Similarly, a given constant K_h to match the mechanical to the hydraulic domain is described as

$$K_h = \frac{\Omega_m}{Q_h} = \frac{P_h}{T_J}, \tag{3.34}$$

where K_h has units of rad/m^3. Moreover, from the hydraulic system domain of Fig. 3.7, we know that

$$P_h = I_h\dot{Q}_h + R_hQ_h + P_{30} + \rho gl. \tag{3.35}$$

All the parameters in (3.35) are explained later on. Solving T_j from (3.34) and (3.35), we rewrite (3.32) as

$$\beta\dot{\Omega}_m = -\gamma_m\Omega_m + T_m - \frac{(P_{30} + \rho gl)}{K_h}, \tag{3.36}$$

with

$$\beta = J_m + \frac{I_h}{K_h^2}, \qquad \gamma_m = B_m + \frac{R_h}{K_h^2}, \tag{3.37}$$

where β represents an apparent mass inertia, and γ_m a system element of unified dissipation. Now, we define an angular momentum p_m based on the angular displacement Ω_m as

$$p_m = \beta \Omega_m. \tag{3.38}$$

Further, the dynamics expression in (3.36) is rewritten in terms of (3.38)

$$\dot{p}_m = -\gamma_m \frac{p_m}{\beta} + T_m - \frac{(P_{30})}{K_h} - \frac{(\rho g l)}{K_h}, \tag{3.39}$$

and a new system's dynamic $\dot{\varphi}_m$ is conveniently re-difined from (3.38) as

$$\dot{\varphi}_m = \frac{p_m}{\beta}. \tag{3.40}$$

The Hamiltonian expression $H_m(p_m, \varphi_m)$ of the mechanical system domain is given by

$$H_m(p_m, \varphi_m) = \frac{1}{2\beta} p_m^2 \tag{3.41}$$

and its function's partial-derivatives are solved in terms of the state variables p_m and φ_m

$$\nabla_{p_m} H_m(p_m, \varphi_m) = \frac{p_m}{\beta_m}, \quad \nabla_{\varphi_m} H_m(p_m, \varphi_m) = 0. \tag{3.42}$$

Thus, the dynamics in (3.39) and (3.40) are redefine from (3.42) as

$$\dot{p}_m = -\gamma_m \nabla_{p_m} H_m + k \nabla_{\varphi_m} H_m + T_m - \frac{(P_{30})}{K_h} - \frac{(\rho g l)}{K_h}, \tag{3.43}$$

$$\dot{\varphi}_m = \nabla_{p_m} H_m, \tag{3.44}$$

where $k = -1$ is an arbitrary constant required to preserve the skew-symmetric properties of the $\mathcal{J}(x_m)$ in (3.45). Based on (3.41), (3.42), (3.43) and (3.44), we formulate the dynamics of the mechanical pump stage in the PH system Σ_{m2} such that

$$\Sigma_{m2} \begin{cases} \underbrace{\begin{bmatrix} \dot{p}_m \\ \dot{\varphi}_m \end{bmatrix}}_{\dot{x}_m} = \underbrace{\begin{bmatrix} -\gamma_m & -1 \\ 1 & 0 \end{bmatrix}}_{\mathcal{J}(x_m) - \mathcal{R}(x_m)} \underbrace{\begin{bmatrix} \nabla_{p_m} H_m(p_m, \varphi_m) \\ \nabla_{\varphi_m} H_m(p_m, \varphi_m) \end{bmatrix}}_{\nabla_{x_m} H_m(x_m)} \\ \qquad\qquad + \underbrace{\begin{bmatrix} 1 \\ 0 \end{bmatrix}}_{g(x_m)} T_m + \begin{bmatrix} \dfrac{-1}{K_h} \\ 0 \end{bmatrix} (P_{30} + \rho g l) \\ y_m = g^\top(x_m) \nabla_{x_m} H_m(x_m) = \Omega_m, \end{cases} \tag{3.45}$$

where the input-output port-pair is given by $(u, y) = (T_m, \Omega_m)$ and can be rewritten $(u, y) = \left(K_m i_{out}, \frac{v_m}{K_e}\right)$, by solving the transducer equations from the electrical to the mechanical domain of the pump as described in (3.33).

3.1.4 Pumping Hydraulic PH Model

Fig. 3.7 shows a hydraulic pumping system that drives the water from the lower to the upper reservoir across the recovery pipe.

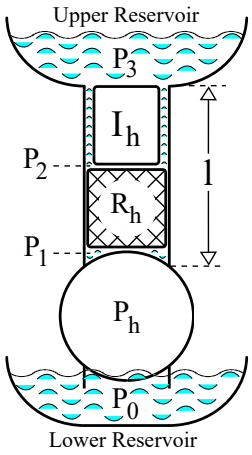

Figure 3.7: Equivalent hydraulic diagram of the pipe system.

The system's dynamic can be written as

$$I_h \dot{Q}_h = -R_h Q_h - P_{30} - \rho g l + P_h \tag{3.46}$$

where I_h represents the hydraulic inertance, Q_h represents the hydraulic flow of water across the pipe, R_h the hydraulic resistance, P_{30} the differential pressure from the upper to the lower reservoir, ρ the density of water, g the gravity force constant, l the length from the upper to the lower reservoir and P_h the pressure from the pump engine. From (3.34) and (3.32) we solve P_h, and (3.46) is rewritten as

$$\dot{Q}_h = -\alpha \Gamma Q_h - \frac{(P_{30} + \rho g l)}{\alpha} + \frac{K_h}{\alpha} T_m, \tag{3.47}$$

where α represents an apparent mass inertia and Γ joined together the dissipative elements of the hydraulic system. α and Γ are given by

$$\alpha = K_h^2 J_m + I_h, \qquad \Gamma = \frac{R_h + K_h^2 B_m}{\alpha^2}. \tag{3.48}$$

Furthermore, the dynamics of the pressure P_{30} in Fig. 3.7 it can be considered

$$\dot{P}_{30} = \frac{1}{C_h} Q_h, \tag{3.49}$$

and a Hamiltonian function $H_h\left(Q_h, P_{30}\right)$ given by

$$H_h\left(Q_h, P_{30}\right) = \frac{1}{2}\alpha Q_h^2 + \frac{1}{2} C_h P_{30}^2 + C_h P_{30} \rho g l. \tag{3.50}$$

complemented by its partial-derivatives in terms of the state variables Q_h and P_{30}

$$\nabla_{Q_h} H_h\left(Q_h, P_{30}\right) = \alpha Q_h, \quad \nabla_{P_{30}} H_h\left(Q_h, P_{30}\right) = C_h\left(P_{30} + \rho g l\right). \tag{3.51}$$

Thus, the dynamics in (3.47) and (3.49) are redefine from (3.51) as

$$\dot{Q}_h = -\Gamma \nabla_{Q_h} H_h\left(Q_h, P_{30}\right) - \frac{1}{\alpha C_h} \nabla_{P_{30}} H_h\left(Q_h, P_{30}\right) + \frac{K_h}{\alpha} T_m, \tag{3.52}$$

$$\dot{P}_{30} = \frac{1}{\alpha C_h} \nabla_{Q_h} H_h\left(Q_h, P_{30}\right). \tag{3.53}$$

Subsequently, we can formulate the dynamics of the hydraulic pumping system in the PH framework Σ_h, based on (3.50), (3.51), (3.52) and (3.53), such that

$$\Sigma_h \begin{cases} \underbrace{\begin{bmatrix} \dot{Q}_h \\ \dot{P}_{30} \end{bmatrix}}_{\dot{x}_h} = \underbrace{\begin{bmatrix} -\Gamma & \frac{-1}{\alpha C_h} \\ \frac{1}{\alpha C_h} & 0 \end{bmatrix}}_{\mathcal{J}(x_h) - \mathcal{R}(x_h)} \underbrace{\begin{bmatrix} \nabla_{Q_h} H_h\left(Q_h, P_{30}\right) \\ \nabla_{P_{30}} H_h\left(Q_h, P_{30}\right) \end{bmatrix}}_{\nabla_{x_h} H_h(x_h)} + \underbrace{\begin{bmatrix} \frac{K_h}{\alpha} \\ 0 \end{bmatrix}}_{g(x_h)} T_m \\ y_h = g^{\top}\left(x_h\right) \nabla_{x_h} H_h\left(x_h\right) = \Omega_m, \end{cases} \tag{3.54}$$

with an input-output port-pair $(u, y) = (T_m, \Omega_m)$.

3.1.5 PHS System PH Model

The complete PH system Σ_{phs} of the PHS model can be inferred from the stages formulations in (3.12), (3.22), (3.31), (3.45) and (3.54).

$$
\Sigma_{phs}\begin{cases}
\underbrace{\begin{bmatrix} \dot{q}_p \\ \dot{\phi}_p \\ \dot{q}_C \\ \dot{\phi}_L \\ \dot{\phi}_m \\ \dot{q}_m \\ \dot{p}_m \\ \dot{\varphi}_m \\ \dot{Q}_h \\ \dot{P}_{30} \end{bmatrix}}_{\dot{x}_{phs}} = \underbrace{\begin{bmatrix} \frac{-1}{R_p} & -1 & 0 & -S_{buck} & 0 & 0 & 0 & 0 & 0 & 0 \\ 1 & 0 & 0 & 0 & 0 & 0 & 0 & 0 & 0 & 0 \\ 0 & 0 & 0 & 1 & -1 & 0 & 0 & 0 & 0 & 0 \\ S_{buck} & 0 & -1 & -S_{buck}R_p & 0 & 0 & 0 & 0 & 0 & 0 \\ 0 & 0 & 1 & 0 & -R_m & -1 & -K_e & 0 & 0 & 0 \\ 0 & 0 & 0 & 0 & 1 & 0 & 0 & 0 & 0 & 0 \\ 0 & 0 & 0 & 0 & K_m & 0 & -\gamma_m & -1 & 0 & 0 \\ 0 & 0 & 0 & 0 & 0 & 0 & 1 & 0 & 0 & 0 \\ 0 & 0 & 0 & 0 & 0 & 0 & 0 & 0 & -\Gamma_h & \frac{-1}{\alpha C_h} \\ 0 & 0 & 0 & 0 & 0 & 0 & 0 & 0 & \frac{1}{\alpha C_h} & 0 \end{bmatrix}}_{\mathcal{J}(x_{phs})-\mathcal{R}(x_{phs})} \underbrace{\begin{bmatrix} \nabla_{q_p} H_{phs} \\ \nabla_{\phi_p} H_{phs} \\ \nabla_{q_C} H_{phs} \\ \nabla_{\phi_L} H_{phs} \\ \nabla_{\phi_m} H_{phs} \\ \nabla_{q_m} H_{phs} \\ \nabla_{p_m} H_{phs} \\ \nabla_{\varphi_m} H_{phs} \\ \nabla_{Q_h} H_{phs} \\ \nabla_{P_{30}} H_{phs} \end{bmatrix}}_{\nabla_{x_{phs}} H_{phs}(x_{phs})} \\
\quad + \underbrace{\begin{bmatrix} 1 \\ 0 \\ 0 \\ 0 \\ 0 \\ 0 \\ 0 \\ 0 \\ 0 \\ 0 \end{bmatrix}}_{g_1(x_m)} i_s(E_e) + \underbrace{\begin{bmatrix} 0 \\ 0 \\ 0 \\ 0 \\ 0 \\ 0 \\ \frac{-1}{K_h} \\ 0 \\ 0 \\ 0 \end{bmatrix}}_{g_2(x_m)} (P_{30}+\rho g l) + \underbrace{\begin{bmatrix} 0 \\ 0 \\ 0 \\ 0 \\ 0 \\ 0 \\ 0 \\ 0 \\ \frac{K_h}{\alpha} \\ 0 \end{bmatrix}}_{g_3(x_m)} T_m, \\
y_{m1} = {g_1}^{\top}(x_m)\nabla_{x_m} H_m(x_m) = v_p, \\
y_{m2} = {g_2}^{\top}(x_m)\nabla_{x_m} H_m(x_m) = \frac{-1}{K_h}\frac{p_m}{\beta_m} = \frac{-1}{K_h}\Omega_m = -Q_h, \\
y_{m3} = {g_3}^{\top}(x_m)\nabla_{x_m} H_m(x_m) = K_h Q_h = \Omega_m,
\end{cases} \tag{3.55}
$$

3.2 Simulation Results

For simulation purposes, we get key constants from the PV cell datasheet SURANA $SLV-175$ [125], following the modeling approach of Fig. 2.1 to solve the terms in (2.1) and (2.2) according to the guidelines of [126], i.e.,

$$
i_{pv} = i_{ph}(E_e) - i_0\left(\exp\left(\frac{v_{pv}+i_{pv}R_s}{a}\right)-1\right) - \frac{v_{pv}+i_{pv}R_s}{R_p}, \tag{3.56}
$$

where $\alpha = nV_t$ and i_0 are considered as constant values. Table 3.1 shows all parameters we have used through modeling the system stages.

Table 3.1: Key parameters of the PHS system

Parameter description	***Magnitude***
Temperature T[a]	25 °C
Irradiance E_{nom}[a]	1000 W/m^2
Output Power $P_{pv,nom}$[a]	175.0 W
Short-circuit current $I_{SC,nom}$[a]	7.6 A
Open-circuit voltage $V_{OC,nom}$[a]	32.8 V
Output current $I_{nom}@MPP$[a]	6.6 A
Output voltage $V_{nom}@MPP$[a]	26.7 V
Temperature coefficient of $V_{OC,nom}$[a]	-0.35% °C
Temperature coefficient of $I_{SC,nom}$[a]	0.05% °C
Temperature coefficient of $P_{pv,nom}$[a]	0.46% °C
Constant α[b]	1.148 V
Saturation current i_0[b]	250 nA
PV cell series resistor R_s[b]	18.85 mΩ
PV cell shunt resistor R_p[b]	$38,984$ Ω
PV cell equivalent capacitance C_{pv}	2.5 μF
Number of series cells N_s	1
Number of parallel cells N_p	2
DC-DC buck capacitor C_1	14.1 mF
DC-DC buck inductor L_1	2 mH
Armature inductanceL_m[c]	1.42 mH
Armature resistance R_m[c]	1.3 mΩ
Torque constant K_m[c]	0.059 Nm/A
Voltage constant K_e[c]	0.059 V/s
Hydraulic capacitance C_h[d]	2.6 g/(ms)^4
Hydraulic inertance I_h[e]	$2.03x10^7$ kg/m^4
Hydraulic resistance R_h[f]	$9.28x10^5$ kg/(m^{4}s)
Speed-flow constant K_h[g]	$1.91x10^5$ rad/m^3
Nominal angular speed Ω_{nom}[h]	55 rev/s
Nominal flow Q_{nom}[h]	$1.81x10^{-3}$ m^3/s
Water density ρ	998.2 kg/m^3
Gravity constant g	9.81 m/s^2
Water viscosity μ	890 μNm/s^2
Pipe length l	10 m
Pipe diameter d	25 mm

[a] From PV cell SURANA SVL-175 datasheet [125]

[b] Estimated as in [126]

[c] From DC-Motor M48x60/I5 datasheet [127]

[d] $C_h = A_R/(\rho g)$, A_R a reservoir estimated area of 25m^2

[e] $I_h = \rho l/A_p$, with A_p the area of pipe cross section

[f] $R_h = 8\pi\mu l/A_p^2$, from Poiseuille law

[g] $K_h = 2\pi\Omega_{nom}/Q_{nom}$

[h] Form Water Pump MARSROCK RD9024 datasheet [128]

For any simulation, the solar irradiance E_e was fixed at 1000 W/m^2. Added, the duty cycle D of the switch S_{buck} of DC-DC buck converter was adjusted at 50%, 66%, 75% and 90%, to compare the response of the system for each case. Hence, the response at the output of the DC-DC buck converter in terms of the output voltage v_{out} and the output power P_{out} is shown in Fig. 3.8, together with the storage water volume V_h in the upper reservoir. All v_{out}, P_{out}, and V_h responses of the Fig. increase as the duty cycle D increases. However, the improvement of v_{out} and P_{out} in the segment $75\% < D < 90\%$ becomes almost negligible. Furthermore, when the duty cycle $D = 50\%$, the storage water volume $Q_h \to 0$.

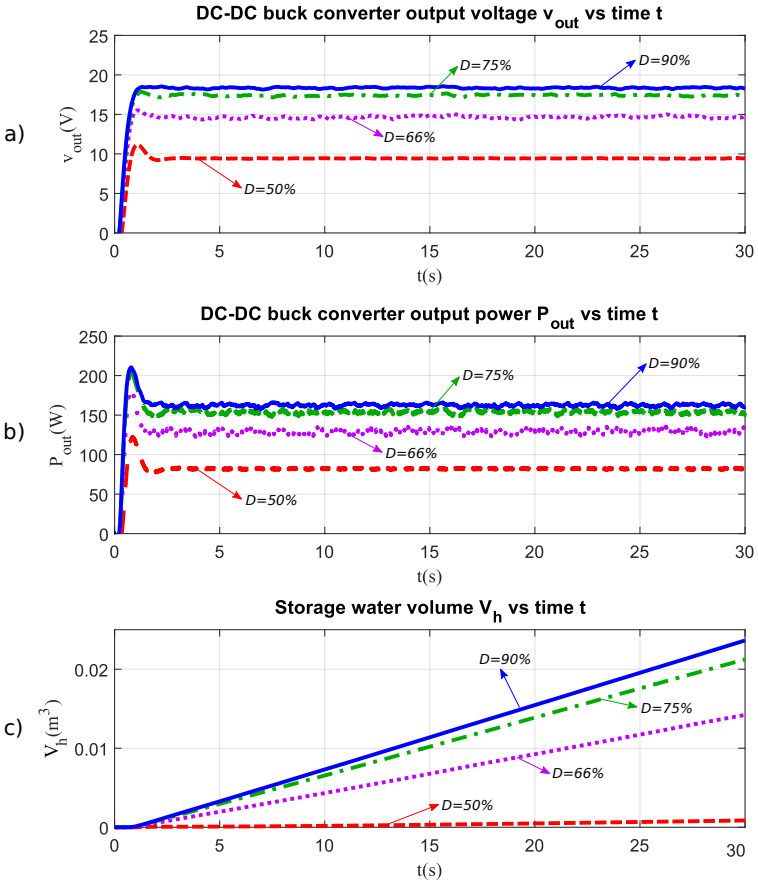

Figure 3.8: DC-DC buck converter output voltage v_{out} and output power P_{out}, and storage water volume V_h in the upper reservoir, for several duty cycles D of the switch S_{buck} at a constant input irradiance $E_e = 1000$ W/m^2.

3.3 Concluding Remarks and Future Work

We successfully modeled and simulated a solar-powered pumped-hydro system to recover potential energy from the water under constant solar radiation ideal conditions. In this system, a PV cell stage feeds a DC pump across a DC-DC buck converter in an open-loop proposal. We chose a port-Hamiltonian energy-based framework to model the multi-physic system domain. According to simulation results, the system responses of the stages'

state variables could be enhanced by controlling the switching behavior in the DC-DC buck converter, i.e., MPPT or VR control strategies.

This Chapter proposed modeling a PHS under the PH framework, demonstrating the transparent interpretation of the state variables, the physical parameters, and their interrelationship across the system stages. Further, we developed a system of a PV cell interconnected to a DC-DC converter. We proposed a nonlinear control to solve the MPPT by controlling the switching state of the DD-DC converter.

Chapter 4

Current Sensorless Control Strategy for the MPPT of a PV Cell: An Energy-Based Approach

This Chapter reports a novel energy-based modeling and control strategy developed and implemented to solve the MPPT issue of a PV cell array connected to consumption loads, as in [34]. Consequently, we propose a PH framework mathematical model that contains critical characteristic parameters of a PV cell array connected to an energy converter stage. This formalism is adopted here since the system integrates energy storage and dissipating elements (inter)connected across input-output power port pairs, becoming a natural and intuitive modeling approach that allows a simple physical interpretation of the system's energy flow towards a robust and scalable control design. A current-sensorless control algorithm is designed in the framework of an IDA-PBC strategy. This algorithm can track the local MPP under variations of solar irradiance and output loads. The control monitors the PV cell's output voltage and the solar irradiance to match the impedance between two stages, the PV cell output and a DC-DC boost converter system. Since the control is based on sensing irradiance as a control input, the strategy allows governing several PV cells with a single control per stage with the same irradiance sensor, decreasing the cost of sensing devices. The performance of the proposed strategy is compared to a (classical) Sliding Mode Control (SMC) law via simulation. Moreover, our energy-based strategy is implemented in a hardware platform with a sampling rate of 122 Hz, resulting in lower dynamic power consumption demand than other MPPT control strategies.

4.1 Mathematical Modeling of the PV cell and DC-DC boost converter stages

Fig. 4.1 depicts a detailed block diagram of the system's PV cell and DC-DC boost converter stages. The whole system can be considered into the electrical domain, where the irradiance of the sun E_e and the DC-DC boost converter output voltage v_{out} are the system's input and output.

The next section defines a PH approach to the PV cell modeling problem.

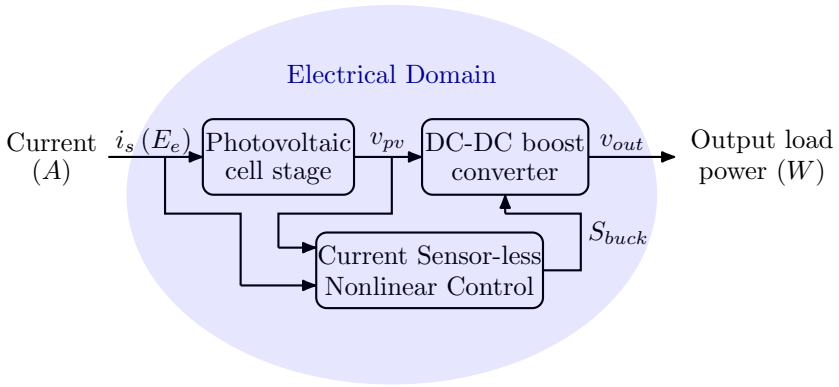

Figure 4.1: Energy storage and control system's block diagram and related physical domains.

4.1.1 Photovoltaic Cell PH Modeling

The PV cell model is based on the equivalent circuit in Fig. 4.2 Considering the KCL on

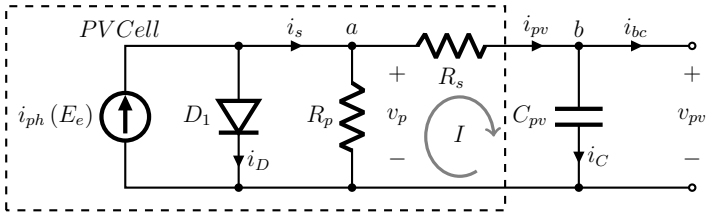

Figure 4.2: Electric diagram of the PV cell with an output DC-link capacitor C_{pv}.

node a of the equivalent circuit, we define

$$i_{pv} = i_s(E_e) - \frac{v_p}{R_p}, \tag{4.1}$$

where $i_s(E_e) = i_{ph}(E_e) - i_D$. Moreover, the KVL over the close path I yields

$$v_p = v_{pv} + R_s i_{pv} \tag{4.2}$$

and solving (4.2) in (4.1)

$$\begin{aligned} i_{pv} =& i_s(E_e) - \frac{v_{pv}}{R_p} - \frac{R_s}{R_p} i_{pv}, \\ =& \frac{R_p}{R_p + R_s} i_s(E_e) - \frac{1}{R_p + R_s} v_{pv}. \end{aligned} \tag{4.3}$$

Likewise, from the equivalent circuit's node b, we know that

$$i_C = i_{pv} - i_{bc}, \tag{4.4}$$

$$C_{pv}\dot{v}_{pv} = i_{pv} - i_{bc}. \tag{4.5}$$

We define the electrical charge q_{pv} in terms of the PV cell output voltage v_{pv} and the capacitor C_{pv} as a state variable, such that $q_{pv} = C_{pv} v_{pv}$, then (4.5) could be rewritten in terms of (4.3), and the dynamics of the electrical charge is expressed

$$\dot{q}_{pv} = -\frac{1}{R_p + R_s}\frac{q_{pv}}{C_{pv}} + \frac{R_p}{R_p + R_s} i_s\left(E_e\right) - i_{bc}. \tag{4.6}$$

We realize the system's second state variable that represents the electrical *flux*, i.e. ϕ_{pv}, whose dynamics are given by

$$\dot{\phi}_{pv} = \frac{q_{pv}}{C_{pv}}. \tag{4.7}$$

Since the capacitor C_{pv} is the only energy-storing element of the system in Fig. 2.1, then the Hamiltonian function $H_{pv}\left(q_{pv}, \phi_{pv}\right)$ of the PV cell stage is determined

$$H_{pv}\left(q_{pv}, \phi_{pv}\right) = \frac{1}{2C_{pv}} q_{pv}^2 \tag{4.8}$$

and the partial-derivatives of the Hamiltonian function in terms of the state variables q_{pv} and ϕ_{pv} are

$$\nabla_{q_{pv}} H_{pv}\left(q_{pv}, \phi_{pv}\right) = \frac{q_{pv}}{C_{pv}}, \tag{4.9}$$

$$\nabla_{\phi_{pv}} H_{pv}\left(q_{pv}, \phi_{pv}\right) = 0. \tag{4.10}$$

Hence, the dynamics in (4.6) and (4.7) can be reformulated in terms of $\nabla_{q_{pv}} H_{pv}$ and $\nabla_{\phi_{pv}} H_{pv}$ as

$$\dot{q}_{pv} = -\frac{1}{R_p + R_s}\nabla_{q_{pv}} H_{pv} + k\nabla_{\phi_{pv}} H_{pv} + \frac{R_p}{R_p + R_s} i_s\left(E_e\right) - i_{bc}, \tag{4.11}$$

$$\dot{\phi}_{pv} = \nabla_{q_{pv}} H_{pv}, \tag{4.12}$$

where $k = -1$ to keep the *skew-symmetric* properties of a $\mathcal{J}\left(x_{pv}\right)$ matrix to be defined later on. The energy function (4.8) together with the dynamics in (4.11) and (4.12), are utilized to formulate the PH system Σ_{PV} of the PV cell, given by

$$\Sigma_{PV}\begin{cases} \underbrace{\begin{bmatrix} \dot{q}_{pv} \\ \dot{\phi}_{pv} \end{bmatrix}}_{\dot{x}_{pv}} = \underbrace{\begin{bmatrix} -\dfrac{1}{R_p + R_s} & -1 \\ 1 & 0 \end{bmatrix}}_{\mathcal{J}(x_{pv}) - \mathcal{R}(x_{pv})} \underbrace{\begin{bmatrix} \nabla_{q_{pv}} H_{pv} \\ \nabla_{\phi_{pv}} H_{pv} \end{bmatrix}}_{\nabla_{x_{pv}} H_{pv}} \\ \qquad\qquad + \underbrace{\begin{bmatrix} \dfrac{R_p}{R_p + R_s} \\ 0 \end{bmatrix}}_{g(x_{pv})} i_s\left(E_e\right) - \begin{bmatrix} 1 \\ 0 \end{bmatrix} i_{bc}, \\ y_{pv} = g^{\top}\left(x_{pv}\right) \nabla_{x_{pv}} H_{pv} = v_p. \end{cases} \tag{4.13}$$

being $\mathcal{R}(x_{pv}) = \text{diag}\left(\frac{1}{R_p + R_s}, 0\right)$, and $\mathcal{J}(x_{pv})$ a skew-symmetric matrix with the form

$$\mathcal{J}(x_{pv}) = \begin{bmatrix} 0 & -1 \\ 1 & 0 \end{bmatrix}. \tag{4.14}$$

From the the dynamics of (4.13) with an input-output port-pair $(u_{pv}, y_{pv}) = (i_s, v_p)$ and the Hamiltonian (4.8), the power balance (2.13) holds since $R_p + R_s \geq 0$.

To continue, it is now necessary to find an expression to track the amplitude of v_{pv} according to the solar irradiance E_e to obtain the so-called *current-sensorless* control strategy. Such expression is developed in the following subsection.

4.1.2 Equilibrium Trajectory of the PV Cell State Variables Over the MPP

The function to track the amplitude of v_{pv} in terms of the solar irradiance E_e relies on the amplitude of the input current $i_{ph}(E_e)$ as in (2.1) and can be defined from the relationship between the transfer function of i_{pv} vs v_{pv} and the MPP of the PV cell, given in terms of the output power $P_{out}(v_{pv})$ such that

$$\nabla_{v_{pv}} P_{out}\left(v_{pv}^*\right) = \nabla_{v_{pv}}\left(i_{pv} v_{pv}\right)\Big|_{v_{pv}^*} = 0, \tag{4.15}$$

$$\nabla_{v_{pv}}\left(\left(i_{ph}(E_e) - i_0\left(\exp\left(\frac{v_p}{nV_t}\right) - 1\right) - \frac{v_p}{R_p}\right) v_{pv}\right)\Big|_{v_{pv}^*} = 0, \tag{4.16}$$

where $v_p = v_{pv} + i_{pv}R_s$, and v_{pv}^* represents the equilibrium state of the PV cell voltage on the MPP. If the magnitude of resistance R_s is shallow compared to R_p, it can be considered $R_s \approx 0$. Assuming i_0 as a constant, thus (4.16) becomes

$$i_{ph} + i_0 - i_0 \exp\left(\frac{v_{pv}^*}{nV_t}\right) - v_{pv}^*\left(\frac{2}{R_p} + \frac{i_0 \exp\left(\frac{v_{pv}^*}{nV_t}\right)}{nV_t}\right) \approx 0, \tag{4.17}$$

where v_{pv}^* can be solved by numerical methods in terms of the input current $i_{ph}(E_e)$, i.e. the so-called *equilibrium trajectory*. Thus, the current $i_{ph}(E_e)$ depends on the solar irradiance E_e as in (2.1), so the equilibrium PV cell voltage v_{pv}^* in (4.17).

The mathematical PH framework modeling approach of the DC-DC boost converter stage is presented in the following subsection.

4.1.3 DC-DC Boost Converter Modelling Approach

A DC-DC boost converter configuration is selected for the step-up voltage conversion, governed by a switching control unit. The converter can draw the MPP from the PV cell by adjusting the duty cycle of the switch for given solar radiance levels. We refer to [129, 130]

and the references therein for further details regarding the working principles of the model. The DC-DC boost converter configuration circuit is shown in Fig. 4.3, where v_{pv} at the left side of the circuit represents the PV cell output voltage and R_L at the right side a resistive output load.

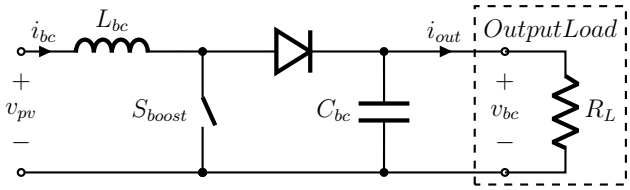

Figure 4.3: Electric diagram of the DC-DC boost converter governed by a normally close (NC) switch S_{boost}.

The DC-DC boost converter system is described by the dynamics of i_{bc} and v_{bc}. In addition to this, we define a two-state switching device represented by $S_{boost} = \{0, 1\}$. Further, the dynamics of i_{bc} and v_{bc} in terms of the state variables are given by $\phi_{bc} = L_{bc} i_{bc}$ (magnetic flux in the inductor), and $q_{bc} = C_{bc} v_{bc}$ (charge in the capacitor). By KCL and KVL, it follows that

$$\dot{q_{bc}} = -\frac{1}{R_L}\frac{q_{bc}}{C_{bc}} + S_{boost}\frac{\phi_{bc}}{L_{bc}}, \tag{4.18}$$

$$\dot{\phi}_{bc} = -S_{boost}\frac{q_{bc}}{C_{bc}} + v_{pv}. \tag{4.19}$$

The Hamiltonian function $H_{bc}(q_{bc}, \phi_{bc})$ of the DC-DC boost converter in Fig. 4.3 is defined as

$$H_{bc}(q_{bc}, \phi_{bc}) = \frac{1}{2C_{bc}} q_{bc}^2 + \frac{1}{2L_{bc}} \phi_{bc}^2, \tag{4.20}$$

and the respective partial-derivatives in terms of the state variables q_{pv} and ϕ_{pv} are given

$$\nabla_{q_{bc}} H_{bc}(q_{bc}, \phi_{bc}) = \frac{q_{bc}}{C_{bc}}, \tag{4.21}$$

$$\nabla_{\phi_{bc}} H_{bc}(q_{bc}, \phi_{bc}) = \frac{\phi_{bc}}{L_{bc}}. \tag{4.22}$$

Moreover, the dynamics in (4.18) and (4.19) are rewritten in terms of $\nabla_{q_{bc}} H_{bc}$ and $\nabla_{\phi_{bc}} H_{bc}$ as

$$\dot{q}_{bc} = -\frac{1}{R_L}\nabla_{q_{bc}} H_{bc} + S_{boost}\nabla_{\phi_{bc}} H_{bc}, \tag{4.23}$$

$$\dot{\phi}_{bc} = -S_{boost}\nabla_{q_{bc}} H_{bc} + v_{pv}, \tag{4.24}$$

and then, from (4.23) and (4.24) we formulate the PH system Σ_{BC} of the DC-DC boost

converter with an output load R_L as

$$\Sigma_{BC}\begin{cases}\underbrace{\begin{bmatrix}\dot{q}_{bc}\\ \dot{\phi}_{bc}\end{bmatrix}}_{\dot{x}_{bc}}=\underbrace{\begin{bmatrix}-\dfrac{1}{R_L} & S_{boost}\\ -S_{boost} & 0\end{bmatrix}}_{\mathcal{J}(x_{bc})-\mathcal{R}(x_{bc})}\underbrace{\begin{bmatrix}\nabla_{q_{bc}}H_{bc}\\ \nabla_{\phi_{bc}}H_{bc}\end{bmatrix}}_{\nabla_{x_{bc}}H_{bc}}\\ \qquad\qquad+\underbrace{\begin{bmatrix}0\\1\end{bmatrix}}_{g(x_{bc})}v_{pv},\\ y_{bc}=g^{\top}(x_{bc})\,\nabla_{x_{bc}}H_{bc}=i_{bc},\end{cases}\tag{4.25}$$

where $\mathcal{R}(x_{bc})=\operatorname{diag}\left(\dfrac{1}{R_L},0\right)$, and $\mathcal{J}(x_{bc})$ is a skew-symmetric matrix with that complies

$$\mathcal{J}(x_{bc})=\begin{bmatrix}0 & S_{bc}\\ -S_{bc} & 0\end{bmatrix}.\tag{4.26}$$

From the dynamics of of (4.25) with input-output port-pair $(u_{bc},y_{bc})=(v_{pv},i_{bc})$ and a Hamiltonian function (4.20), the power balance (2.13) is satisfied since $R_L>0$.

We describe the PV cell and the DC-DC boost converter in a single interconnected system for control design purposes.

4.1.4 The PV Cell Array and the DC-DC Boost Converter: an Energy-Based Approach

From the PH formulation of the PV cell modeling approach (4.13) and the DC-DC boost converter (4.25), and their Hamiltonian functions (4.8), and (4.20), we interconnect both stages in a single PH framework, rewriting a new system Σ

$$\Sigma\begin{cases}\underbrace{\begin{bmatrix}\dot{q}_{pv}\\ \dot{\phi}_{pv}\\ \dot{q}_{bc}\\ \dot{\phi}_{bc}\end{bmatrix}}_{\dot{x}}=\underbrace{\begin{bmatrix}-\dfrac{1}{R_p+R_s} & -1 & 0 & -1\\ 1 & 0 & 0 & 0\\ 0 & 0 & -\dfrac{1}{R_L} & S_{boost}\\ 1 & 0 & -S_{boost} & 0\end{bmatrix}}_{\mathcal{J}(x)-\mathcal{R}(x)}\underbrace{\begin{bmatrix}\nabla_{q_{pv}}H\\ \nabla_{\phi_{pv}}H\\ \nabla_{q_{bc}}H\\ \nabla_{\phi_{bc}}H\end{bmatrix}}_{\nabla_x H}\\ \qquad\qquad+\underbrace{\begin{bmatrix}\dfrac{R_p}{R_p+R_s}\\ 0\\ 0\\ 0\end{bmatrix}}_{g(x)}i_s(E_e),\\ y_I=g^{\top}(x)\,\nabla_x H=v_p,\end{cases}\tag{4.27}$$

where $\mathcal{J}(x) = \text{diag}(\mathcal{J}(x_{pv}), \mathcal{J}(x_{bc}))$, $\mathcal{R}(x) = \text{diag}(\mathcal{R}(x_{pv}), \mathcal{R}(x_{bc}))$, and the input-output port-pair $(u, y) = (i_s, v_p)$. The Hamiltonian function of Σ is defined as

$$H(x) = H_{pv}(q_{pv}, \phi_{pv}) + H_{bc}(q_{bc}, \phi_{bc}) = \frac{1}{2C_{pv}} q_{pv}^2 + \frac{1}{2C_{bc}} q_{bc}^2 + \frac{1}{2L_{bc}} \phi_{bc}^2, \tag{4.28}$$

and the power balance (2.13) for (4.27) also holds, since $\mathcal{R}(x) \succ 0$.

In the follow-up, we design our passivity-based MPPT control strategy based on the Σ structure.

4.2 Proposed Control Approach

A novel IDA-PBC design inspired by the work of [41, 115, 118], is introduced to control the interconnected system (4.27). The main design steps of this strategy are recapitulated in section 2.6. Moreover, the feedback function $\beta(x)$ in (2.16) is obtained to control the system (4.27). We compute the control requirements by following the statements of the IDA-PBC strategy, i.e., structure preservation (2.18), integrability (2.20), equilibrium assignment (2.21), and Lyapunov stability (2.22).

(i) **Structure preservation**. To simplify the structure, We assume that the matrix $J_a(x)$ is equal to zero and (2.16) is reduced in terms of $\mathcal{J}(x, \beta(x))$, $\mathcal{R}(x)$, $g(x)$, $R_a(x)$ and $\mathcal{K}(x)$, such that

$$\{[\mathcal{J}(x, \beta(x))] - [\mathcal{R}(x) + \mathcal{R}_a(x)]\} \mathcal{K}(x) = -[\mathcal{R}_a(x)] \nabla_x H(x) + g(x, \beta(x)), \tag{4.29}$$

where $g(x, \beta(x)) = g(x) i_s$, being i_s the input of the system (4.27). To simplify the left side of (4.29), $R_a(x)$ is assumed as

$$\mathcal{R}_a = \begin{bmatrix} 1 - \dfrac{1}{R_p + R_s} & 0 & 0 & 0 \\ 0 & 0 & 0 & 0 \\ 0 & 0 & 1 - \dfrac{1}{R_L} & 0 \\ 0 & 0 & 0 & 0 \end{bmatrix}, \tag{4.30}$$

and (4.29) becomes

$$\underbrace{\begin{bmatrix} -1 & -1 & 0 & -1 \\ 1 & 0 & 0 & 0 \\ 0 & 0 & -1 & S_{boost} \\ 1 & 0 & -S_{boost} & 0 \end{bmatrix}}_{[\mathcal{J}(x,\beta(x))]-[\mathcal{R}(x)+\mathcal{R}_a(x)]} \mathcal{K}(x) =$$

$$-\underbrace{\begin{bmatrix} 1-\dfrac{1}{R_p+R_s} & 0 & 0 & 0 \\ 0 & 0 & 0 & 0 \\ 0 & 0 & 1-\dfrac{1}{R_L} & 0 \\ 0 & 0 & 0 & 0 \end{bmatrix}}_{\mathcal{R}_a(x)} \underbrace{\begin{bmatrix} \dfrac{q_{pv}}{C_{pv}} \\ 0 \\ \dfrac{q_{bc}}{C_{bc}} \\ \dfrac{\phi_{bc}}{L_{bc}} \end{bmatrix}}_{\nabla_x H(x)} + \underbrace{\begin{bmatrix} \dfrac{R_p}{R_p+R_s} i_s(E_e) \\ 0 \\ 0 \\ 0 \end{bmatrix}}_{g(x,\beta(x))}. \tag{4.31}$$

Since we assume $[\mathcal{J}(x,\beta(x))]-[\mathcal{R}(x)+\mathcal{R}_a(x)]$ invertible, we can solve the matrix $\mathcal{K}(x)$ in (4.31) as

$$\mathcal{K}(x) = \begin{bmatrix} \mathcal{K}_1(x) \\ \mathcal{K}_2(x) \\ \mathcal{K}_3(x) \\ \mathcal{K}_4(x) \end{bmatrix} = \begin{bmatrix} 0 \\ \dfrac{R_{p,s}-1}{R_{p,s}}\dfrac{q_{pv}}{C_{pv}} + \dfrac{R_p}{R_{p,s}} i_s(E_e) - \dfrac{R_L-1}{\beta(x)R_L}\dfrac{q_{bc}}{C_{bc}} \\ 0 \\ \dfrac{R_L-1}{\beta(x)R_L}\dfrac{q_{bc}}{C_{bc}} \end{bmatrix}, \tag{4.32}$$

where $R_{p,s} = R_p + R_s$. The form of the vector function $\mathcal{K}(x)$ in (4.32) guarantees the structure preservation properties of the closed-loop system as in (2.15).

(*ii*) **Integrability**. $\mathcal{K}(x)$ obtained on (4.32) is now computed to comply the condition (2.20) as

$$\begin{bmatrix} 0 & 0 & 0 & 0 \\ \nabla_{q_{pv}}\mathcal{K}_2 & \nabla_{\phi_{pv}}K_2 & \nabla_{q_{bc}}\mathcal{K}_2 & \nabla_{\phi_{bc}}\mathcal{K}_2 \\ 0 & 0 & 0 & 0 \\ \nabla_{q_{pv}}\mathcal{K}_4 & \nabla_{\phi_{pv}}\mathcal{K}_4 & \nabla_{q_{bc}}\mathcal{K}_4 & \nabla_{\phi_{bc}}\mathcal{K}_4 \end{bmatrix} = \begin{bmatrix} 0 & \nabla_{q_{pv}}\mathcal{K}_2 & 0 & \nabla_{q_{pv}}\mathcal{K}_4 \\ 0 & \nabla_{\phi_{pv}}\mathcal{K}_2 & 0 & \nabla_{\phi_{pv}}\mathcal{K}_4 \\ 0 & \nabla_{q_{bc}}\mathcal{K}_2 & 0 & \nabla_{q_{bc}}\mathcal{K}_4 \\ 0 & \nabla_{\phi_{bc}}\mathcal{K}_2 & 0 & \nabla_{\phi_{bc}}\mathcal{K}_4 \end{bmatrix} \tag{4.33}$$

and from (4.33) it holds

$$\begin{aligned} \nabla_{q_{pv}}\mathcal{K}_2(x) = \nabla_{q_{bc}}\mathcal{K}_2(x) = 0 \\ \nabla_{q_{pv}}\mathcal{K}_4(x) = \nabla_{q_{bc}}\mathcal{K}_4(x) = 0 \\ \nabla_{\phi_{bc}}\mathcal{K}_2(x) = \nabla_{\phi_{pv}}\mathcal{K}_4(x). \end{aligned} \tag{4.34}$$

The third line in (4.34) is equal to zero since $\mathcal{K}_2(x)$ and $\mathcal{K}_4(x)$ are independent of the flux terms ϕ_{bc} and ϕ_{pv}. Assuming that the voltage in the serial equivalent resistor R_s, i.e., $R_s i_{pv}$,

is very low respect to v_{pv}, and since the current $i_s(E_e)$ on Fig. 2.1 is a function of q_{pv} (as defined in (2.2) and (2.1)), one solution for the vector $\mathcal{K}(x)$ comes from the differentiation

$$\begin{aligned} \nabla_{q_{pv}}\mathcal{K}_2(x) &= 0, \\ \frac{R_{p,s}-1}{R_{p,s}C_{pv}} - \frac{R_p i_0}{R_{p,s}C_{pv}nV_t}\exp\left(\frac{q_{pv}}{C_{pv}nV_t}\right) - \frac{R_L-1}{R_L}\frac{q_{bc}}{C_{bc}}\frac{\nabla_{q_{pv}}\beta(q_{pv})}{\beta(q_{pv})^2} &= 0. \end{aligned} \tag{4.35}$$

A solution to the PDE in (4.35) to preserve the structure result in (4.29) and to comply with the integrability condition is given by

$$\beta(q_{pv}) = \frac{-\left(\frac{R_L-1}{R_L}\right)v_{bc}}{C_1 - \frac{R_{p,s}-1}{R_{p,s}}v_{pv} - \frac{R_p}{R_{p,s}}i_0\exp\left(\frac{v_{pv}}{nV_t}\right)}, \tag{4.36}$$

with C_1 in (4.36) a term to be defined to accomplish the equilibrium assignment and Lyapunov stability.

(*iii*) **Equilibrium assignment at stable equilibrium** x^*. Based on the Hamiltonian of (4.28), it can be determined that

$$\nabla_x H\left(q_{pv}^*, \phi_{pv}^*, q_{bc}^*, \phi_{bc}^*\right) = \text{col}\left[\frac{q_{pv}^*}{C_{pv}}, 0, \frac{q_{bc}^*}{C_{bc}}, \frac{\phi_{bc}^*}{L_{cb}}\right], \tag{4.37}$$

where $x^* = \left(q_{pv}^*, \phi_{pv}^*, q_{bc}^*, \phi_{bc}^*\right)$ represent the equilibrium state of the system in (4.27). Onward, by evaluating (4.37) and (4.32) at x^* and equalizing according to the *Equilibrium assignment* statement, we accomplish

$$\frac{R_{p,s}-1}{R_{p,s}}\frac{q_{pv}^*}{C_{pv}} + \frac{R_p}{R_{p,s}}i_s - \frac{R_L-1}{\beta(x)R_L}\frac{q_{bc}^*}{C_{bc}} = 0. \tag{4.38}$$

We finally recover (4.36) into (4.38) to solve C_1 complying with the equilibrium assignment. Moreover, we found two expressions that satisfy the solution, and we have labeled such expressions as C_{1A} and C_{1B}, such that

$$\begin{aligned} C_{1A} &= \left(\frac{2(R_{p,s}-1)}{R_{p,s}}\right)v_{pv}^* + \frac{R_p}{R_{p,s}}\left(i_{ph}(E_e) + i_0\right), \\ C_{1B} &= \left(\frac{-2R_pR_s}{R_p^2 - R_s^2}\right)v_{pv}^* + \frac{R_p}{R_{p,s}}i_0\exp\left(\frac{v_{pv}^*}{nV_t}\right). \end{aligned} \tag{4.39}$$

Notice how C_{1A} and C_{1B} in (4.39) depend on the equilibrium state v_{pv}^*, which in turn depend on $i_{ph}(E_e)$ and, consequently, on E_e.

(*iv*) **Lyapunov stability**. From the vector functions $\mathcal{K}(x)$ in (4.32) and $\nabla_x H(x^*)$ in (4.37), we solve the Lyapunov stability in (2.22) as

$$0 > -\left(\frac{1}{C_{pv}} + \frac{1}{C_{bc}} + \frac{1}{L_{bc}}\right). \tag{4.40}$$

and then, the inequality (4.40) complies with the stability statement, leading the close loop system to satisfy the MPP in the equilibrium trajectory described in (4.17).

4.2.1 IDA-PBC Switching Control Law

The DC-DC boost converter of Fig. 4.3 is considered as a lossless stage, controlled by the discrete set $S_{boost} = \{0, 1\}$, as explained by [131]. The exerted control law $\beta(q_p)$ drives the state of the switch S_{boost} in Fig. 4.3, turning between mode 0 or 1, to adjust the controller to the desired MPP trajectory. This trajectory follows the magnitude of the solar irradiance E_e to adjust the switching on a *threshold dynamic level*, according to a feedback reference. The dynamic threshold level is defined from the estimation of the scalar function $\beta(q_{pv})$ on the desired equilibrium point over the MPP trajectory, i.e., $\beta(q^*_{pv})$, with q^*_{pv} as the state value that reaches the MPP. Consequently, the PV cell output voltage v_{pv} at the desired MPP depends also on the charge, i.e. $v^*_{pv} = q^*_{pv}/C_{pv}$ as in (4.17). Since the current $i_{ph}(E_e)$ as in (2.1) depends on the solar irradiance E_e, then $\beta\left(q^*_{pv}\right)$ becomes a control parameter dynamically adjusted by the E_e. Hence, we define our primary switching control law in a proposition and remark as follows:

Proposition 2: *Given a system of a PV cell connected to a DC-DC boost converter represented in the PH framework as in* (4.27)*, whose duty cycle for the converter switch* S_{boost} *is defined by the permanence between two modes, such that* $0 \leq S_{boost} \leq 1$*, as in [132], then a designed control algorithm reaches the MPPT target via a scalar function* $\beta(x)$ *in* (4.36)*, which solves the PDE in* (2.16)*. Hence, inspired by [133, 131], the proposed control signal is given by*

$$S_{boost} = \begin{cases} 1 & \text{for} \quad \beta(q_{pv}) - \beta\left(q^*_{pv}\right) > 0 \\ 0 & \text{for} \quad \beta(q_{pv}) - \beta\left(q^*_{pv}\right) \leq 0, \end{cases} \tag{4.41}$$

being $\beta(q_{pv}) - \beta\left(q^*_{pv}\right)$ *an error tracking control, where* $\beta\left(q^*_{pv}\right)$ *is constantly adjusted by the state variables at the equilibrium point of the system as a dynamic threshold level that tracks the MPP trajectory.* ■

Proof. The Hamiltonian function $H_d(x, \beta(x))$ of the close loop PH system in (2.15) is given by

$$H_d(x, \beta(x)) = H_I(x, \beta(x)) + H_a(x, \beta(x)), \tag{4.42}$$

being $H_I(x, \beta(x))$ defined in (4.28) and $H_a(x, \beta(x))$ the energy of the desired controller. Thus, for the given $\beta(x)$; $\mathcal{J}(x, \beta(x))$; $\mathcal{R}(x)$; the solution of (4.29) is a gradient of the form

$$\mathcal{K}(x) = \nabla_x H_a(x, \beta(x)) \tag{4.43}$$

if and only if the integrability condition in (2.20) is satisfied. Furthermore, the system (2.15) reaches stability at the equilibrium point x^* on (4.17) laying over the MPP trajectory: firstly, the function $H_d(x, \beta(x))$ has an isolated extremum at x^* as shown in the equilibrium assignment condition on (4.39), since we solve it to satisfy (2.21); secondly, from the Lyapunov stability condition (4.40), we demonstrate that it is an isolated minimum of the function. Hence, we have demonstrated that $H_d(x, \beta(x))$ is a Lyapunov candidate function. □

We formulated in the Appendix H a specific type of SMC strategy for our PV cell plus the DC-DC boost converter system for the MPPT issue according to [132, 133], to compare the performance of our IDA-PBC control law (4.41) and the SMC strategy (H.6), via numerical simulations and an experimental setup.

4.3 Simulation results

We simulate the performance of the terms C_{1A} and C_{1B} of the control function $\beta(v_{pv})$, PV cell transfer and power functions, and the PV cell output power response under disturbances of solar irradiance and output impedance. Further, a behavioral multi-physics numerical model of the PH system (4.27) is developed and fed with the key parameters of Table 4.2 from section 4.4. Based on this numerical model, the control action of both strategies, our proposed IDA-PBC and the SMC over the PH system (4.27), are simulated and compared. To get accurate simulation results, the sampling of the states for the control strategies ($\{v_{pv}, E_e\}$ in IDA-PBC and $\{v_{pv}, i_{pv}\}$ in SMC is restricted in frequency into the programming code.

According to (4.36) and (4.39), the function $\beta(v_{pv})$ has a *discontinuous behaviour* in terms of C_{1A} and C_{1B}, at right and left side of a given equilibrium state v_{pv}^* respectively, as shown in Fig. 4.4. Consequently, to satisfy a continuous swept of the control law over the whole MPPT trajectory in (4.41), it can be established that C_{1A} must be applied to the control law (4.41) when the magnitude of $v_{pv}. \leq v_{pv}^*$ and C_{1B} in the case $v_{pv} > v_{pv}^*$.

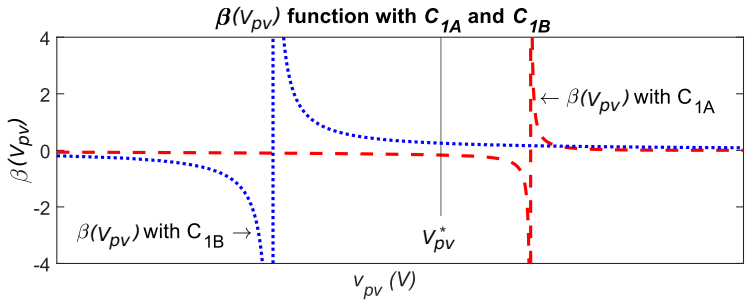

Figure 4.4: Function $\beta(v_{pv})$ behaviour dependance from the constants C_{1A} (dashed red line) and C_{1B} (dot blue line).

On the other hand, Fig. 4.5 shows the *transfer functions* i_{pv} vs v_{pv} in *a)* and P_{pv} vs v_{pv} in *b)* of a PV cell. The MPP trajectory track defined by the control function $\beta(v_{pv})$ relies on these transfer functions. Such characteristic curves are based on the dynamics of (2.2) to (2.4) and complemented with the critical parameters of the Table 4.2. The magnitude of v_{pv}, i_{pv} and P_{pv} are highlighted at the MPP for a solar irradiance $E_e = 1000$ W/m^2. The reliability of the control laws (4.41) and (H.6) is evaluated following the PV cell transfer functions' behavior.

The responses of the PV cell output power P_{pv} of the IDA-PBC and SMC strategies in Fig. 4.6 *b)*, are compared under *disturbances on the solar irradiance level* from 960 $\frac{W}{m^2}$ to 670 $\frac{W}{m^2}$, as in Fig. 4.6*a)*. The response of the PV cell's output power P_{pv} of both the IDA-PBC and the SMC have no perceptible differences. The simulation sample rate is set to 1 MHz for both control strategies to accomplish an SMC-suitable performance due to the extra-computation requirements for the differential equations calculation.

The IDA-PBC and the SMC strategies performance were simulated and compared, where the DC-DC boost converter load R_L behaves as an input time function, following a *step perturbation* from 10 Ω to 5 Ω (Fig. 4.7.*a*). For both the IDA-PBC and the SMC, the power signals P_{pv} remain unmovable (Fig. 4.7.*b*). Once more, the simulation sample rate of both

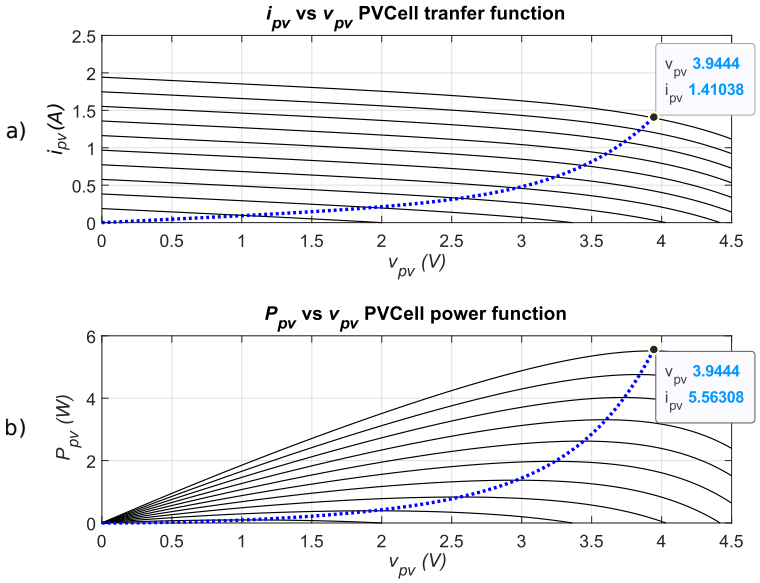

Figure 4.5: Simulated PV cell transfer functions of *a)* i_{pv} *vs* v_{pv} (solid black lines), and maximum power impedance function at MPP (blue dot line); and *b)* P_{pv} *vs* v_{pv} (solid black lines), and MPP trajectory (blue dot line), at irradiance levels given by steps of 100 $\frac{W}{m^2}$ from 100 to 1000 $\frac{W}{m^2}$.

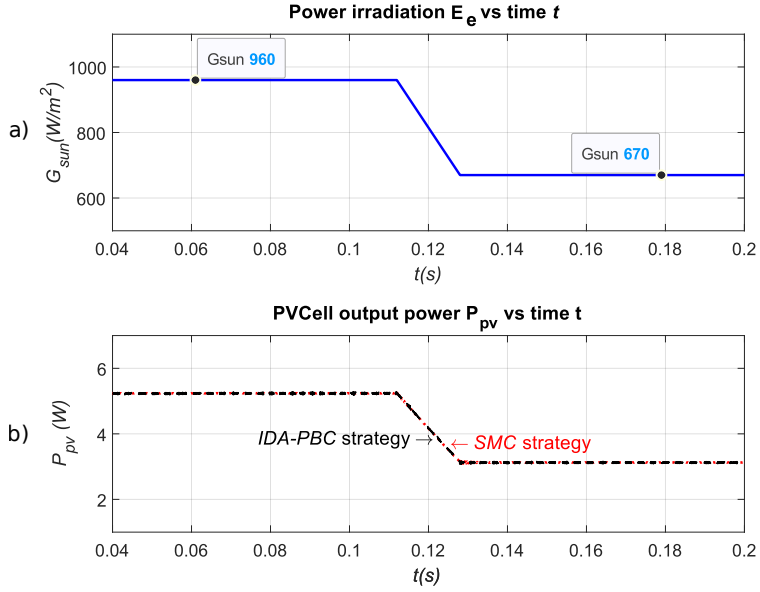

Figure 4.6: Simulation results of *b)* PV cell output power response P_{pv} with the IDA-PBC strategy (dark dashed line) and the SMC strategy (red dot line) to a given *a)* input irradiance step fluctiation $E_e = 960$ $\frac{W}{m^2}$ for the time interval $(0.040, 0.112)$ s and $E_e = 670$ $\frac{W}{m^2}$ for the time interval $(0.128, 0.200)$ s (blue solid line), with a fixed load of $R_L = 10$ Ω.

control strategies is set to 1 MHz due to the extra computation required by the SMC for the differential equations calculation.

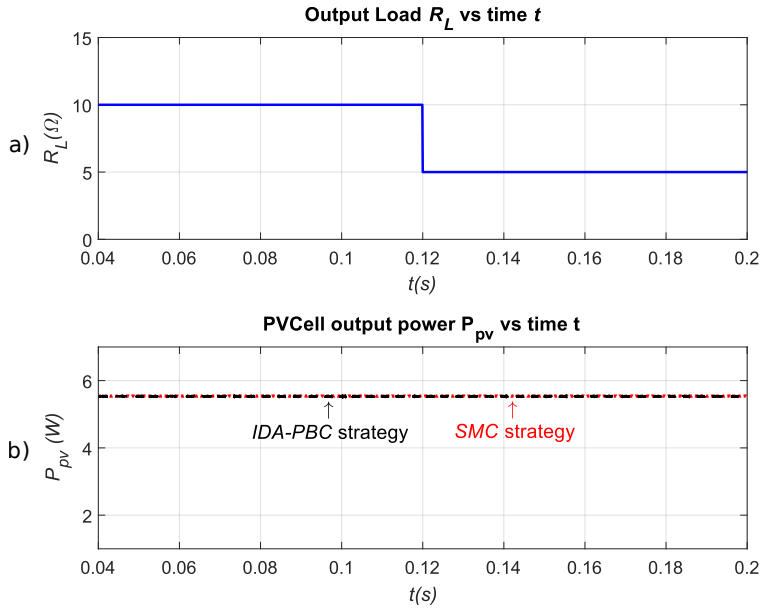

Figure 4.7: Simulation results of *b)* PV cell output power response P_{pv} with the IDA-PBC strategy (dark dashed line) and the SMC strategy (red dot line) to a given *a)* output load R_L step fluctuation from 10 Ω to 5 Ω at $t = 0.12$ s, under constant irradiance $E_e = 1000 \frac{W}{m^2}$.

Furthermore, the control performance of the IDA-PBC and SMC strategies was simulated regarding the switching frequency response, as shown in Fig. 4.8. The monitoring sampling frequency was set to 1 MHz in the simulation code for both cases. In *a)*, the switching action of the IDA-PBC strategy is more intermittent than the switching action of the SMC strategy in *b)* (IDA-PBC switches 32 time and SMC only 8 times in the same period). Hence, it can be considered that the IDA-PBC requires less computational resources than SMC strategy in terms of calculation to perform the switching control.

4.4 Experimental results

Fig. 4.9 depicts the experimental setup to verify the reliability of the MPPT control strategy, exerted by the suggested control function S_{boost} in (4.41) over the system Σ in (4.27). The control circuit to govern the the DC-DC boost converter's switching is a home-made designed, detailed in the Appendix F. Table 4.1 shows the setup hardware, equipment, and tools. To calibrate our irradiance sensor Spektron 210 [135], we have referred to sensor-reading real-time data from the website of the Costa Rican's National Meteorological Institute.

The physical parameters v_{pv} and i_{pv} were monitored from the set up shown in Fig. 4.9, under constant solar irradiances E_e of $\approx 1000 \frac{W}{m^2}$, $\approx 850 \frac{W}{m^2}$ and $\approx 700 \frac{W}{m^2}$. Simultaneously, an impedance sweep was induced with a load connected to the output of the PV cell to drive various matching conditions. Thus, we determine the experimental PV cell output

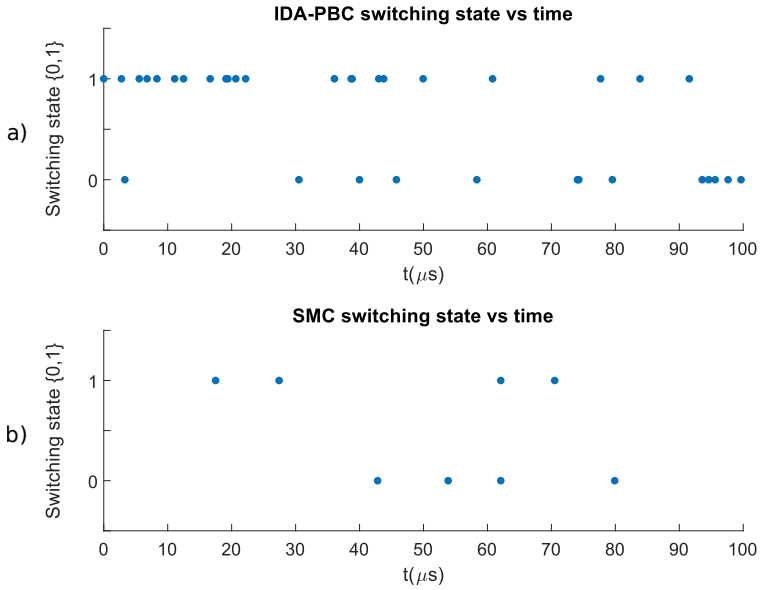

Figure 4.8: Simulation results of the switching performance for *a)* IDA-PBC and *b)* SMC strategies over a period of $100\mu s$.

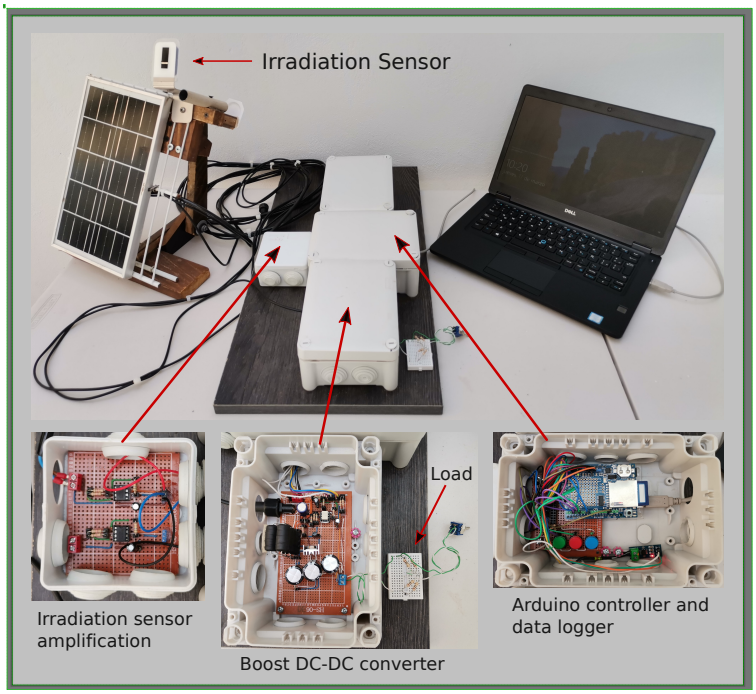

Figure 4.9: Prototype setup for physical experimental measurements of the current-sensorless system.

Table 4.1: Experimental setup hardware, equipment and tools

Name	***Model***	***Quantity***
PV cell *ZHIWANG* $30W$ [134]	$ZW-7W-6V-1$	1
Prototyping platform *Arduino UNO*	*Rev*3	1
Data logger shield *Adafruit*	*Adafruit*	1
Irradiance sensor *SPECTRON* [135]	210	1
Hall current sensor $5A$	$ACS712$	1
Multimeter *BK PRECISION*	393	1
Oscilloscope *BK PRECISION*	$2540C$	1
Laptop *DELL LATITUDE*	5491	1
Electronic components	N/A	N/A
Shielded enclosures	N/A	N/A

power function by fitting the PV cell output power P_{pv} at the MPP, as shown in Fig. 4.10. The MPP at $E_e = 1000\ \frac{W}{m^2}$ was experimentally estimated, resulting $P_{pv} \approx 5.7$ W when the voltage $v_{pv} \approx 4.0$ V and $i_{pv} \approx 1.41$ A, with $I_{SC,nom} \approx 1.95$ A and $V_{OC,nom} \approx 6.5$ V at the lowest and highest levels of the swept impedance matching. These parameters allow the PV cell's experimental characterization to improve the control reliability.

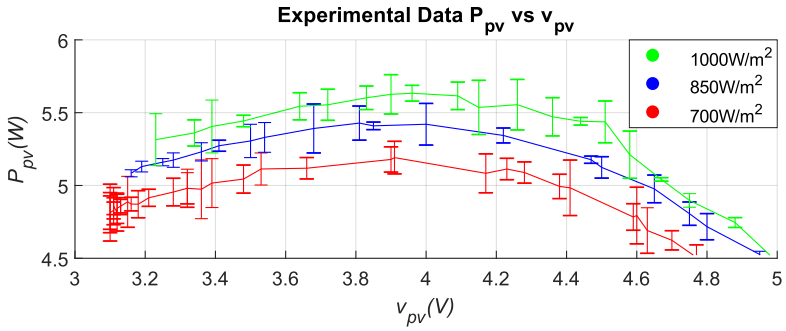

Figure 4.10: Experimental characterization of the PV cell output power transfer function P_{pv} vs P_{pv} at several irradiance levels E_e.

The modelling approach of (2.1), (2.2), (2.3) and (2.4) is simplified in (4.44) to evaluate the current i_{pv} following the guidelines of [126], to get key constants from the experimental PV cell data on Fig. 4.10 for simulation and control purposes,i.e.,

$$i_{pv} = i_{ph}\left(E_e\right) - i_0\left(\exp\left(\frac{v_{pv} + i_{pv}R_s}{a}\right) - 1\right) - \frac{v_{pv} + i_{pv}R_s}{R_p}, \tag{4.44}$$

where $a = nV_t$ and i_0 are considered as constant values. Table 4.2 summarizes the critical constants and the DC-DC boost converter design parameters.

The *frequency performance* of the switch S_{boost}, that controls the DC-DC boost converter under the IDA-PBC strategy, is evaluated to determine the maximum capabilities of the hardware platform Arduino UNO Rev3. To reach the maximum allowed frequency, a square signal cycle is executed from the Arduino UNO Rev3 over the switch S_{boost}. The executed

Table 4.2: Key parameters of the sensor-less system

Parameter description	***Magnitude***
Environment temperature T	30 °C
PV cell temperature T_v	30 °C
PV nominal irradiance G_{nom}	1000 kW/m^2
PV cell output short circuit $I_{SC,nom}$[a]	1.95 A
PV cell output open circuit $V_{OC,nom}$[a]	6.5 V
PV cell output $I_{nom}@MPP$[a]	1.42 A
PV cell output $V_{nom}@MPP$[a]	4.0 V
Saturation current i_0[b]	745 μA
Simplified constant a[b]	0.711 V
PV cell series resistor R_s[b]	43 mΩ
PV cell shunt resistor R_p[b]	11.28 Ω
PV cell DC-link capacitor C_{pv}	470 μF
DC-DC boost capacitor C_{bc}	14.1 mF
DC-DC boost inductor L_{bc}	2 mH

[a] Obtained experimentally @G_{nom} as in Fig. 4.10

[b] estimated as in [126]

code considers the delay time of the IDA-PBC algorithm. Fig. 4.11 shows the maximum reached a frequency of approximately 122 Hz (period of 8.21 ms). Furthermore,[136] establishes that the dynamic power dissipated on the digital circuit's clock cycle signals can be determined as

$$P = ACV^2F, \tag{4.45}$$

where A represents the activity factor of the switching, C the equivalent capacitance of the circuit, V the source voltage applied across the circuit, and F the working frequency. From (4.45), it can be considered that the dynamic switching power increases according to the magnitude of working frequency F. From Fig. 4.8, it was demonstrated via simulation that IDA-PBC performs at least four times faster than SMC strategy. If both strategies were evaluated into the same hardware platform, SMC would require a four times faster processing to perform as faster as the IDA-PBC, increasing the working frequency F of the controller and, consequently, the power of the controller according to (4.45).

Afterward, the response of the IDA-PBC strategy is evaluated by exposing the system setup in Fig. 4.9 firstly to a constant solar irradiance E_e. Subsequently, the PV cell ZHI-WANG ZW-7W-6V-1 [134] is rotated to generate an *irradiance step* from $E_e \approx 960\ \frac{W}{m^2}$ to $E_e \approx 670\ \frac{W}{m^2}$, as depicted in Fig. 4.12*a*. Hence, the response of the output power P_{pv} to the irradiance step is measured. Experimentally, Fig. 4.12*b* demonstrates that the IDA-PBC strategy implemented into the hardware Arduino UNO Rev3 effectively tracks the MPP, according to the irradiance trend lines of Fig. 4.12*a*.

Finally, the response of the IDA-PBC strategy is evaluated once more by inducing an *impedance step* from 10 Ω to 5 Ω at the output of the DC-DC boost converter, at a constant solar irradiance $E_e \approx 960\ \frac{W}{m^2}$, as shown in Fig. 4.13. The PV cell output power P_{pv} remains stable around 5.5 W when exposed to load disturbances (Fig. 4.13*b*). Such results in Fig.

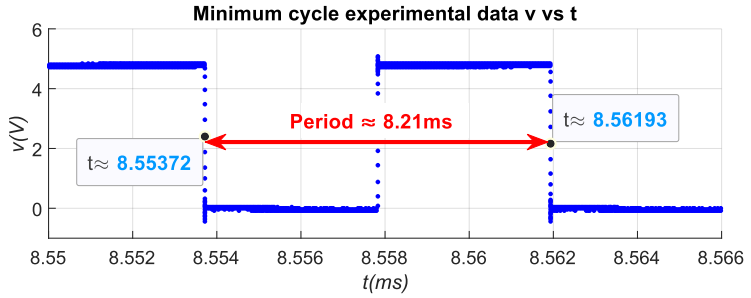

Figure 4.11: Minimum period of sampling cycle of the IDA-PBC strategy due to the physical restrictions of the hardware platform.

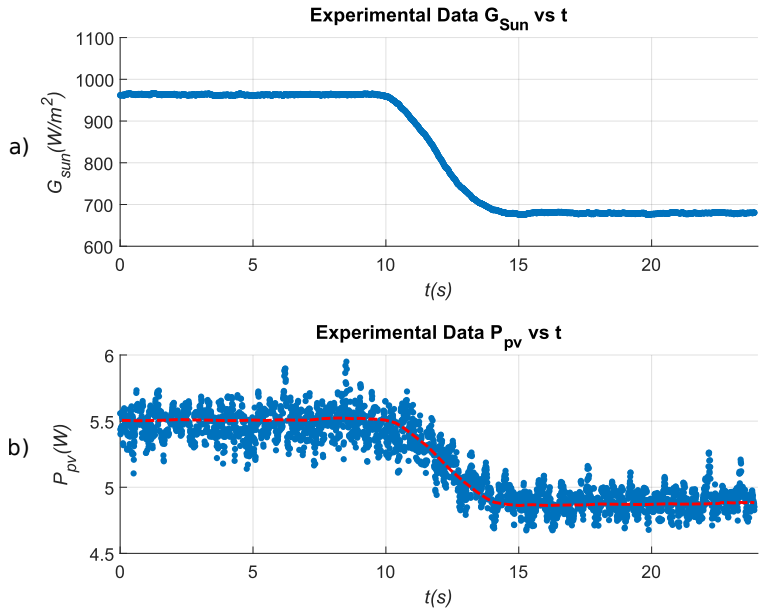

Figure 4.12: Experimental data of *b)* PV cell output power response P_{pv} and power target (red dashed line), to a given *a)* input irradiance step fluctuation $E_e \approx 960\ \frac{W}{m^2}$ for the time interval $(0, 10)\ s$ and $E_e \approx 670\ \frac{W}{m^2}$ for the time interval $(15, 25)\ s$, at a fixed load of $R_L = 10\ \Omega$ with the IDA-PBC strategy implemented in a physical prototype.

4.12 and 4.13 are consistent with the MPP estimated on the P_{pv} experimental functions of Fig. 4.10.

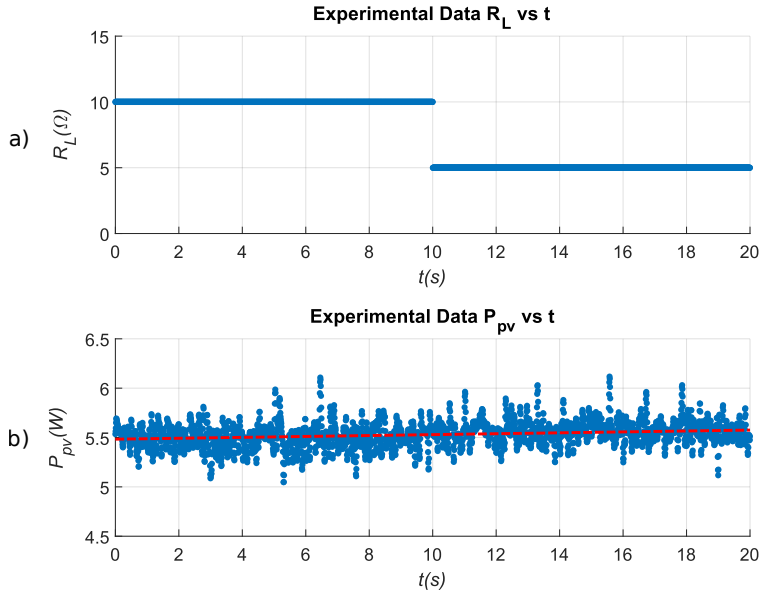

Figure 4.13: Experimental data of *b)* PV cell output power response P_{pv} and power target (red dashed line), to a given *a)* output load R_L step fluctuation from 10 Ω to 5 Ω at $t = 10$ s, at constant sun irradiance $E_e \approx 970\ \frac{W}{m^2}$, with the IDA-PBC strategy implemented in a physical prototype.

Remark 1. *The proposed IDA-PBC strategy is a non-invasive approach since it performs without electrical current sensors, requiring to monitor of only the PV cell output voltage v_p and the irradiance power E_e as input parameters; contrary to the SMC law in* (H.6)*, and the IDA-PBC law of [41], that require electrical current monitoring at the output of the PV cell.*

4.5 Concluding Remarks and Future Work

We have proposed a novel control law for the local MPPT issue, modeled in an energy-based approach, which takes advantage of the structure preservation properties of the system under study. The simplicity of the calculations allows an adequate response under uncertainties in irradiance inputs and output load disturbances. We have also simulated an SMC control law strategy for comparison purposes. Our novel control law and the SMC were simulated under the same conditions, and we demonstrated that both strategies reached the addressed MPPT issue. However, our IDA-PBC approach requires no direct electrical current measurements in an eventual physical implementation, being less invasive and requiring fewer monitoring sensors than the SMC strategy.

Although our control strategy was tested for a single PV cell's MPPT, the proposed solution can be extended to larger applications without critical partial shadow. Since the irradiance was established as a sensing state for control performance, then a single irradiance

sensor is suitable to govern the control of several separated DC-DC converters, each one connected to single PV cell stages, as long as all the PV cell stages remain exposed to the same irradiance level or localized under the same shadowing conditions, i.e., several PV cell arrays could be controlled with a single sensor. Furthermore, since the sensor is externally connected, its installation does not depend on a specific place and requires a single sensor requires a single connection line. Such installation simplicity benefits the implementation in terms of costs, e.g., wiring over the array, in applications such as low-power production PV farms and roof PV cell arrays.

The proposed IDA-PBC strategy was implemented in a physical prototype governed by a control hardware platform Arduino UNO Rev3, reaching a maximum control switching rate of 122Hz. According to simulation results, our control strategy requires fewer computational resources than the SMC strategy due to the simplicity of the proposed algorithm's calculation. Such an advantage results in a low-cost implementation and a reduction in dynamic-power consumption.

Further, the PV cell is physically characterized to obtain an accurate MPP trajectory at several solar irradiance inputs. We evaluate the performance of our IDA-PBC strategy implemented into the physical prototype by inducing step disturbances in the dynamics of the system: firstly, in the solar irradiance displayed over the PV cell; secondly, in the impedance output load of the DC-DC boost converter. As a result, our algorithm shows an efficient performance under input irradiance and output load disturbances.

Implementing our control law requires identifying the PV cell's parameters. Those parameters can be collected mainly from the PV cell manufacturer's datasheet once the PV array is homogeneous in terms of the PV cell's characteristic performance.

Future work will consider re-designing the proposed control law for a higher power system and a physical implementation under reactive output loads conditions.

We have proposed a nonlinear switched-controlled system of a PV cell stage interconnected to a DC-DC boost converter that solves the MPPT issue for a low power load. Now, we introduce in the next Chapter a more complex double-switched proposed control that solves the MPPT issue and the output voltage regulation to feed a battery load from a PV cell interconnected by a DC-DC own-designed buck-boost converter. Moreover, the proposal is implemented and compared to a commercial device to demonstrate its reliability in terms of power consumption.

Chapter 5

Passivity-Based Control Approach for Photovoltaic MPPT and Output Voltage Regulation

This Chapter presents the reliability comparison between a proposed prototype and a commercial device to control both the MPPT of a PV cell and the VR of a DC-DC Converter, interconnected to charge a battery load under natural irradiance conditions. Based on the PH framework, We have modeled a PV cell system that feeds a battery load across a double-switched non-inverted DC-DC buck-boost own converter configuration. Further, a prototype of the system was implemented and calibrated. Moreover, an MPPT and a VR control stages were designed with an IDA-PBC novel nonlinear algorithm to govern the suggested system. Both the linear and nonlinear characteristics of the system are considered in the proposed algorithms, which provide a simple mathematical expression to develop the control strategies, resulting in fast response times from the controller and low computational resource consumption. The suggested control strategy also includes temperature dependencies of the internal PV cell parameters. The proposed prototype and a commercial solar charger were evaluated under natural critical low-level sun irradiance conditions to compare the effectiveness and reliability performance of the systems. We demonstrated that the proposed prototype demands less energy than the commercial solar charger control, which collapses at low irradiation power levels.

5.1 Mathematical Modeling of the DC-DC Conversion and Output VR system

The diagram of the proposed configuration of the energy harvest system: PV cell, DC-DC buck-boost converter, battery, and nonlinear control module, is shown in Fig. 5.1.

We split the system into several stages for analysis and modeling purposes, as follows in the next subsections.

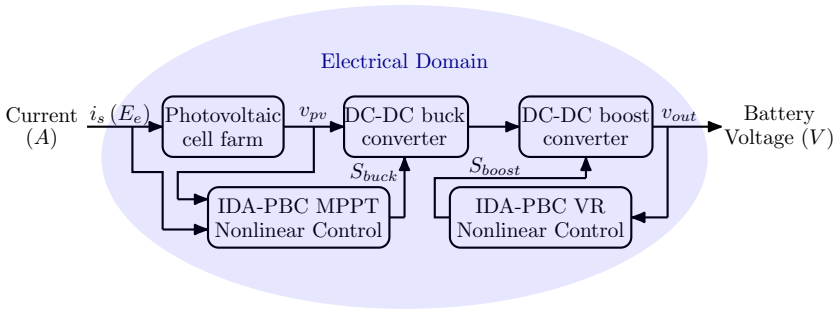

Figure 5.1: Energy storage and control system's block-diagram and related physical-domains.

5.1.1 PH modeling of the PV Cell stage

Fig. 5.2 shows the PV cell stage, where the KVL over the close path I holds

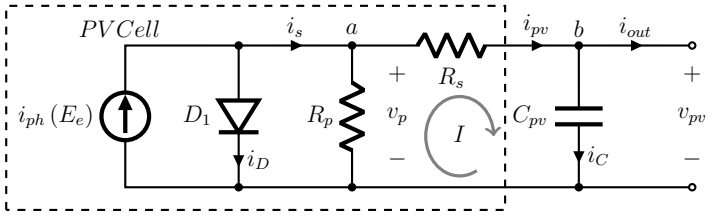

Figure 5.2: Electric diagram of the PV cell with DC-link output capacitor C_{pv}.

$$\begin{aligned} v_{pv} &= v_p - i_{pv}R_s \\ &= \left(i_s\left(E_e\right) - i_{pv}\right)R_p - i_{pv}R_s \\ &= R_p i_s\left(E_e\right) - i_{pv}\left(R_p + R_s\right), \end{aligned} \tag{5.1}$$

re-writing (5.1) in terms of i_{pv}

$$i_{pv} = \frac{R_p}{R_{p,s}} i_s\left(E_e\right) - \frac{1}{R_{p,s}} v_{pv}, \tag{5.2}$$

with $R_{p,s} = R_p + R_s$. Then, the KCL analysis is applied over the node b, and solving for (5.2) it follows

$$\begin{aligned} i_C &= i_{pv} - i_{out} \\ C_{pv}\dot{v}_{pv} &= \frac{R_p}{R_{p,s}} i_s\left(E_e\right) - \frac{1}{R_{p,s}} v_{pv} - S_{buck} i_{bc}, \end{aligned} \tag{5.3}$$

where $S_{buck} = \{0, 1\}$, being $\{0, 1\}$ the $\{open, close\}$ states of the switch. Hence, i_{bc} from Fig. 5.3 depends of the state of S_{buck}. Further, we defined the state variable in terms of charge $q_{pv} = C_{pv} v_{pv}$, to rewrite (5.3)

$$\dot{q}_{pv} = -\frac{1}{R_{p,s}} \frac{q_{pv}}{C_{pv}} + \frac{R_p}{R_{p,s}} i_s\left(E_e\right) - S_{buck} i_{bc}. \tag{5.4}$$

We define a second state dynamics expression in terms of the electrical flux, i.e. ϕ_{pv}, given by

$$\dot{\phi}_{pv} = \frac{q_{pv}}{C_{pv}}. \tag{5.5}$$

Moreover, the PV cell stage's Hamiltonian function $H\left(q_{pv}, \phi_{pv}\right)$ is expressed

$$H\left(q_{pv}, \phi_{pv}\right) = \frac{1}{2C_{pv}} q_{pv}^2, \tag{5.6}$$

and its partial-derivatives in terms of the state variables q_p and ϕ_p are given by

$$\nabla_{q_{pv}} H\left(q_{pv}, \phi_{pv}\right) = \frac{q_{pv}}{C_{pv}}, \quad \nabla_{\phi_{pv}} H\left(q_{pv}, \phi_{pv}\right) = 0. \tag{5.7}$$

Hence, (5.4) and (5.5) are redefined as

$$\dot{q}_{pv} = -\frac{1}{R_{p,s}} \nabla_{q_{pv}} H + k \nabla_{\phi_{pv}} H + \frac{R_p}{R_{p,s}} i_s\left(E_e\right) - S_{buck} i_{bc} \tag{5.8}$$

$$\dot{\phi}_{pv} = \nabla_{q_{pv}} H, \tag{5.9}$$

where the constant k is chosen equal to -1 to keep the desired structure of the PV cell stage's PH system Σ_{pv}, formulated from (5.8), (5.9) and (5.6) as follow

$$\Sigma_{pv} \begin{cases} \underbrace{\begin{bmatrix} \dot{q}_{pv} \\ \dot{\phi}_{pv} \end{bmatrix}}_{\dot{x}_{pv}} = \underbrace{\begin{bmatrix} \frac{-1}{R_{p,s}} & -1 \\ 1 & 0 \end{bmatrix}}_{\mathcal{J}(x_{pv}) - \mathcal{R}(x_{pv})} \underbrace{\begin{bmatrix} \nabla_{q_{pv}} H\left(q_{pv}, \phi_{pv}\right) \\ \nabla_{\phi_{pv}} H\left(q_{pv}, \phi_{pv}\right) \end{bmatrix}}_{\nabla_{x_{pv}} H(x_{pv})} \\ \qquad\qquad + \underbrace{\begin{bmatrix} \frac{R_p}{R_{p,s}} \\ 0 \end{bmatrix}}_{g(x_{pv})} i_s\left(E_e\right) + \begin{bmatrix} -S_{buck} \\ 0 \end{bmatrix} i_{bc}, \\ y_{pv} = g^{\top}\left(x_{pv}\right) \nabla_{x_{pv}} H\left(x_{pv}\right) = v_p, \end{cases} \tag{5.10}$$

with an input-output port-pair $\left(u_{pv}, y_{pv}\right) = \left(i_s\left(E_e\right), v_p\right)$, where the matrix $\mathcal{R}\left(x_{pv}\right) = \operatorname{diag}\left(\frac{1}{R_{p,s}}, 0\right)$ and $\mathcal{J}\left(x_{pv}\right)$ complies the skew-symmetric condition, since

$$\mathcal{J}\left(x_{pv}\right) = \begin{bmatrix} 0 & -1 \\ 1 & 0 \end{bmatrix}. \tag{5.11}$$

Based on the dynamics of the PH system Σ_{pv} in (5.10), the Hamiltonian function (5.6), and since $R_{p,s} \geq 0$, the power balance in (2.13) is fully satisfied.

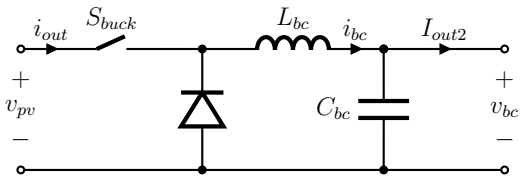

Figure 5.3: Electric diagram of the DC-DC buck converter governed by a normally open (NO) switch S_{buck}.

5.1.2 PH Modeling of the DC-DC Buck converter Stage

A diagram of the DC-DC buck converter is shown in Fig. 5.3, where the input voltage is v_{pv}, supplied across a DC-link capacitor C_{pv} of Fig. 2.1, and i_{pv} is the input current. The output voltage and current to the output stage are represented by v_{bc}, I_{out2}.

By solving KVL and KCL on the DC-DC buck converter circuit diagram of Fig. 5.3, it follows that

$$C_{bc}\dot{v}_{bc} = i_{bc} - i_{out2}, \tag{5.12}$$

$$L_{bc}\dot{i}_{bc} = -v_{bc} + S_{buck}v_{pv}, \tag{5.13}$$

being $i_{out2} = i_{bc2}$ in line with Fig. 5.3 and 5.4. Once again, the dynamics in (5.12) and (5.13) are rewritten in terms of the state variables of charge $q_{bc} = C_{bc}v_{bc}$ and flux $\phi_{bc} = L_{bc}i_{bc}$, as

$$\dot{q}_{bc} = \frac{\phi_{bc}}{L_{bc}} - i_{bc2}, \tag{5.14}$$

$$\dot{\phi}_{bc} = -\frac{q_{bc}}{C_{bc}} + S_{buck}v_{pv}. \tag{5.15}$$

The DC-DC boost converter Hamiltonian function $H\left(q_{bc}, \phi_{bc}\right)$ complies

$$H\left(q_{bc}, \phi_{bc}\right) = \frac{1}{2C_{bc}}q_{bc}^2 + \frac{1}{2L_{bc}}\phi_{bc}^2, \tag{5.16}$$

and its partial-derivatives in terms of the state variables q_{pv} and ϕ_{pv} are given by

$$\nabla_{q_{bc}} H\left(q_{bc}, \phi_{bc}\right) = \frac{q_{bc}}{C_{bc}}, \tag{5.17}$$

$$\nabla_{\phi_{bc}} H\left(q_{bc}, \phi_{bc}\right) = \frac{\phi_{bc}}{L_{bc}}. \tag{5.18}$$

Then, we rewrite the dynamics in (5.14) and (5.15) as

$$\dot{q}_{bc} = \nabla_{\phi_{bc}} H - i_{bc2}, \tag{5.19}$$

$$\dot{\phi}_{bc} = -\nabla_{q_{bc}} H + S_{buck}v_{pv}, \tag{5.20}$$

and we formulate the PH system Σ_{bc} of the DC-DC buck converter from (5.19), (5.20) and (5.16) as

$$\Sigma_{bc}\begin{cases}\underbrace{\begin{bmatrix}\dot{q}_{bc}\\ \dot{\phi}_{bc}\end{bmatrix}}_{\dot{x}_{bc}} = \underbrace{\begin{bmatrix}0 & 1\\ -1 & 0\end{bmatrix}}_{\mathcal{J}(x_{bc})-\mathcal{R}(x_{bc})}\underbrace{\begin{bmatrix}\nabla_{q_{bc}}H\left(q_{bc},\phi_{bc}\right)\\ \nabla_{\phi_{bc}}H\left(q_{bc},\phi_{bc}\right)\end{bmatrix}}_{\nabla_{x_{bc}}H(x_{bc})}\\ \qquad\qquad + \underbrace{\begin{bmatrix}0\\ S_{buck}\end{bmatrix}}_{g(x_{bc})}v_{pv} + \begin{bmatrix}-1\\ 0\end{bmatrix}i_{bc2}\\ y_{bc} = g^{\top}\left(x_{bc}\right)\nabla_{x_{bc}}H\left(x_{bc}\right) = S_{buck}i_{bc}.\end{cases} \tag{5.21}$$

where input-output port-pair (u_{bc}, y_{bc}) of the system Σ_{bc} are given by $(v_{pv}, S_{buck}i_{bc})$. Moreover, $\mathcal{J}\left(x_{bc}\right)$ complies the skew-symmetric matrix condition, i.e.,

$$\mathcal{J}\left(x_{bc}\right) = \begin{bmatrix}0 & 1\\ -1 & 0\end{bmatrix}, \tag{5.22}$$

and $\mathcal{R}\left(x_{bc}\right) = 0$, then the power balance in (2.13) is complied.

5.1.3 PH Modeling of the DC-DC Boost Converter stage

The basic design of the DC-DC boost converter electrical diagram is depicted in Fig. 5.4 where the input voltage and current are represented by v_{bc}, i_{bc2}, and v_{bc2}, i_{out3} are the output voltage and current of the converter.

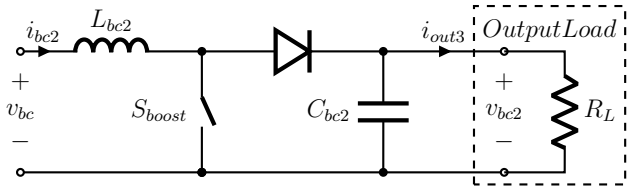

Figure 5.4: Electric diagram of the DC-DC boost converter governed by a normally closed (NC) switch S_{boost}.

Correspondingly to the DC-DC buck converted, solving the KVL and KCL on the diagram of Fig. 5.4 follows

$$C_{bc2}\dot{v}_{bc2} = S_{boost}i_{bc2} - \frac{v_{bc2}}{R_L}, \tag{5.23}$$

$$L_{bc2}\dot{i}_{bc2} = -S_{boost}v_{bc2} + v_{bc}. \tag{5.24}$$

where $S_{boost} = \{0, 1\}$ are defined as the $\{close, open\}$ switch states of the circuit. As well, (5.23) and (5.24) are expressed in terms of the state variables of charge $q_{bc2} = C_{bc2}v_{bc2}$ and flux $\phi_{bc2} = L_{bc2}i_{bc2}$, that yields

$$\dot{q}_{bc2} = -\frac{q_{bc2}}{R_L C_{bc2}} + S_{boost}\frac{\phi_{bc2}}{L_{bc2}}, \tag{5.25}$$

$$\dot{\phi}_{bc2} = -S_{boost}\frac{q_{bc2}}{C_{bc2}} + v_{bc}, \tag{5.26}$$

whose Hamiltonian function $H\left(q_{bc}, \phi_{bc}\right)$ is given by

$$H\left(q_{bc2}, \phi_{bc2}\right) = \frac{1}{2C_{bc2}}q_{bc2}^2 + \frac{1}{2L_{bc2}}\phi_{bc2}^2, \tag{5.27}$$

and its partial-derivatives in terms of the state variables q_{pv} and ϕ_{pv} comply

$$\nabla_{q_{bc2}} H\left(q_{bc2}, \phi_{bc2}\right) = \frac{q_{bc2}}{C_{bc2}}, \tag{5.28}$$

$$\nabla_{\phi_{bc2}} H\left(q_{bc2}, \phi_{bc2}\right) = \frac{\phi_{bc2}}{L_{bc2}}. \tag{5.29}$$

We can rewrite the dynamics in (5.25) and (5.26) as

$$\dot{q}_{bc2} = -\frac{1}{R_L}\nabla_{q_{bc2}} H + S_{boost}\nabla_{\phi_{bc2}} H, \tag{5.30}$$

$$\dot{\phi}_{bc2} = -S_{boost}\nabla_{q_{bc2}} H + v_{bc}, \tag{5.31}$$

achieving a DC-DC boost converter PH system Σ_{bc2} of the form

$$\Sigma_{bc2}\begin{cases} \underbrace{\begin{bmatrix} \dot{q}_{bc2} \\ \dot{\phi}_{bc2} \end{bmatrix}}_{\dot{x}_{bc2}} = \underbrace{\begin{bmatrix} \frac{-1}{R_L} & S_{boost} \\ -S_{boost} & 0 \end{bmatrix}}_{\mathcal{J}(x_{bc2})-\mathcal{R}(x_{bc2})} \underbrace{\begin{bmatrix} \nabla_{q_{bc2}} H\left(q_{bc2}, \phi_{bc2}\right) \\ \nabla_{\phi_{bc2}} H\left(q_{bc2}, \phi_{bc2}\right) \end{bmatrix}}_{\nabla_{x_{bc2}} H(x_{bc2})} \\ \qquad\qquad + \underbrace{\begin{bmatrix} 0 \\ 1 \end{bmatrix}}_{g(x_{bc2})} v_{bc}, \\ y_{c2} = g^\top \nabla_{x_{bc2}} H\left(x_{bc2}\right) = i_{bc2}. \end{cases} \tag{5.32}$$

In Σ_{bc2} the input-output pair is given by $(u_{bc2}, y_{bc2}) = (v_{bc2}, i_{bc2})$, while $\mathcal{R}\left(x_{bc2}\right) = \text{diag}\left(\frac{1}{R_L}, 0\right)$ and $\mathcal{J}\left(x_{bc2}\right)$ is a skew-symmetric matrix of the form

$$\mathcal{J}\left(x_{bc2}\right) = \begin{bmatrix} 0 & S_{boost} \\ -S_{boost} & 0 \end{bmatrix}, \tag{5.33}$$

such that the system Σ_{bc2} complies the power balance in (2.13). The complete integration of the stages can be expressed as PH systems since all single stages of the proposed energy-harvest system do. We suggest a PH-based control algorithm to solve the issues of the MPPT and VR.

5.2 IDA-PBC Strategy Approach

We design two independent control algorithms for both MPPT and output VR issues based on the IDA-PBC Strategy. Firstly, an algorithm integrating together the PV cell and the DC-DC buck converter stages from Fig. 5.2 and 5.3 is proposed to solve the MPPT problem by controlling the timing of the $\{close, open\}$ states of the DC-DC buck converter switch S_{buck}. Next in order, we consider the control over the isolated DC-DC boost converter stage feeding resistive load R_L as in Fig. 5.4, where the $\{open, close\}$ timing of the switch S_{boost} performs the VR control task.

5.2.1 MPPT IDA-PBC design

Recapitulating from the PH systems Σ_{pv} (5.10) and Σ_{bc} (5.21), we interconnect the PV Cell and the DC-DC buck converter stages in a more general PH system Σ_1 as follow

$$\Sigma_1 \begin{cases} \underbrace{\begin{bmatrix} \dot{q}_{pv} \\ \dot{\phi}_{pv} \\ \dot{q}_{bc} \\ \dot{\phi}_{bc} \end{bmatrix}}_{\dot{x}_1} = \underbrace{\begin{bmatrix} \frac{-1}{R_{p,s}} & -1 & 0 & -S_{buck} \\ 1 & 0 & 0 & 0 \\ 0 & 0 & 0 & 1 \\ S_{buck} & 0 & -1 & 0 \end{bmatrix}}_{\mathcal{J}(x_1)-\mathcal{R}(x_1)} \underbrace{\begin{bmatrix} \nabla_{q_{pv}} H_1 \\ \nabla_{\phi_{pv}} H_1 \\ \nabla_{q_{bc}} H_1 \\ \nabla_{\phi_{bc}} H_1 \end{bmatrix}}_{\nabla_{x_1} H_1} \\ \qquad + \underbrace{\begin{bmatrix} \frac{R_p}{R_{p,s}} \\ 0 \\ 0 \\ 0 \end{bmatrix}}_{g(x_1)} i_s(E_e) + \begin{bmatrix} 0 \\ 0 \\ -1 \\ 0 \end{bmatrix} i_{bc2}, \\ y_1 = g^\top(x_1) \nabla_{x_1} H_1 = v_p, \end{cases} \tag{5.34}$$

where the full integration of the Hamiltonian functions in (5.6) and (5.16) remains

$$H_1(q_{pv}, \phi_{pv}, q_{bc}, \phi_{bc}) = \frac{1}{2C_{pv}} q_{pv}^2 + \frac{1}{2C_{bc}} q_{bc}^2 + \frac{1}{2L_{bc}} \phi_{bc}^2, \tag{5.35}$$

and the input-output port-pair is defined by $(i_s(E_e), v_p)$. Since Σ_{pv} and Σ_{bc} comply the power balance in (2.13), as well Σ_1 do. Attending to the IDA-PBC design procedure of section 2.6, we start our algorithm configuration to solve the MPPT issue by assigning S_{buck} as the control law term $\beta(x_1)$ of the system (5.34) becoming a dependant function on the state variables of the system Σ_1. Hence, to comply the statement *Structure Preservation* (i) of subsection 2.6, we assume the matrices $\mathcal{J}_a(x_1)$ and $\mathcal{R}_a(x_1)$ are equal to zero, simplifying in (2.16), such that

$$\mathcal{K}(x_1) = [\mathcal{J}(x_1, \beta(x_1)) - \mathcal{R}(x_1)]^{-1} g(x_1, \beta(x_1)), \tag{5.36}$$

$$\mathcal{K}(x_1) = \begin{bmatrix} \frac{-1}{R_{p,s}} & -1 & 0 & -\beta(x_1) \\ 1 & 0 & 0 & 0 \\ 0 & 0 & 0 & 1 \\ \beta(x_1) & 0 & -1 & 0 \end{bmatrix}^{-1} \begin{bmatrix} \frac{R_p i_s(E_e)}{R_{p,s}} \\ 0 \\ -i_{bc2} \\ 0 \end{bmatrix}, \tag{5.37}$$

and solving for $\mathcal{K}$

$$\mathcal{K}(x_1) = \begin{bmatrix} \mathcal{K}_1(x_1) \\ \mathcal{K}_2(x_1) \\ \mathcal{K}_3(x_1) \\ \mathcal{K}_4(x_1) \end{bmatrix} = \begin{bmatrix} 0 \\ \frac{-R_p}{R_{p,s}} i_s(E_e) + \beta(x_1) i_{out} \\ 0 \\ -i_{out} \end{bmatrix}. \tag{5.38}$$

Since $\beta(x_1)$ is still an unknown function, the statement (ii) of *Integrability* is refered as follow

$$\nabla_{x_1} \mathcal{K}(x_1) = \nabla_{x_1} \mathcal{K}(x_1)^\top, \tag{5.39}$$

then, from (5.38)

$$\nabla_{q_{pv}} \mathcal{K}_2(x_1) = \nabla_{q_{bc}} \mathcal{K}_2(x_1) = \nabla_{\phi_{bc}} \mathcal{K}_2(x_1) = 0. \tag{5.40}$$

The expression $\nabla_{q_{pv}} \mathcal{K}_2(x_1) = 0$ is selected as a candidate to solve $\beta(x_1)$, since the voltage v_{pv} is a suitable state variable to sense, in order to implement a current sensor-less strategy for the MPPT, as in [34]. Thus, from (2.1) and (2.2) we rearrange $\beta(x_1)$ in terms of q_{pv} as

$$\nabla_{q_{pv}} \left(\frac{-R_p}{R_{p,s}} i_s(E_e) + \beta_1(q_{pv}) i_{bc2} \right) = 0, \tag{5.41}$$

solving $\beta(x_1)$ as

$$\beta(q_{pv}) = \frac{-i_0}{i_{out}} \left(\frac{R_p}{R_{p,s}} \right) \exp\left(\frac{q_{pv}}{C_{pv}\alpha} \right), \tag{5.42}$$

and (5.38) becomes

$$\mathcal{K}(q_{pv}) = \begin{bmatrix} 0 \\ \frac{-R_p}{R_{p,s}} \left(i_s + i_0 \exp\left(\frac{q_{pv}}{C_{pv}\alpha} \right) \right) \\ 0 \\ -i_{bc2} \end{bmatrix}. \tag{5.43}$$

The state variable dependency in (5.43) suggests a (locally) equilibrium spot q_{pv}^* as a particular case to be determined from the statement *Equilibrium Assignment* (iii). Then,

$$\frac{-R_p}{R_{p,s}} \left(i_s(E_e) + i_0 \exp\left(\frac{q_{pv}^*}{C_{pv}\alpha} \right) \right) = 0, \tag{5.44}$$

where $v_{pv}^* = \frac{q_{pv}^*}{C_{pv}}$, and we solve

$$v_{pv}^* = nV_t \ln\left(\frac{-i_s\left(E_e\right)}{i_0}\right). \tag{5.45}$$

From (2.1) and (2.2), we expand (5.45) as

$$v_{pv}^* = \alpha \ln\left(\exp\left(\frac{v_p}{\alpha}\right) - 1 - \frac{\left(I_{SC,nom} + K_0\Delta T\right)}{i_0}\frac{E_e}{E_{nom}}\right), \tag{5.46}$$

where $v_p = R_s I_{pv} + v_{pv}^*$. To guarantee the system reaches the equilibrium on the MPP trajectory of the PV cell, the specific value of v_{pv}^* is estimated from the transfer function of i_{pv} vs v_{pv}. Therefore, the reliance between v_{pv} and the MPP trajectory is determined from the output power term $P_{pv}\left(v_{pv}\right)$ as in [34], such that

$$\nabla_{v_{pv}} P_{pv}\left(v_{pv}^*\right) = \nabla_{v_{pv}}\left(i_{pv} v_{pv}\right)\big|_{v_{pv}^*} = 0, \tag{5.47}$$

solving from (2.1) and (2.2)

$$\nabla_{v_{pv}}\left(\left(i_{ph}\left(E_e\right) - i_0\left(\exp\left(\frac{v_p}{\alpha}\right) - 1\right) - \frac{v_p}{R_p}\right) v_{pv}\right)\Big|_{v_{pv}^*} = 0. \tag{5.48}$$

where the magnitude of R_s is very low compared to R_p accordint to Table 5.2 (e.g.,. $R_s < 0.001R_p$), and we assume $R_s I_{pv} \to 0 \Rightarrow v_p \to v_{pv}^*$; thus, (5.48) becomes

$$i_{ph}\left(E_e\right) + i_0 - \frac{2}{R_p} v_{pv}^* - i_0 \exp\left(\frac{v_{pv}^*}{\alpha}\right)\left(1 + \frac{v_{pv}^*}{\alpha}\right) \approx 0. \tag{5.49}$$

In (5.49), v_{pv}^* can be solved in terms of the irradiance E_e in (2.1) by numerical methods, i.e. the so-called *equilibrium trajectory*. It can be demonstrated that all solutions of v_{pv}^* in (5.49) achieve the MPP trajectory and, consequently, the statement *Equilibrium Assignment* in (5.45) is complied by the values of v_{pv}^* on the *equilibrium trajectory*.

Since the control strategy proposed for the scalar function $\beta\left(v_{pv}\right)$ has been developed based on requirements derived from a closed-loop arbitrary structure, i.e. the system in (2.16), we can confirm the compliance of the *Lyapunov Stability* statement in (2.22) of section 2.6. It follows that based on $\mathcal{K}\left(q_{pv}\right)$ in (5.43) and $H_1\left(q_{pv}, \phi_{pv}, q_{bc}, \phi_{bc}\right)$ in (5.35) we can establish

$$\nabla_{x_1}\mathcal{K}\left(x_1^*\right) > -\nabla_{x_{p1}}^2 H\left(x_1^*\right). \tag{5.50}$$

$$\frac{-R_p}{R_{p,s}}\nabla_{\phi_{pv}}\left(i_s\left(E_e\right) + i_0\exp\left(\frac{q_{pv}}{C_{pv}\alpha}\right)\right)\Big|_{x_1^*} > -\left(\nabla_{q_{pv}}\frac{q_{pv}}{C_{pv}} + \nabla_{q_{bc}}\frac{q_{bc}}{C_{bc}} + \nabla_{\phi_{bc}}\frac{\phi_{bc}}{L_{bc}}\right)\Big|_{x_1^*}. \tag{5.51}$$

Further, recovering i_s from (2.1) and (2.2)

$$\frac{R_p}{R_{p,s}}\nabla_{\phi_{pv}}\left(i_{ph}\left(E_e\right) - i_D + i_0\exp\left(\frac{q_{pv}}{C_{pv}\alpha}\right)\right) > -\left(\nabla_{q_{pv}}\frac{q_{pv}}{C_{pv}} + \nabla_{q_{bc}}\frac{q_{bc}}{C_{bc}} + \nabla_{\phi_{bc}}\frac{\phi_{bc}}{L_{bc}}\right), \tag{5.52}$$

and solving

$$0 > -\left(\frac{1}{C_{pv}} + \frac{1}{C_{bc}} + \frac{1}{L_{bc}}\right). \tag{5.53}$$

Thus, (5.53) holds since $\{C_{pv}, C_{bc}, L_{bc}\} \in \mathbb{R}^+$ and then *Lyapunov Stability* statement is satisfied.

5.2.2 VR IDA-PBC design

In this case, S_{boost} from (5.32) was assigned as the control law $\beta(x_{bc2})$ of the VR IDA-PBC algorithm design, becoming a function dependant on the state variables of the system Σ_{bc2}. To satisfy the *Structure Preservation* statement, the matrices $J_a(x_{bc2})$ and $R_a(x_{bc2})$ from (2.16) are assumed equal to zero, simplifying (2.16) to

$$\mathcal{K}(x_{bc2}) = \left[\mathcal{J}(x_{bc2}, \beta(x_{bc2})) - \mathcal{R}(x_{bc2})\right]^{-1} g(x_{bc2}, \beta(x_{bc2})), \tag{5.54}$$

and then $\mathcal{K}(x_{bc2})$ is solved as

$$\mathcal{K}(x_{bc2}) = \begin{bmatrix} \mathcal{K}_1(x_{bc2}) \\ \mathcal{K}_2(x_{bc2}) \end{bmatrix} = \begin{bmatrix} \dfrac{-v_{bc}}{\beta(x_{bc2})} \\ \dfrac{-v_{bc}}{R_L \beta(x_{bc2})^2} \end{bmatrix}, \tag{5.55}$$

shifting *Integrability* statement into

$$\nabla_{q_{bc2}} \mathcal{K}_2(x_{bc2}) = \nabla_{\phi_{bc2}} \mathcal{K}_1(x_{bc2}), \tag{5.56}$$

$$\nabla_{q_{bc2}} \left(\frac{-v_{bc}}{R_L \beta(x_{bc2})^2} \right) = \nabla_{\phi_{bc2}} \left(\frac{-v_{bc}}{\beta(x_{bc2})} \right). \tag{5.57}$$

The PDE in (5.57) is solved and the resulting control function $\beta(x_{bc2})$ is explicitly described in terms of q_{bc2} and ϕ_{bc2} as

$$\beta(x_{bc2}) = \frac{2}{R_L} \frac{\phi_{bc2}}{(\mathcal{C} - q_{bc2})}, \tag{5.58}$$

with $\mathcal{C}$ an unknown constant to be defined later. Hence, $\mathcal{K}(x_{bc2})$ in (5.55) becomes

$$\mathcal{K}(x_{bc2}) = \begin{bmatrix} \dfrac{-R_L(\mathcal{C} - q_{bc2}) v_{bc}}{2\phi_{bc2}} \\ \dfrac{-R_L(\mathcal{C} - q_{bc2})^2 v_{bc}}{4\phi_{bc2}^2} \end{bmatrix}. \tag{5.59}$$

The constant $\mathcal{C}$ is defined by accomplishing the *Equilibrium Assignment* statement, where the magnitude of the state variables in the equilibrium target is described by $x^* = (q^*_{bc2}, \phi^*_{bc2})$

$$\begin{bmatrix} \dfrac{R_L(\mathcal{C} - q^*_{bc2}) v_{bc}}{2\phi^*_{bc2}} \\ \dfrac{R_L(\mathcal{C} - q^*_{bc2})^2 v_{bc}}{4{\phi^*_{bc2}}^2} \end{bmatrix} = \begin{bmatrix} \dfrac{q^*_{bc2}}{C_{bc2}} \\ \dfrac{\phi^*_{bc2}}{L_{bc2}} \end{bmatrix}, \tag{5.60}$$

and solving for $\mathcal{C}$

$$\begin{bmatrix} \mathcal{C}_1 \\ \mathcal{C}_2 \end{bmatrix} = \begin{bmatrix} q^*_{bc2} \left(\dfrac{2\phi^*_{bc2}}{R_L C_{bc2} v_{bc}} + 1 \right) \\ 2\phi^*_{bc2} \left(\dfrac{\phi^*_{bc2}}{R_L L_{bc2} v_{bc}} \right)^{\frac{1}{2}} + q^*_{bc2} \end{bmatrix}. \tag{5.61}$$

Being $\{\mathcal{C}_1, \mathcal{C}_2\}$ in (5.61) represent the possible solutions for $\mathcal{C}$, both of then suitable in (5.59). Moreover, the control function $\beta(x_{bc2})$ in (5.58) is finally defined in terms of $\mathcal{C}_1$. Additionally, the equilibrium states q_{bc2}, ϕ_{bc2} can be defined depending on the *voltage, current* demands of the final load.

As well as proposed to $\beta(v_{pv})$, to find the conditions where $\beta(x_{bc2})$ holds the *Lyapunov Stability* statement in (2.22), we formulate from $\mathcal{K}(x_{bc2})$ in (5.59) and $H(q_{bc2}, \phi_{bc2})$ (5.27) that

$$\begin{aligned} &- R_L v_{bc} \left(\nabla_{q_{bc2}} \left(\frac{\gamma_{bc2}}{2\phi_{bc2}} \right) + \nabla_{\phi_{bc2}} \left(\frac{\gamma_{bc2}^2}{4\phi_{bc2}^2} \right) \right) \Big|_{x_{bc2}^*} > \\ &- \left(\nabla_{q_{bc2}} \frac{q_{bc2}}{C_{bc2}} + \nabla_{\phi_{bc2}} \frac{\phi_{bc2}}{L_{bc2}} \right) \Big|_{x_{bc2}^*}, \end{aligned} \tag{5.62}$$

being $\gamma_{bc2} = \mathcal{C}_1 - q_{bc2}$. Furthermore

$$\frac{R_L v_{bc}}{2\phi_{bc2}^*} + \frac{1}{L_{bc2}} > - \left(\frac{1}{C_{bc2}} \right), \tag{5.63}$$

and then, the *Lyapunov Stability* statement complies since $\{L_{bc2}, C_{bc2}, R_L\} \in \mathbb{R}^+$ and $\{v_{bc}, \phi_{bc2}^*\} \geq 0$.

5.3 Switching Control Implementation

We have defined a scalar control function $\beta(q_{pv})$ in (5.42) which solves the PDE in (5.41) to reach the MPPT objective of the close-loop PH system Σ_1 proposed in (5.34). However, since the performance of the switch S_{buck} lies between the states modes $\{0, 1\}$, as in [132, 34], we formulate a switching modification based on [133, 131, 34] surveys, as follow

$$S_{buck} = \begin{cases} 0 & \text{for} \quad \beta\left(q_{pv}^*\right) - \beta\left(q_{pv}\right) > 0 \\ 1 & \text{for} \quad \beta\left(q_{pv}^*\right) - \beta\left(q_{pv}\right) \leq 0, \end{cases} \tag{5.64}$$

Hence, the new suggested switching control law S_{buck} in (5.64), in terms of the previous control function $\beta(q_{pv})$, can be implemented as a current sensor-less control since it depends only on v_{pv} and E_e states.

Similarly, the control function $\beta(q_{bc2}, \phi_{bc2})$ in (5.58) is adapted to achieve a new S_{boost} control function, that relies between switching state modes $\{0, 1\}$ and performs over the proposed close-loop PH system Σ_{bc} in (5.32). Then, it can be defined

$$S_{boost} = \begin{cases} 0 & \text{for} \quad \beta(x_{bc2}^*) - \beta(x_{bc2}) < 0 \\ 1 & \text{for} \quad \beta(x_{bc2}^*) - \beta(x_{bc2}) \geq 0. \end{cases} \tag{5.65}$$

The new control function S_{boost} depends on v_{bc2} or i_{bc2}, in agreement with the relationships $q_{bc2} = C_{bc2} v_{bc2}$ and $\phi_{bc2} = L_{bc2} i_{bc2}$. The selection of the equilibrium state, either the v_{bc2} or i_{bc2}, depends on the load control requirements.

5.4 Testing Prototype Set Up

The experimental prototype designed to verify the performance of the MPPT and VR control algorithms proposed in section 5.3, is shown in Fig. 5.5. The home-made switching control of the DC-DC boost and buck converters is described in Appendices F and G. The setup

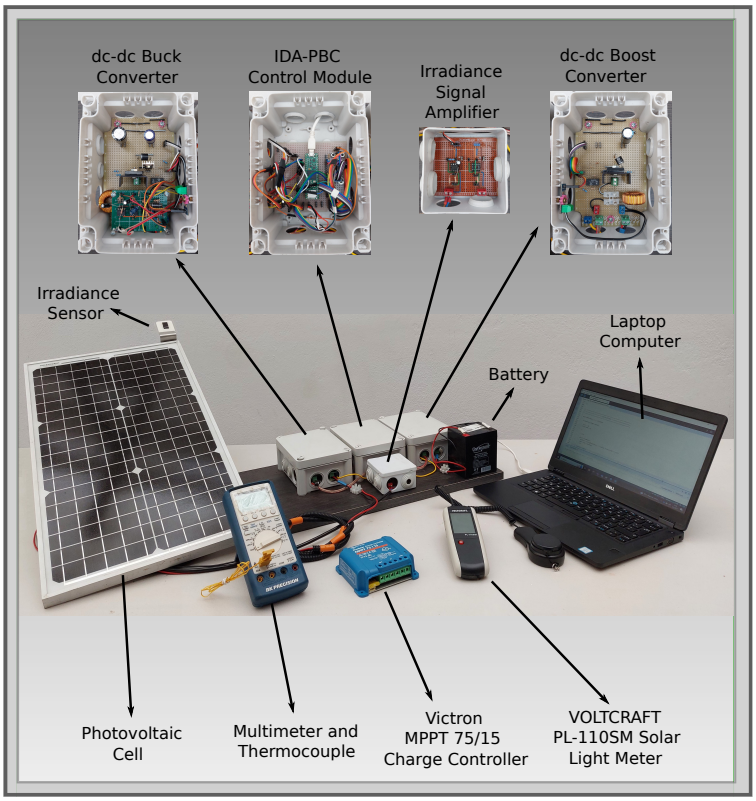

Figure 5.5: Prototype setup for physical experimental measurements of the MPPT and VR system.

hardware, equipment, and tools are described in Table 5.1. A signal conditioner amplifier active filter was included to raise the output voltage signal from the *Spektron* 210 [135] sensor, which reaches only 70 mV at $E_e = 1000\ \frac{W}{m^2}$, Moreover, to calibrate the irradiance sensor *Spektron* 210, we utilize the solar light meter $VOLTCRAFT\ PL-110SM$ [138]. Likewise, the current and voltage sensor calibration was referred to the multimeter *BK PRECISION* 393.

Since the equilibrium state v_{pv}^* in (5.49) and the control function $\beta\left(q_{pv}\right)$ depend on the internal parameters of the PV cell and their dependencies in terms of the temperature T_v, as in (2.1) and (2.2), the suitable Method for the Analytical Extraction of the Single-Diode PV Model Parameters developed by [126] has been called forth to estimate R_p, R_s, i_0 and α, since it makes use of the PV cell data-sheet to determine the required parameters. Furthermore, We formulate the parameters R_p, R_s, i_0 in terms of the temperature fluctuation ΔT, as shown in the Table 5.2.

We validate the computed parameters of the PV cell by simulating the transfer functions i_{pv} *vs* v_{pv} and P_{pv} *vs* v_{pv}, based on (2.1) and (2.2), at several irradiances E_e in steps of 100

Table 5.1: Experimental setup hardware, equipment, and tools

Name	***Model***	***Quantity***
PV cell *CELLEVIA* 30W [137]	$CL-SM30M$	1
Prototyping platform *TEENSY*	4.1	1
Irradiance sensor *SPECTRON* [135]	210	1
Solar light meter *VOLTCRAFT* [138]	$PL-110SM$	1
Hall current sensor 5A	$ACS712$	1
Multimeter *BK PRECISION*[a]	393	1
Laptop *DELL LATITUDE*	5491	1
Solar charger *VICTRON BLUE SOLAR* [139]	*MPPT* 75/15	1
Electronic components	N/A	N/A
Shielded enclosures	N/A	N/A

[a] Thermocouple K included.

Table 5.2: Key parameters of the MPPT and VR control system

Parameter description	***Magnitude***
Temperature T[a]	25 °C
Irradiance E_{nom}[a]	1000 W/m^2
Output Power $P_{pv,nom}$[a]	30.0 W
Short-circuit current $I_{SC,nom}$[a]	1.77 A
Open-circuit voltage $V_{OC,nom}$[a]	22.9 V
Output current $I_{nom}@MPP$[a]	1.62 A
Output voltage $V_{nom}@MPP$[a]	18.6 V
Temperature coefficient of $V_{OC,nom}$[a]	$-(0.40 \pm 0.05)\%$ °C
Temperature coefficient of $I_{SC,nom}$[a]	$(0.065 \pm 0.01)\%$ °C
Temperature coefficient of $P_{pv,nom}$[a]	$(0.5 \pm 0.05)\%$ °C
Constant α[b]	761 mV
Saturation current i_0[b]	$2\mathrm{e}^{(0.1001*\Delta T)}$ μA
PV cell series resistor R_s[b]	$-100\Delta T + 0.0213$ $\mu\Omega$
PV cell shunt resistor R_p[b]	$-1.1301\Delta T + 248.36$ Ω

[a] From CL-SM30M data-sheet

[b] Estimated as in [126]

kW/m^2 between zero to 1000 kW/m^2, at several temperature conditions T_v, i.e., 25 °C, 40 °C and 55 °C, as shown in Fig. 5.6. According to the Temperature coefficient of $P_{pv,nom}$ reported on the data sheet and included in Table 5.2, the simulated transfer function P_{pv} *vs* v_{pv} holds the manufacturer technical data for any tested temperature.

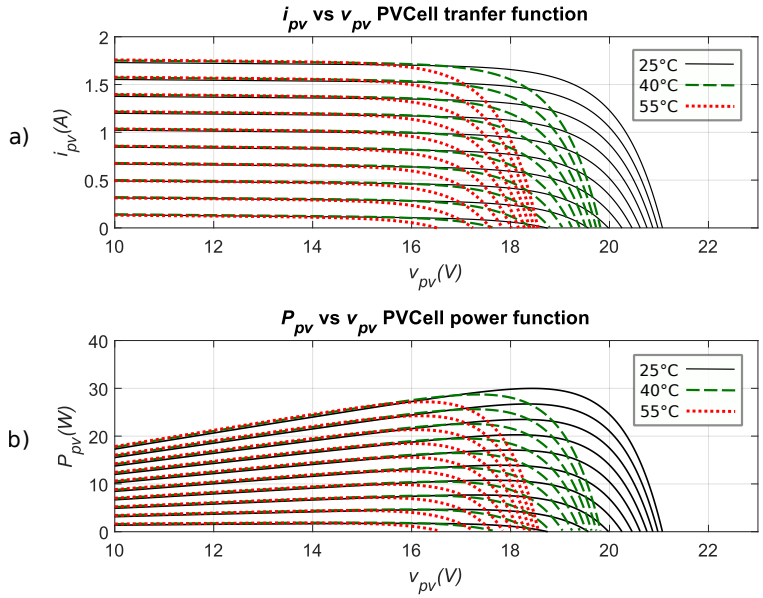

Figure 5.6: Simulation of the PV cell transfer functions: *a)* i_{pv} *vs* v_{pv} and *b)* P_{pv} *vs* v_{pv}, at different temperatures.

The prototype in Fig. 5.5 was compared to the commercial solar charger *Victron Blue Solar MPPT* 75/15 [139], in terms of controlling energy demand and reliability by exposing both systems to solar irradiance disturbances. Both systems (prototype and commercial) are entirely fed from the PV cell source, and then the consumption of the control stages is extracted from the PV cell power. As the available commercial PV cell $CL-SM30M$ [137] has a power specification of 30 W at 1000 W/m^2, we selected a battery that expends around 6 W (430 mA at 14.4 V) in the charging process to operate as the output load R_L, to generate circumstances of power demand and compare the controllers' consumption of both the prototype and commercial systems. For comparison purposes, the equilibrium state at the output voltage of the proposed prototype was also adjusted to 14.4 V since the output voltage from the commercial solar charger to feed the battery is also 14.4 V. The parameters of irradiance E_e, the PV cell output voltage $\{v_{pv}$ and current $i_{pv}\}$, and battery voltage v_{bc2} were collected from the control module governed by the electronic prototyping platform *Teensy* 4.2 all along the experimental testing for both systems, Added, the battery was pre-charged to 12.5 V (around 80% of the entire charge state) for both systems before testing.

5.5 Experimental Results

We exposed the proposed prototype and the commercial solar charger *Victron BlueSolar MPPT* 75/15 to solar irradiance between 11 a.m and 2 p.m. at the earth coordinates

10.007820, −84.151131 on November 2022 to compare the energy demand and reliability of their control modules. The PV cell was first exposed perpendicularly to the sun and then rotated to different positions to emulate irradiance disturbances. The PV cell parameters E_e, T_v, v_{pv}, i_{pv} and the battery voltage v_{bc2} were monitored during the sun irradiance exposition for both systems, to obtain the required data to compare their MPPT and VR controls' behavior.

Fig. 5.7 shows the reliability measurement results of the commercial solar charger *Victron BlueSolar MPPT* 75/15's MPPT and VR control strategies. The PV cell $CL-SM30M$ [137] was connected to feed the commercial solar charger. This system was exposed to irradiance fluctuations E_e between 1100 to 600 W/m^2 for a period t of 45 s at 48 °C, as depicted in the black solid line of the graphic *a) Sun irradiance* (E_e) *vs time* (t) of the figure. The MPPT control strategy of the commercial solar charger (solid green line) meets the *MPPT control target* (red dotted line) at irradiances below $800W/m^2$, into the time range from 13 to 34 seconds approximately. Still, it failed out of this range, at irradiances above 800 W/m^2, out of the time range from 13 to 34 s, as depicted in the graphic *b) PV cell output power* (P_{pv}) *vs time* (t). Contrariwise, the VR control strategy (solid green line) reaches 14.4 V of the *VR control target* (red dotted line) above to 800 W/m^2, out of the time range from 13 to 34 s, and fails the control performance into the time range from 13 to 34 s, where the irradiance magnitude remains below 800 W/m^2, as shown in the graphic *c) Battery Voltage* (v_{bc2}) *vs time* (t). Thus, based on the *MPPT control target*, at irradiation levels up to 800 W/m^2 the MPPT of the commercial controller collapses; e.g., at given irradiation of 1000 W/m^2 the theoretical PV cell output power P_{pv} must be 29 W, but falls to 23 W. Conversely, when the irradiation falls below 800 W/m^2, the VR breaks off, and the battery voltage collapses, moving away from the *VR control target*. At the same time, the MPPT recovers to the target correctly. Hence, since the MPPT and VR controllers collapsed alternately at input levels lower than 29 W and the battery load demands 6 W on charging state, then we conclude that the control hardware of the commercial battery charger expends at least 23 W.

Furthermore, we evaluate the control strategies MPPT and VR of the proposed prototype by exposing the PV cell $CL-SM30M$ under irradiance fluctuations E_e between 800 to 500 W/m^2 for a period t of 30 s at 42 °C, as depicted in the solid black line of the graphic *a) Sun irradiance* (E_e) *vs time* (t) on the Fig. 5.8). As shown in the graphic *b) PV cell output power* (P_{pv}) *vs time* (t), the MPPT control strategy of the prototype reaches the *MPPT control target* (red dotted line) all along the test period. Nevertheless, the PV cell output power p_{pv} fluctuates at 500 W/m^2 at 12 W power level and recovers up to this magnitude. Equivalently, at any irradiance, the VR control strategy (solid green line) reaches the *VR control target* (red dotted line) but also fluctuates at 500 W/m^2. Hence, the prototype system's MPPT and VR controllers can support the battery power at 12 W lower input power P_{pv}, being 6 W the controllers' consumption of the proposed prototype. We highlight that a few noises affect the controllers' responses due to the prototype's double-switching nature, as shown in Fig. 5.8.

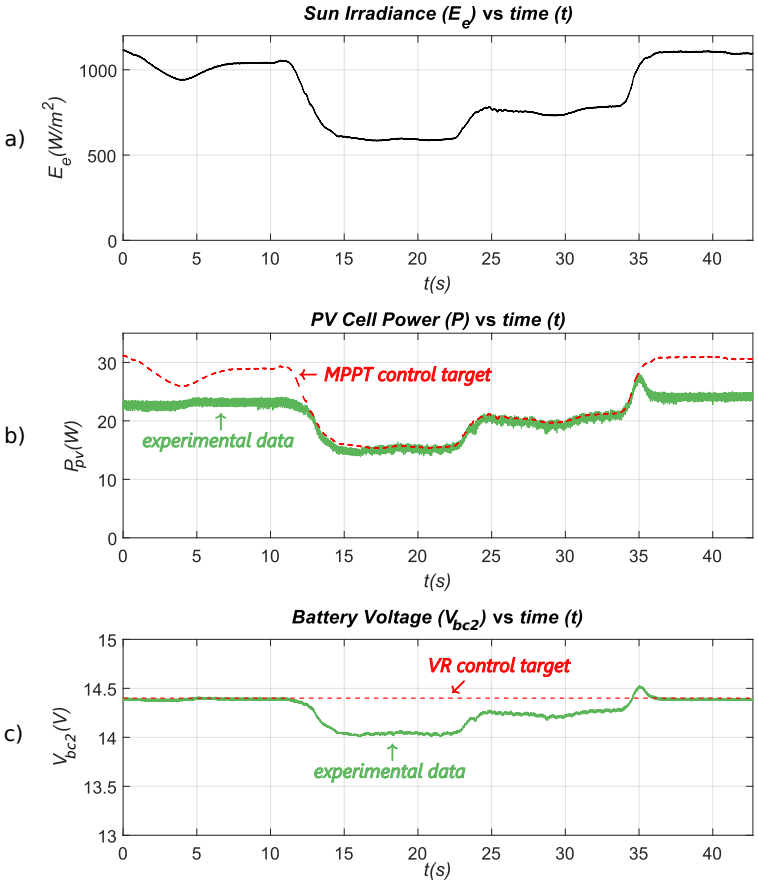

Figure 5.7: Response of the PV cell output power P_{pv} in *b)*, and the DC-DC stage converter output voltage v_{bc2} in *c)*, of the commercial solar charger with MPPT and VR controllers at 48 °C, to a natural solar input irradiance E_e in *a)*.

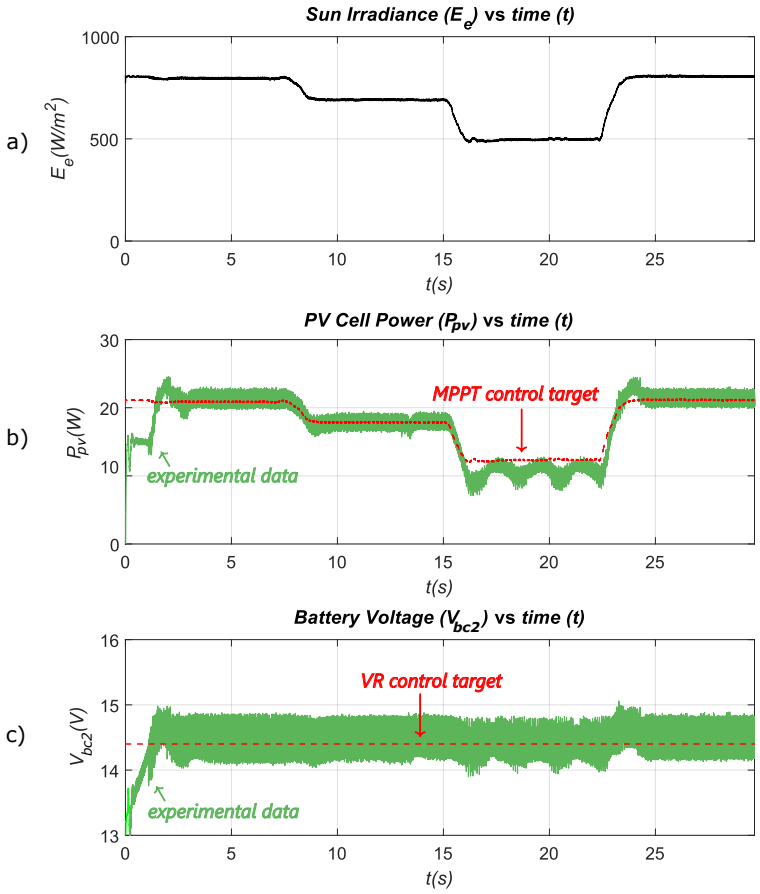

Figure 5.8: Response of the PV cell output power P_{pv} in *b)*, and the DC-DC stage converter output voltage v_{bc2} in *c)*, of the proposed prototype with MPPT and VR controllers at 42 °C, to a natural solar input irradiance E_e in *a)*.

5.6 Concluding Remarks and Future Work

We have modeled an MPPT and a VR-controlled system, integrating a PV cell and a DC-DC buck-boost converter to charge a $12V$ battery. The model was released in the PH framework, and the controllers were developed in an IDA-PBC strategy. The system was implemented in a prototype to verify the MPPT and the VR control design. To develop the prototype's MPPT and VR controllers, we adapted the control strategy in a two-states control signal over the switches of the DC-DC buck and the DC-DC boost converters.

The prototype and a commercial solar charge were tested under natural sun irradiance conditions by connecting each system to a 30 W PV cell to feed a 6 W charging power commercial battery to evaluate the proposed controllers' reliability. As a result, the commercial solar charger demonstrates erratic behavior at 29 W input power and collapses under this power level. Hence, we determine that the power demand of the commercial solar charger controller is estimated at at least 23 W. Contrariwise, the proposed prototype collapsed at 12 W input power, and then the power demand of the proposed controller is estimated at 6 W.

This chapter compares the reliability of the MPPT and VR controllers between a proto-

type and a commercial solar charger under natural irradiance conditions, including temperature corrections. As far as we know, this is the first time this comparison has been made.

Chapter 6

Conclusions and Outlook

6.1 Conclusions

Recapitulation of our surveys from Chapters 3, 4, and 5 in this thesis, we can summarise the subsequent conclusions. It is demonstrated that the PH framework energy-based approach becomes a suitable modeling tool, able to set and concatenate nonlinear systems of different physical domains.

The resulting model from a PH framework transparently shows the interconnection between the physical stages, allowing modification of the equivalent physical parameters quickly to tune and evaluate the effect of the system's behavior.

Added, the PH model explicitly displays the input and output state variables, and the energy dissipation and storage elements are highlighted in separated matrices, simplifying the understanding of the energy flow and the interaction of the stages.

The transparency of the PH framework modeling allows for to proposed and evaluate nonlinear control strategies. Those strategies are mainly aimed at modifying the distribution or consumption of energy by changing the original system structure and preserving the PH model attributes.

The IDA-PBC strategy demonstrates high performance in controlling a PV cell system's MPPT to feed a load across a DC-DC converter. This system has a stochastic behavior since the input irradiance state is entirely independent regarding time. Hence, the IDA-PBC strategy is designed from a proposed close-loop structure that complies with several statements to reach global stability.

Furthermore, an IDA-PBC strategy to control both MPPT and VR at the input and output of a double switch highly nonlinear DC-DC converter stage has demonstrated a performance better than a homologous commercial device, even in terms of energy consumption.

6.2 Outlook

Finally, from our results, we provide recommendations on the next possible future lines:

- The parameters nonlinear behavior described in the PV cell internal equivalent circuit applied for the proposed systems was assumed into the $i_s\left(E_e\right)$ current as part of the

input matrix $g(x)$. Since this matrix is explicitly contained in the solution of control law function $\beta(x)$, the PV cell model nonlinear parameters are included in the control strategy when the PDE is solved. However, those nonlinear terms (specifically the dependence of the current i_D from the state variable v_{pv}) can be extended into the interconnection and dissipation matrices of the mathematical model the PV cell.

- Although the home-designed circuit to evaluate the proposed control strategy was implemented in a Bipolar Junction Transistors topology to ensure the system reaches high-frequency switching actuation, it's possible to implement the control with more power-efficient semiconductor devices, such as Junction Field-Effect Transistors.

- The IDA-PBC was successfully proposed and evaluated to solve the MPPT and VR issues of a photovoltaic energy harvesting system. Moreover, other nonlinear PH framework-compatible strategies could be designed and evaluated; e.g., the so-called *Error Trajectory Tracking* strategy has been proposed to control PH systems via canonical transformations and passivity-based control [140, 141].

- In terms of extending the scope of the physical system, we suggest designing a control strategy for other renewable energy sources where power extraction represents an important issue, i.e., wind energy-powered systems.

- A DC-AC converter stage to connect output AC loads could also be added to evaluate the system's performance under both DC and AC consumption environments. Similarly, a DC-AC 3-phase converter stage could allow connecting high-power and inductive loads, i.e., motor, water pumps, or a complete PHS system to verify the high-power performance of the control strategies, under stand-alone and grid-connected circumstances.

Appendix A

MPPT Methods Classification

Table A.1: MPPT Methods Classification by the Scope

Classification	**MPPT Method**
Conventional	Perturb and Observe (P&O) [142, 143, 144, 145, 146, 147, 148, 149, 150, 151, 152, 153, 154, 29, 155, 156, 157, 158]; Incremental Conductance (INC) [29, 75, 159, 160, 161, 162, 163, 164, 165, 154]; Differential Fixed-step Size (DFS) and Differential Variable-step Size (DVS) [160, 161, 164]; Hill-Climbing (HC) [166, 167, 151, 168, 29]
Mathematics	Linear Reoriented Coordinates Method (LRCM) [20, 169, 21, 170]; Curve Fitting [171, 20]; Incremental Resistance (INR) [20, 172, 173, 174, 175]; Beta [176, 20, 177, 178, 179, 180]; Ripple Correlation Control (RCC) [181, 20, 182]; Analytical solution (AS) [183, 184, 185, 186, 187]
Measurement and Comparison	Look-up Table [188, 152]; Load Current or Voltage Maximisation (LCVM) [189, 20]; Linear Current Control (LCC) [190, 191, 192, 193]; Current Sweep [194, 195, 20]
Constant Parameters	Constant Voltage (CV) and Constant Current (CC) [20, 196, 154, 197]; Open Circuit Voltage (OCV), Fractional Open Circuit Voltage (FOCV) and Fractional Short Circuit Current (FSCC) [198, 199, 200, 29, 196]; pn Junction Drop Voltage Tracking [20, 27]; Best Fixed Voltage (BFV) and Temperature Parametric (TP) [20, 27, 201]
Trial and Error	Output Senseless (POS) [202, 20]; Three Point Comparison [203, 20]; DC-Link Capacitor Droop [20, 202]; Variable Inductor [20, 202]; Gradient Descent [204, 205]; Sliding Mode Controller (SMC) [79, 206, 207, 132, 208, 209, 133, 210, 211, 80, 212]; Extremum Seeking Method (ESM) [213, 20, 214, 215]
Numerical	Newton–Raphson (NR) [216, 217, 218]; The Secant Method (SM) [219, 220, 221]; Central Point Iterative (CPI) [20, 222]; False Position Method (FPM) and Bisection Search Method (BSM) [223]; Brent method (BM) [224, 20]
Intelligent Prediction and Iterative in Nature	Fuzzy Logic (FL) [225, 226, 227, 228, 229, 230, 231, 232, 233, 234, 156, 235]; Artificial Neural Network (ANN) [225, 236, 237, 238, 239, 240, 241, 242, 243, 231, 235, 244, 245]; Adaptive Neuro-Fuzzy Inference System (ANFIS) [20, 246, 247, 248, 249, 250, 251]; Evolutionary Algorithm (EA) [252, 20]; Particle Swarm Optimization (PSO) [253, 254, 155, 255, 256, 257, 258, 259, 260, 158, 86], Genetic Algorithm (GA) [261, 262, 263, 235], Fruit Fly Optimization (FFO) [261, 264], Firefly Algorithm (FA) [265, 266, 254, 155, 267, 268, 261, 157], Cuckoo Search (CS) [255, 269, 270, 271, 272, 244, 158], Teaching Learning Based Optimization (TLBO) [256, 273, 274, 275], Grey Wolf Optimization (GWO) [256, 276, 277, 278, 279, 280], Ant Colony Optimization (ACO) [281, 282, 283, 284], Flower Pollination Algorithm (FPA) [285, 286, 287, 156, 288, 289, 157], Artificial Bee Colony (ABS) [284, 290, 291, 292], Differential Evolution (DE) [293, 294, 295, 296], Bat Algorithm (BA) [297, 298, 299, 300], Whale Optimization Algorithm (WOA) [278, 301, 302, 303, 304]
Passivity-Based	Passivity-based controllers (PBC) [30, 31, 32, 33, 34, 35, 36, 37, 38, 39, 40, 41]

Appendix B

Several Reported Hybrid MPPT Techniques

GWO and ANN [305]; GWO-optimized FL [306]; FL with four different optimizations: TLBO, FF, Biogeography Based Optimization (BBO) and PSO [307]; CS and GWO [308]; CS and Golden Section Search [309]; GA to optimize the FL [310, 80]; GA and FOCV [311]; IC and PSO [312]; ACO to train a developed ANN [313]; optimization of Fractional Order (FO) with INC [314]; ABC and Semi-supervised Extreme Learning Machine [315]; TLBO and ABC [316]; ABC and P&O [317]; PSO and Optimum-Relation-Based (ORB) [318]; FL and BA [319]; Overall Distribution (OD) integrated and PSO [320]; optimization of a Fractional Chaotic FPA [321]; FPA assisted by P&O [322]; GA and ACO [323]; DE and GA [324]; ANFIS and ABC [325]; FO-based ANFIS combined and P&O [326]; Opposition-based learning (OBL) and FA [327]; GA, FA and DE [328]; FPM and HC [329]; BA with CS [330]; ABC and P&O [331], WOA and Simulated Annealing (SA) [332]; WOA, Pattern Search (PS), INC and ANFIS [333]; Model Predictive Control (MPC) and ESM [334]; PSO to improve SFLAESM and MPC [335]; SFLA modified by SMC and P&n [336]; FL tuned via SFLA [337]; P&O, CC and CV [338]; FL and ANN in [339, 340]; INC and CV [341]; P&O based on Pythagorean theorem and CV in [342]; ANN and NR [343]; NR and P&O [344]; SM based on NR [345]; BAT algorithm using Cultural Evolution Process [346]; CV, INC and PSO [347]; FL optimized by SFLA [348]; PSO and Adaptive Linear Active Disturbance Rejection Control (A-LADRC) [349]; Load Current Maximization(LCM) and P&O [350]; P&O and CV [351]; FL and BAT [352]; SFLA and P&O [353]; HC and FL [354]; beta parameter and FL [355, 356]; HC, FOCV and FSCC [357]; P&O and Look-Up Table [358, 359]; IC, CV and look-up table [360]; ABC and simultaneous heat transfer search [361]; P&O and Current Sweep in [362]; a variant of PSO known as Adaptive Perceptive PSO in [363]; ANN with MPC using Kalman Filter (KF) [364]; PSO and DE [85]; DE and Jaya optimization based [365]; Magic Square (MS) array and DE-based adaptive P&O [366]; two different hybrid algorithms of WOA and improved DE in [367]; GWO and DE [368]; Salp Swarm Algorithm (SSA), DE and P&O [369]; combinations of the Bat-based algorithm with P&O, IC and Beta, named as Bat-P&O, Bat-Beta and Bat-IC [370].

Appendix C

MPPT and Voltage Regulation Unified Control

Table C.1: MPPT and Voltage Regulation Methods Unified Control

Hardware	**MPPT Method**	**Voltage Regulation Method**	**Validation**
Two-stage DC-DC converter	P&O	Not detailed	Simulated
DC-DC boost converter and a DC-AC 3f inverter	Steped P&O	Modified Synchronous Reference Frame (MSRF)	Laboratory bench emulated
Two-stage three-switches DC-DC boost	P&O	Fractional Order Proportional Integral (FOPI)	Simulated
Sepic converter and DC-DC buck-boost stage	INC	Duty cycle pulse width	Simulated
Two sepic converters	P&O	Passivity Based (PB)	Simulated
Single-stage power converter	P&O frequency	Duty cycle pulse width	Simulated
Two-input DC-DC buck converter	Small-signal modeling	Small-signal modeling	Laboratory bench emulated
DC-DC boost converter and a DC-AC 3f inverter	Integral SMC	Space Vector Modulation (SVM)	Simulated
DC-DC boost converter and a DC-AC converter	Proportional-Integrative	AC signal Voltage-frequency (V-f)	Simulated

Appendix D

Nonlinear Stability

Consider an autonomous (time-invariant) [371, 372] system given by

$$\dot{x} = f(x), \tag{D.1}$$

where $f : D \to \mathbb{R}^n$ is a locally Lipschitz map from a domain $D \in \mathbb{R}^n$ into $\mathbb{R}^n$, with an equilibrium point x^* such that $f(x^*) = 0$. Let's assume that $x^* = 0$. Based on the Lyapunov stability, the equilibrium stability in x^* of the given system (D.1) can be classified into several categories:

- Stable: The system remains close to the equilibrium point or trajectory for any small perturbation in the initial conditions; for each $\varepsilon > 0$ there is a $\delta = (\varepsilon) > 0$, such that

$$\| x(0) \| < \delta \Rightarrow \| x(t) \| < \varepsilon, \ \forall \ t \geq 0$$

- Asymptotic Stable: All trajectories that start sufficiently close to the equilibrium point converge to the equilibrium point as time approaches infinity, literally

$$\| x(0) \| < \delta \Rightarrow \lim_{t \to \infty} x(t) = 0$$

- Exponential Stable The trajectories converge to the equilibrium point exponentially, such that the system reaches the equilibrium point at an increasingly faster rate as time progresses, more precisely

$$< \delta \Rightarrow \lim_{t \to \infty} \dot{f}(x) < 0$$

- Global Stable All trajectories converge to the equilibrium point regardless of the initial conditions. Only in global stability the concept of a stable system can apply.

$$\forall \ \ \| x(0) \| \ \ \Rightarrow \lim_{t \to \infty} x(t) = 0$$

Characterizing stability properties allows for understanding complex systems' behavior and designing control strategies to ensure stability and reliable operation.

Appendix E

Lyapunov Function

In the context of the Lyapunov theory, stability refers to the behavior of a dynamical system over time. It provides insights into the system's long-term behavior and convergence properties. The Lyapunov theory is widely used to analyze the stability of dynamical systems. This theory relies on the Lyapunov function concept. A Lyapunov function is a scalar function that satisfies specific properties, such as being positive definite, continuously differentiable, and having a negative definite derivative along the trajectories of the system. Lyapunov functions assigns a value to each system state. It characterizes the system's energy or potential at a particular state. The key idea is that if a Lyapunov function can be found for a given system, its behavior can be analyzed to determine stability properties [371, 372].

Consider a scalar function $V(x)$ to be positive definite that complies the following conditions

- $V(x)$ and its first partial derivatives are continuous together in a given open region Ω surrounding the origin $x^* = 0$.
- $V(0)$=0.
- $V(x)$ is positive outside the origin $x^* = 0$ (and always in Ω). Hence, $V(x)$ vanishes only at the origin and $x^* = 0$ becomes an isolated minimum of $V(x)$.

  If the derivative $\dot{V}(x) \leq 0$, then the equilibrium point $x^* = 0$ is *stable*.

  If the derivative $\dot{V}(x) \leq 0$ in $\Omega - \{0\}$, then the equilibrium point $x^* = 0$ is *asymptotically stable*.

  The scalar function $V(x)$ is the so-called Lyapunov function that describes the stability of the equilibrium point x^*

Appendix F

Electric Diagram of the DC-DC Boost Converter Switching Control

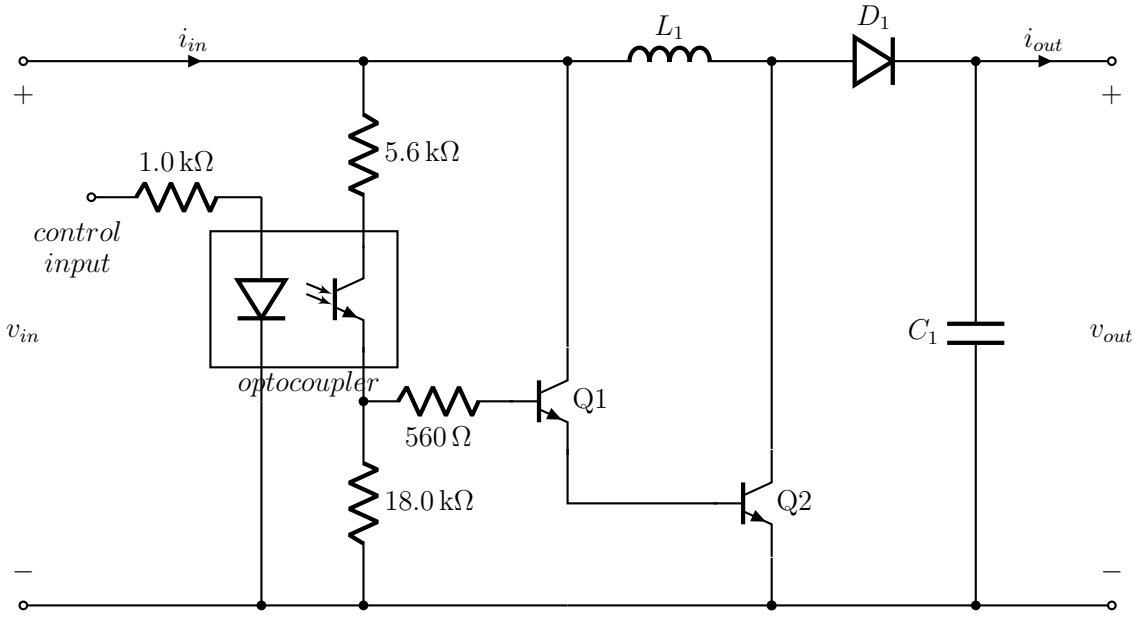

Figure F.1: Electric diagram of the DC-DC boost converter controller to governed a normally closed (NC) switch S_{boost}.

Appendix G

Electric Diagram of the DC-DC Buck Converter Switching Control

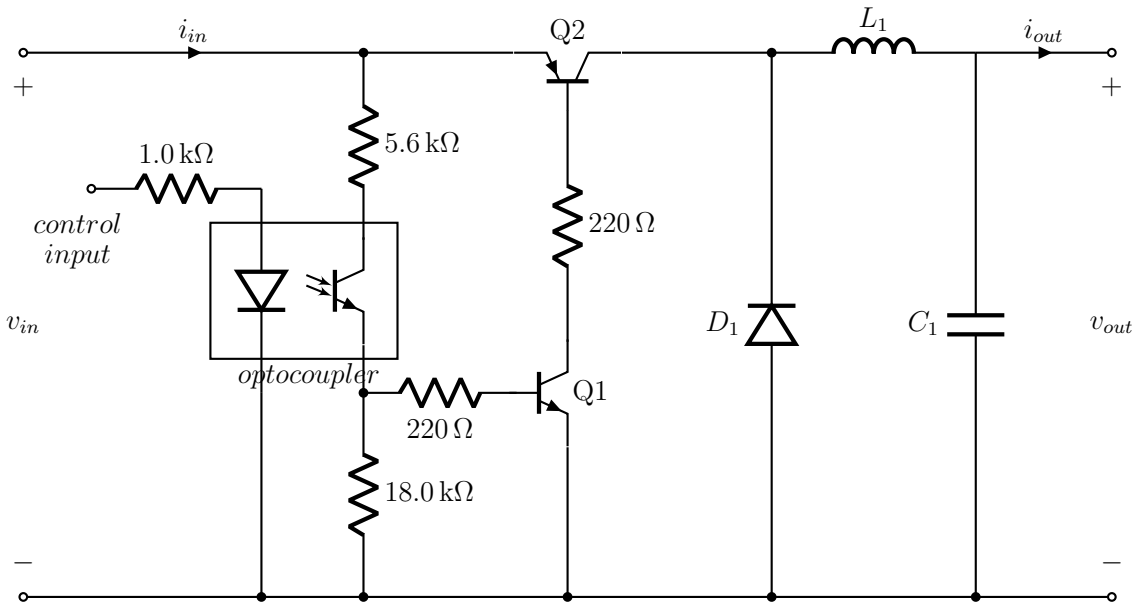

Figure G.1: Electric diagram of the DC-DC buck converter controller to governed a normally open (NO) switch S_{buck}.

Appendix H

Sliding Mode Control Strategy

This strategy considers the dynamics of the input and output states of a DC-DC transfer system to perform on two operation modes: *approach* and *sliding*. In the approach mode, the system states converge to a finite-time predefined domain known as the sliding function σ_1. The sliding mode is also called σ_2, where the states of the system are restricted to operate over a sliding surface that reaches the system's origin, as in [206, 132, 133]. Given the electrical power supplied by the PV cell system at the DC-DC transfer system input, i.e., P_{pv}, and its input voltage and current v_{pv} and i_{pv}, the partial-derivative $\nabla_{v_{pv}} P_{pv} = 0$ can be chosen as the sliding surface for the MPPT objective, such that the states of the system persistently lies on the maximum power transference trajectory. Hence, the sliding surface is defined as

$$\nabla_{v_{pv}} P_{pv} = v_{pv} \left(\nabla_{v_{pv}} i_{pv} + \frac{i_{pv}}{v_{pv}} \right). \tag{H.1}$$

From (H.1), we can define the sliding mode σ_2 as

$$\sigma_2 (t, x) = \nabla_{v_{pv}} i_{pv} + \frac{i_{pv}}{v_{pv}}. \tag{H.2}$$

Moreover, the system dynamics $\dot{x}$ are given by

$$\dot{x} = \mathcal{F}(x) + \mathcal{G}(x)\, \sigma_1, \tag{H.3}$$

where the approach sliding function σ_1 is obtained by solving the PDE

$$\dot{\sigma}_1 = [\nabla_x \sigma]^\top \dot{x} = 0. \tag{H.4}$$

Similarly to [133], we assume that $[\partial \sigma / \partial x]^\top$ is a reversible matrix, and (H.4) is solved as

$$\sigma_1 = -\frac{[\nabla_x \sigma]^\top}{[\nabla_x \sigma]^\top} \frac{\mathcal{F}(x)}{\mathcal{G}(x)} = 1 - \frac{v_{pv}}{v_L}. \tag{H.5}$$

Hence, the approach mode is obtained from solving the sliding function σ_1, and the control algorithm for the controller is completed. Subsequently, from this SMC algorithm, it is proposed a switch control signal S_{SM} as in [133], to govern the DC-DC transfer system by controlling the duty cycle. Then, S_{SM} is given by

$$S_{SM} = \begin{cases} 1 & \text{for} \quad \sigma_1 + k\sigma_2 \geq 1 \\ \sigma_1 + k\sigma_2 & \text{for} \quad 0 < \sigma_1 + k\sigma_2 < 1 \\ 0 & \text{for} \quad \sigma_1 + k\sigma_2 \leq 0, \end{cases} \tag{H.6}$$

where k is a positive magnitude scaling constant suitable to adjust the SMC strategy performance.

References

[1] Julio Matamoros Alfaro. Informe de atención de demanda y producción de energía con fuentes renovables, costa rica 2022. Technical report, División Operación y Control del Sistema Eléctrico (DOCSE), Grupo ICE, 2022.

[2] Dolf Gielen, Francisco Boshell, Deger Saygin, Morgan D. Bazilian, Nicholas Wagner, and Ricardo Gorini. The role of renewable energy in the global energy transformation. *Energy Strategy Reviews*, 24:38–50, 2019.

[3] Maria Mercedes Vanegas Cantarero. Of renewable energy, energy democracy, and sustainable development: A roadmap to accelerate the energy transition in developing countries. *Energy Research & Social Science*, 70:101716, 2020.

[4] Muhammad Shahbaz, Chandrashekar Raghutla, Krishna Reddy Chittedi, Zhilun Jiao, and Xuan Vinh Vo. The effect of renewable energy consumption on economic growth: Evidence from the renewable energy country attractive index. *Energy*, 207:118162, 2020.

[5] Taner Güney. Renewable energy, non-renewable energy and sustainable development. *International Journal of Sustainable Development & World Ecology*, 26(5):389–397, 2019.

[6] Nuno Silva, José Alberto Fuinhas, and Matheus Koengkan. Assessing the advancement of new renewable energy sources in latin american and caribbean countries. *Energy*, 237:121611, 2021.

[7] Akhtar Hussain, Syed Muhammad Arif, and Muhammad Aslam. Emerging renewable and sustainable energy technologies: State of the art. *Renewable and Sustainable Energy Reviews*, 71:12 – 28, 2017.

[8] Kenneth Hansen, Christian Breyer, and Henrik Lund. Status and perspectives on 100% renewable energy systems. *Energy*, 175:471 – 480, 2019.

[9] Proceso de Expansión del Sistema de Planificación y Desarrollo Eléctrico. Proyecciones de la demanda eléctrica de costa rica 2018-2040. Technical report, INSTITUTO COSTARRICENSE DE ELECTRICIDAD, 2018.

[10] Jaime Wright. Estudio del potencial solar en Costa Rica. *Uniciencia*, 23(1-2):19–40, 2009.

[11] Sadeq D. Al-Majidi, Maysam F. Abbod, and Hamed S. Al-Raweshidy. A novel maximum power point tracking technique based on fuzzy logic for photovoltaic systems. *International Journal of Hydrogen Energy*, 43(31):14158 – 14171, 2018.

[12] Maroua Haddad, Jean Nicod, Yacouba Boubacar Mainassara, Landy Rabehasaina, Zeina Al Masry, and Marie Péra. Wind and Solar Forecasting for Renewable Energy System using SARIMA-based Model. In *International conference on Time Series and Forecasting*, Gran Canaria, Spain, September 2019.

[13] Salvador I. Pérez-Uresti, Ricardo M. Lima, Mariano Martín, and Arturo Jiménez-Gutiérrez. On the design of renewable-based utility plants using time series clustering. *Computers & Chemical Engineering*, 170:108124, 2023.

[14] Abbes Kihal, Fateh Krim, Billel Talbi, Abdelbaset Laib, and Abdeslem Sahli. A robust control of two-stage grid-tied pv systems employing integral sliding mode theory. *Energies*, 11(10), 2018.

[15] Atika Qazi, Fayaz Hussain, Nasrudin ABD. Rahim, Glenn Hardaker, Daniyal Alghazzawi, Khaled Shaban, and Khalid Haruna. Towards sustainable energy: A systematic review of renewable energy sources, technologies, and public opinions. *IEEE Access*, 7:63837–63851, 2019.

[16] Pengqing Bi, Shaoqing Zhang, Zhihao Chen, Ye Xu, Yong Cui, Tao Zhang, Junzhen Ren, Jinzhao Qin, Ling Hong, Xiaotao Hao, and Jianhui Hou. Reduced non-radiative charge recombination enables organic photovoltaic cell approaching 19% efficiency. *Joule*, 5:2408–2419, 2021.

[17] Yong Cui, Yuming Wang, Jonas Bergqvist, Huifeng Yao, Ye Xu, Bowei Gao, Chenyi Yang, Shaoqing Zhang, Olle Inganäs, Feng Gao, and Jianhui Hou. Wide-gap non-fullerene acceptor enabling high-performance organic photovoltaic cells for indoor applications. *Nature Energy*, 4:768–775, 2019.

[18] Pabitra K Nayak, Suhas Mahesh, Henry J Snaith, and David Cahen. Photovoltaic solar cell technologies: analysing the state of the art. *Nature Reviews Materials*, 4:269–285, 2019.

[19] Jianqiu Wang, Zhong Zheng, Yunfei Zu, Yafei Wang, Xiaoyu Liu, Shaoqing Zhang, Maojie Zhang, and Jianhui Hou. A tandem organic photovoltaic cell with 19.6% efficiency enabled by light distribution control. *Advanced Materials*, 33:2102787, 2021.

[20] Amit Kumer Podder, Naruttam Kumar Roy, and Hemanshu Roy Pota. Mppt methods for solar pv systems: a critical review based on tracking nature. *IET Renewable Power Generation*, 13(10):1615–1632, 2019.

[21] Mohammad Sarvi and Ahmad Azadian. A comprehensive review and classified comparison of mppt algorithms in pv systems. *Energy Systems*, 13:281–320, 2022.

[22] Saad Motahhir, Aboubakr El Hammoumi, and Abdelaziz El Ghzizal. The most used mppt algorithms: Review and the suitable low-cost embedded board for each algorithm. *Journal of Cleaner Production*, 246:118983, 2020.

[23] Mostefa Kermadi, Zainal Salam, Ali M. Eltamaly, Jubaer Ahmed, Saad Mekhilef, Cherif Larbes, and El Madjid Berkouk. Recent developments of mppt techniques for pv systems under partial shading conditions: a critical review and performance evaluation. *IET Renewable Power Generation*, 14(17):3401–3417, 2020.

[24] Bidyadhar Subudhi and Raseswari Pradhan. A comparative study on maximum power point tracking techniques for photovoltaic power systems. *IEEE transactions on Sustainable Energy*, 4(1):89–98, 2012.

[25] Paramatmuni Sarath Samrat, Fonkwe Fongang Edwin, and Weidong Xiao. Review of current sensorless maximum power point tracking technologies for photovoltaic power systems. In *2013 International Conference on Renewable Energy Research and Applications (ICRERA)*, pages 862–867. IEEE, 2013.

[26] Pallavee Bhatnagar and R.K. Nema. Maximum power point tracking control techniques: State-of-the-art in photovoltaic applications. *Renewable and Sustainable Energy Reviews*, 23:224 – 241, 2013.

[27] Nabil Karami, Nazih Moubayed, and Rachid Outbib. General review and classification of different mppt techniques. *Renewable and Sustainable Energy Reviews*, 68:1–18, 2017.

[28] Md Tofael Ahmed, Masud Rana Rashel, Fahad Faisal, and Mouhaydine Tlemçani. Non-iterative mppt method: A comparative study. *International Journal of Renewable Energy Research*, 10:549–557, 2020.

[29] Riaz Ahmad, Ali F. Murtaza, and Hadeed Ahmed Sher. Power tracking techniques for efficient operation of photovoltaic array in solar applications – a review. *Renewable and Sustainable Energy Reviews*, 101:82–102, 2019.

[30] J. Linares-Flores, A. Hernández-Méndez, J.A. Juárez-Abad, M. A. Contreras-Ordaz, and C. García-Rodriguez. Mppt novel controller based on passivity for the pv solar panel-boost power converter combination. In *2021 IEEE Energy Conversion Congress and Exposition (ECCE)*, pages 310–315, 2021.

[31] Mustafa Alrayah Hassan, Er-Ping Li, and Song Chi. Passivity-based control of dc-dc boost power converter for mppt used in dc microgrid systems. In *2018 2nd IEEE Conference on Energy Internet and Energy System Integration (EI2)*, pages 1–6, 2018.

[32] Jacob J. Vásquez S., Jorge A. Domínguez A., Mario Espinosa T., Marco A. Alonso P., Edgardo Yescas Mendoza, and Jesús Linares Flores. Passivity based-control of output voltage regulation with mppt for photovoltaic panel using two sepic converters. In *2020 IEEE International Autumn Meeting on Power, Electronics and Computing (ROPEC)*, volume 4, pages 1–6, 2020.

[33] Isaac Ortega Velázquez, Gerardo René Espinosa Pérez, Oscar Danilo Montoya Giraldo, Alejandro Garcés Ruiz, and Luis Fernando Grisales Noreña. Current control mode in pv systems integrated with dc-dc converters for mppt: An ida-pbc approach. In *2018 IEEE Green Technologies Conference (GreenTech)*, pages 1–6, 2018.

[34] Hayden Phillips-Brenes, Roberto Pereira-Arroyo, Renato Rímolo-Donadío, and Mauricio Muñoz-Arias. Current-sensorless control strategy for the mppt of a pv cell: An energy-based approach. *International Journal of Photoenergy*, 2022:1747533, 2022.

[35] Ali Tofighi and Mohsen Kalantar. Interconnection and damping assignment and euler-lagrange passivity-based control of photovoltaic/battery hybrid power source for stand-alone applications. *Journal of Zhejiang University SCIENCE C*, 12:774–786, 2011.

[36] Isaac Ortega Velázquez, Gerardo René Espinosa Pérez, Oscar Danilo Montoya Giraldo, Alejandro Garcés Ruiz, and Luis Fernando Grisales Noreña. Current control mode in pv systems integrated with dc-dc converters for mppt: An ida-pbc approach. In *2018 IEEE Green Technologies Conference (GreenTech)*, pages 1–6, 2018.

[37] Anamika, Soumya Samanta, Sudhansu Mishra, and T. Ghosh. Control of dc microgrid using interconnection and damping assignment passivity based control method. In *2022 IEEE 7th International conference for Convergence in Technology (I2CT)*, pages 1–6, 2022.

[38] Soumya Samanta, Saumitra Barman, Jyoti Prakash Mishra, Prasanta Roy, and Binoy Krishna Roy. Energy management and damping improvement of a dc microgrid with constant power load using interconnection and damping assignment-passivity based control. *Transactions of the Institute of Measurement and Control*, 43(7):1545–1559, 2021.

[39] Ricardo Ramiro Peña, Juan Ignacio Talpone, Ricardo Mantz, and Pedro Battaiotto. Mppt for a photovoltaic system under partial shaded conditions. In *2020 IEEE International Conference on Industrial Technology (ICIT)*, pages 65–70, 2020.

[40] Chaima Ghanjati, Slim Tnani, Patrick Coirault, Jamel Belhadj, and Habib Cherif. Design and implementation of an interconnection and damping assignment–passivity-based control for grid-integrated hybrid renewable system with energy storage. *Proceedings of the Institution of Mechanical Engineers, Part I: Journal of Systems and Control Engineering*, 235(7):1011–1022, 2021.

[41] Shengzhao Pang, Babak Nahid-Mobarakeh, Serge Pierfederici, Matheepot Phattanasak, Yigeng Huangfu, Guangzhao Luo, and Fei Gao. Interconnection and damping assignment passivity-based control applied to on-board dc–dc power converter system supplying constant power load. *IEEE Transactions on Industry Applications*, 55(6):6476–6485, 2019.

[42] Pavel Ripka. Electric current sensors: a review. *Measurement Science and Technology*, 21(11):112001, sep 2010.

[43] Morcos Metry, Mohammad B Shadmand, Robert S Balog, and Haitham Abu-Rub. Mppt of photovoltaic systems using sensorless current-based model predictive control. *IEEE Transactions on Industry Applications*, 53(2):1157–1167, 2016.

[44] Zhen Xin, He Li, Qing Liu, and Poh Chiang Loh. A review of megahertz current sensors for megahertz power converters. *IEEE Transactions on Power Electronics*, 37(6):6720–6738, 2022.

[45] Nobuyuki Kasa, Takahiko Iida, and Liang Chen. Flyback inverter controlled by sensorless current mppt for photovoltaic power system. *IEEE Transactions on Industrial Electronics*, 52(4):1145–1152, 2005.

[46] Morcos Metry and Robert S. Balog. An adaptive model predictive controller for current sensorless mppt in pv systems. *IEEE Open Journal of Power Electronics*, 1:445–455, 2020.

[47] Xingshuo Li, Huiqing Wen, Yihua Hu, and Lin Jiang. Drift-free current sensorless mppt algorithm in photovoltaic systems. *Solar Energy*, 177:118–126, 2019.

[48] José-Enrique Hernández-Díez, César-Fernando Méndez-Barrios, Silviu-Iulian Niculescu, and Ernesto Bárcenas-Bárcenas. A current sensorless delay–based control scheme for mppt–boost converters in photovoltaic systems. *IEEE Access*, 8:174449–174462, 2020.

[49] Resat Celikel and Ahmet Gundogdu. System identification-based mppt algorithm for pv systems under variable atmosphere conditions using current sensorless approach. *International Transactions on Electrical Energy Systems*, 30(8):e12433, 2020.

[50] Nabil Obeidi, Mostefa Kermadi, Bachir Belmadani, Abdelkarim Allag, Lazhar Achour, and Saad Mekhilef. A current sensorless control of buck-boost converter for maximum power point tracking in photovoltaic applications. *Energies*, 15(20), 2022.

[51] Dhiman Das, Sreedhar Madichetty, Bhim Singh, and Sukumar Mishra. Luenberger observer based current estimated boost converter for pv maximum power extraction—a current sensorless approach. *IEEE Journal of Photovoltaics*, 9(1):278–286, 2019.

[52] Ahsan Nadeem, Hadeed Ahmed Sher, Ali Faisal Murtaza, and Nisar Ahmed. Online current-sensorless estimator for pv open circuit voltage and short circuit current. *Solar Energy*, 213:198–210, 2021.

[53] Shabbir S Bohra. Dc-current sensor-less mppt based grid-fed single-phase photovoltaic (pv) micro-inverter. *Applied Solar Energy*, 56:85–93, 2020.

[54] Madisa V. G. Varaprasad and Somnath Maity. Microcontroller-based current sensorless photovoltaic mpp tracker. In *2018 8th IEEE India International Conference on Power Electronics (IICPE)*, pages 1–6, 2018.

[55] Afaq Hussain, Hadeed Ahmed Sher, Ali Faisal Murtaza, and Kamal Al-Haddad. A novel sensor-less current technique for photovoltaic system using dc transformer model based model predictive control. *International Journal of Electrical Power & Energy Systems*, 122:106165, 2020.

[56] Madisa V. G. Varaprasad and Somnath Maity. Development of current sensorless photovoltaic mpp tracker. In *2019 International Conference on Computer, Electrical & Communication Engineering (ICCECE)*, pages 1–5, 2019.

[57] Dhiman Das, Sreedhar Madichetty, Bhim Singh, and Sukumar Mishra. Luenberger observer based current estimated boost converter for pv maximum power extraction—a current sensorless approach. *IEEE Journal of Photovoltaics*, 9(1):278–286, 2018.

[58] Bong-Yeon Choi, Jin-Woo Jang, Young-Ho Kim, Young-Hyok Ji, Yong-Chae Jung, and Chung-Yuen Won. Current sensorless mppt using photovoltaic ac module-type flyback inverter. In *2013 IEEE International Symposium on Industrial Electronics*, pages 1–6. IEEE, 2013.

[59] Sol Moon, Seong-Jin Kim, Jeong-Won Seo, Joung-Hu Park, Changkun Park, and Chan-Su Chung. Maximum power point tracking without current sensor for photovoltaic module integrated converter using zigbee wireless network. *International Journal of Electrical Power & Energy Systems*, 56:286 – 297, 2014.

[60] Young-Ho Kim, Jun-Gu Kim, Young-Hyok Ji, Chung-Yuen Won, and Tae-Won Lee. Flyback inverter using voltage sensorless mppt for ac module systems. In *The 2010 International Power Electronics Conference-ECCE ASIA-*, pages 948–953. IEEE, 2010.

[61] Young-Ho Kim, Ju-Suk Kang, Sun-Jae Youn, Yong-Chae Jung, and Chung-Yuen Won. Sensorless current balancing and mppt control for photovoltaic ac module type interleaved flyback inverter. In *Proceedings of The 7th International Power Electronics and Motion Control Conference*, volume 2, pages 1363–1367. IEEE, 2012.

[62] Christopher Lohmeier, Jianwu Zeng, Wei Qiao, Liyan Qu, and Jerry Hudgins. A current-sensorless mppt quasi-double-boost converter for pv systems. In *2011 IEEE Energy Conversion Congress and Exposition*, pages 1069–1075. IEEE, 2011.

[63] Jianwu Zeng, Wei Qiao, and Liyan Qu. A single-switch isolated dc-dc converter for photovoltaic systems. In *2012 IEEE Energy Conversion Congress and Exposition (ECCE)*, pages 3446–3452. IEEE, 2012.

[64] Jawad Ahmad. A fractional open circuit voltage based maximum power point tracker for photovoltaic arrays. In *2010 2nd International Conference on Software Technology and Engineering*, volume 1, pages V1–247. IEEE, 2010.

[65] Gamal M. Dousoky and Masahito Shoyama. New parameter for current-sensorless mppt in grid-connected photovoltaic vsis. *Solar Energy*, 143:113 – 119, 2017.

[66] Gamal M Dousoky and Masahito Shoyama. Current-sensorless power-angle-based mppt for single-stage grid-connected photovoltaic voltage-source inverters. In *2013 IEEE Energy Conversion Congress and Exposition*, pages 2757–2763. IEEE, 2013.

[67] Jawad Ahmad and Hee-Jun Kim. A voltage based maximum power point tracker for low power and low cost photovoltaic applications. *International Journal of Electronics and Communication Engineering*, 3(12):2344 – 2347, 2009.

[68] G Escobar, S Pettersson, CNM Ho, M Karppanen, and T Pulli. Pv current sensorless mppt for a single-phase pv inverter. In *IECON 2011-37th Annual Conference of the IEEE Industrial Electronics Society*, pages 3906–3911. IEEE, 2011.

[69] June-Hee Lee, June-Seok Lee, and Kyo-Beum Lee. Current sensorless mppt control method for dual-mode pv module-type interleaved flyback inverters. *Journal of Power Electronics*, 15(1):54–64, 01 2015.

[70] Ibrahim Sefa and Şaban Özdemir. Experimental study of interleaved mppt converter for pv systems. In *2009 35th Annual Conference of IEEE Industrial Electronics*, pages 456–461. IEEE, 2009.

[71] Kazutaka Itako and Takeaki Mori. A new current sensorless mppt control method for pv generation systems. In *2005 European Conference on Power Electronics and Applications*, pages 9–pp. IEEE, 2005.

[72] Kazutaka Itako and Takeaki Mori. A current sensorless mppt control method for a stand-alone-type pv generation system. *Electrical Engineering in Japan*, 157(2):65–71, 2006.

[73] PURASOL. Financiamiento de su proyecto. `https://purasol.co.cr/es/`, 2020.

[74] GREENENERGY. Retorno de inversión de paneles solares. `https://greenenergy.cr/retorno-de-inversion-de-paneles-solares/`, 2020.

[75] Liqun Shang, Hangchen Guo, and Weiwei Zhu. An improved mppt control strategy based on incremental conductance algorithm. *Protection and Control of Modern Power Systems*, 5:14, 2020.

[76] Mariam A. Sameh, M. A. Badr, Mostafa I. Mare, and Mahmoud A. Attia. Enhancing the performance of photovoltaic systems under partial shading conditions using cuttlefish algorithm. In *2019 8th International Conference on Renewable Energy Research and Applications (ICRERA)*, pages 874–885, 2019.

[77] Mohamed AL-Emam, Mostafa I. Marei, and Walid El-khattam. A maximum power point tracking technique for pv under partial shading condition. In *2018 8th IEEE India International Conference on Power Electronics (IICPE)*, pages 1–6, 2018.

[78] Rabindra Nath Shaw, Pratima Walde, and Ankush Ghosh. Iot based mppt for performance improvement of solar pv arrays operating under partial shade dispersion. In *2020 IEEE 9th Power India International Conference (PIICON)*, pages 1–4, 2020.

[79] Ziad M. Ali, Nguyen Vu Quynh, Sajjad Dadfar, and Hiroki Nakamura. Variable step size perturb and observe mppt controller by applying θ-modified krill herd algorithm-sliding mode controller under partially shaded conditions. *Journal of Cleaner Production*, 271:122243, 2020.

[80] R. Ramaprabha, M. Balaji, and B.L. Mathur. Maximum power point tracking of partially shaded solar pv system using modified fibonacci search method with fuzzy controller. *International Journal of Electrical Power & Energy Systems*, 43(1):754 – 765, 2012.

[81] Majad Mansoor, Adeel Feroz Mirza, and Qiang Ling. Harris hawk optimization-based mppt control for pv systems under partial shading conditions. *Journal of Cleaner Production*, 274:122857, 2020.

[82] Muhammad Hamza Zafar, Thamraa Al-shahrani, Noman Mujeeb Khan, Adeel Feroz Mirza, Majad Mansoor, Muhammad Usman Qadir, Muhammad Imran Khan, and Rizwan Ali Naqvi. Group teaching optimization algorithm based mppt control of pv systems under partial shading and complex partial shading. *Electronics*, 9(11), 2020.

[83] Muhammad Hamza Zafar, Noman Mujeeb Khan, Adeel Feroz Mirza, Majad Mansoor, Naureen Akhtar, Muhammad Usman Qadir, Nauman Ali Khan, and Syed Kumayl Raza Moosavi. A novel meta-heuristic optimization algorithm based mppt control technique for pv systems under complex partial shading condition. *Sustainable Energy Technologies and Assessments*, 47:101367, 2021.

[84] Majad Mansoor, Adeel Feroz Mirza, Fei Long, and Qiang Ling. An intelligent tunicate swarm algorithm based mppt control strategy for multiple configurations of pv systems under partial shading conditions. *Advanced Theory and Simulations*, 4(12):2100246, 2021.

[85] Mansi Joisher, Dharampal Singh, Shamsodin Taheri, Diego R. Espinoza-Trejo, Edris Pouresmaeil, and Hamed Taheri. A hybrid evolutionary-based mppt for photovoltaic systems under partial shading conditions. *IEEE Access*, 8:38481–38492, 2020.

[86] Hong Li, Duo Yang, Wenzhe Su, Jinhu Lü, and Xinghuo Yu. An overall distribution particle swarm optimization mppt algorithm for photovoltaic system under partial shading. *IEEE Transactions on Industrial Electronics*, 66(1):265–275, 2019.

[87] Ali Khatibi, Fatemeh Razi Astaraei, and Mohammad Hossein Ahmadi. Generation and combination of the solar cells: A current model review. *Energy Science & Engineering*, 7(2):305–322, 2019.

[88] Luis D Murillo-Soto, Geovanni Figueroa-Mata, and Carlos Meza. Identification of the Internal Resistance in Solar Modules Under Dark Conditions Using Differential Evolution Algorithm. In *2018 IEEE International Work Conference on Bioinspired Intelligence (IWOBI)*, pages 1–9. IEEE, 2018.

[89] Valerio Lo Brano, Aldo Orioli, Giuseppina Ciulla, and Alessandra Di Gangi. An improved five-parameter model for photovoltaic modules. *Solar Energy Materials and Solar Cells*, 94(8):1358 – 1370, 2010. National Conference on the Emerging Trends in the Photovoltaic Energy and Utilization.

[90] Y Chaibi, M Salhi, A El-jouni, and A Essadki. A new method to extract the equivalent circuit parameters of a photovoltaic panel. *Solar Energy*, 163:376–386, 2018.

[91] Mehar-un-Nisa Khursheed, Muhammad Faisal Nadeem Khan, Ghulam Ali, and Ahmed Khalil Khan. A review of estimating solar photovoltaic cell parameters. In *2019 2nd International Conference on Computing, Mathematics and Engineering Technologies (iCoMET)*, pages 1–6, 2019.

[92] Patrick Juvet Gnetchejo, Salomé Ndjakomo Essiane, Pierre Ele, René Wamkeue, Daniel Mbadjoun Wapet, and Steve Perabi Ngoffe. Important notes on parameter estimation of solar photovoltaic cell. *Energy Conversion and Management*, 197:111870, 2019.

[93] Fahmi F. Muhammad, Ali W. Karim Sangawi, Suhairul Hashim, S. K. Ghoshal, Isam K. Abdullah, and Shilan S. Hameed. Simple and efficient estimation of photovoltaic cells and modules parameters using approximation and correction technique. *PLOS ONE*, 14(5):1–19, 05 2019.

[94] Marcelo Gradella Villalva, Jonas Rafael Gazoli, and Ernesto Ruppert Filho. Comprehensive approach to modeling and simulation of photovoltaic arrays. *IEEE Transactions on power electronics*, 24(5):1198–1208, 2009.

[95] Xiaochao Fan, Hexu Sun, Zhi Yuan, Zheng Li, Ruijing Shi, and Noradin Ghadimi. High voltage gain dc/dc converter using coupled inductor and vm techniques. *IEEE Access*, 8:131975–131987, 2020.

[96] Saleh Mobayen, Farhad Bayat, Chun-Chi Lai, Asghar Taheri, and Afef Fekih. Adaptive global sliding mode controller design for perturbed dc-dc buck converters. *Energies*, 14(5), 2021.

[97] Qun Qi, Davood Ghaderi, and Josep M. Guerrero. Sliding mode controller-based switched-capacitor-based high dc gain and low voltage stress dc-dc boost converter for photovoltaic applications. *International Journal of Electrical Power & Energy Systems*, 125:106496, 2021.

[98] R. Reshma Gopi and S. Sreejith. Converter topologies in photovoltaic applications – a review. *Renewable and Sustainable Energy Reviews*, 94:1–14, 2018.

[99] Samir Abdelmalek, Ali Dali, Azzeddine Bakdi, and Maamar Bettayeb. Design and experimental implementation of a new robust observer-based nonlinear controller for dc-dc buck converters. *Energy*, 213:118816, 2020.

[100] M.Z. Hossain, N.A. Rahim, and Jeyraj a/l Selvaraj. Recent progress and development on power dc-dc converter topology, control, design and applications: A review. *Renewable and Sustainable Energy Reviews*, 81:205–230, 2018.

[101] Asim Amir, Aamir Amir, Hang Seng Che, Ahmad Elkhateb, and Nasrudin Abd Rahim. Comparative analysis of high voltage gain dc-dc converter topologies for photovoltaic systems. *Renewable Energy*, 136:1147–1163, 2019.

[102] S. Morteza Ghamari, Hasan Mollaee, and Fatemeh Khavari. Robust self-tuning regressive adaptive controller design for a dc–dc buck converter. *Measurement*, 174:109071, 2021.

[103] Jaw-Kuen Shiau, Min-Yi Lee, Yu-Chen Wei, and Bo-Chih Chen. Circuit simulation for solar power maximum power point tracking with different buck-boost converter topologies. *Energies*, 7(8):5027–5046, 2014.

[104] J. Prasanth Ram, Himanshu Manghani, Dhanup S. Pillai, T. Sudhakar Babu, Masafumi Miyatake, and N. Rajasekar. Analysis on solar pv emulators: A review. *Renewable and Sustainable Energy Reviews*, 81:149–160, 2018.

[105] Pandav Kiran Maroti, Rashid Al-Ammari, Mahajan Sagar Bhaskar, Mohammad Meraj, Atif Iqbal, Sanjeevikumar Padmanaban, and Syed Rahman. New tri-switching state non-isolated high gain dc–dc boost converter for microgrid application. *IET Power Electronics*, 12(11):2741–2750, 2019.

[106] Mohammad Zaid, Shahrukh Khan, Marif Daula Siddique, Adil Sarwar, Javed Ahmad, Zeeshan Sarwer, and Atif Iqbal. A transformerless high gain dc–dc boost converter with reduced voltage stress. *International Transactions on Electrical Energy Systems*, 31(5):e12877, 2021.

[107] Geetanjali Singh and Sudip Kundu. An efficient dc-dc boost converter for thermoelectric energy harvesting. *AEU - International Journal of Electronics and Communications*, 118:153132, 2020.

[108] Tarakanath Kobaku, R. Jeyasenthil, Subham Sahoo, Rijil Ramchand, and Tomislav Dragicevic. Quantitative feedback design-based robust pid control of voltage mode controlled dc-dc boost converter. *IEEE Transactions on Circuits and Systems II: Express Briefs*, 68(1):286–290, 2021.

[109] Saif Ahmad and Ahmad Ali. Active disturbance rejection control of dc–dc boost converter: a review with modifications for improved performance. *IET Power Electronics*, 12(8):2095–2107, 2019.

[110] V. Duindam, A. Macchelli, S. Stramigioli, and H. Bruyninckx. *Modeling and Control of Complex Physical Systems: The Port-Hamiltonian Approach*. Springer, Berlin, Germany, 2009.

[111] A.J. van der Schaft. *L_2-Gain and Passivity Techniques in Nonlinear Control*. Springer, London, UK, 2000.

[112] Arjan van der Schaft and Dimitri Jeltsema. Port-hamiltonian systems theory: An introductory overview. *Found. Trends Syst. Control*, 1(2–3):173–378, June 2014.

[113] Romeo Ortega and Mark W. Spong. Adaptive motion control of rigid robots: A tutorial. *Automatica*, 25(6):877–888, 1989.

[114] Romeo Ortega, A Loria, Per Johan Nicklasson, and H Sira-Ramirez. Passivity–based control of euler–lagrange systems, communications and control engineering. *Berlin, Germany: Spring-Verlag*, 1998.

[115] Romeo Ortega, Arjan van der Schaft, Bernhard Maschke, and Gerardo Escobar. Interconnection and damping assignment passivity-based control of port-controlled hamiltonian systems. *Automatica*, 38(4):585 – 596, 2002.

[116] D.A. Dirksz, J.M.A. Scherpen, and R. Ortega. Interconnection and damping assignment passivity-based control for port-hamiltonian mechanical systems with only position measurements. In *2008 47th IEEE Conference on Decision and Control*, pages 4957–4962, 2008.

[117] Romeo Ortega, Arjan J Van Der Schaft, Iven Mareels, and Bernhard Maschke. Putting energy back in control. *IEEE Control Systems Magazine*, 21(2):18–33, 2001.

[118] Romeo Ortega and EloÃsa GarcÃa-Canseco. Interconnection and damping assignment passivity-based control: A survey. *European Journal of Control*, 10(5):432 – 450, 2004.

[119] Meng Zhang, Romeo Ortega, Zhitao Liu, and Hongye Su. A new family of interconnection and damping assignment passivity-based controllers. *International Journal of Robust and Nonlinear Control*, 27(1):50–65, 2017.

[120] Tao Ma, Hongxing Yang, Lin Lu, and Jinqing Peng. Technical feasibility study on a standalone hybrid solar-wind system with pumped hydro storage for a remote island in Hong Kong. *Renewable energy*, 69:7–15, 2014.

[121] Hayden Phillips-Brenes, Roberto Pereira-Arroyo, and Mauricio Muñoz-Arias. Energy-based model of a solar-powered pumped-hydro storage system. In *2019 IEEE 39th Central America and Panama Convention (CONCAPAN XXXIX)*, pages 1–6, 2019.

[122] C Bueno and Jose A Carta. Wind powered pumped hydro storage systems, a means of increasing the penetration of renewable energy in the Canary Islands. *Renewable and sustainable energy reviews*, 10(4):312–340, 2006.

[123] Oliver Paish. Small hydro power: technology and current status. *Renewable and sustainable energy reviews*, 6(6):537–556, 2002.

[124] Benfei Wang, Venkata Ravi Kishore Kanamarlapudi, Liang Xian, Xiaoyang Peng, Kuan Tak Tan, and Ping Lam So. Model predictive voltage control for single-inductor multiple-output DC–DC converter with reduced cross regulation. *IEEE Transactions on Industrial Electronics*, 63(7):4187–4197, 2016.

[125] SURANA. *Photovoltaic module SLV-175 datasheet*. SURANA.

[126] Efstratios I. Batzelis and Stavros A. Papathanassiou. A method for the analytical extraction of the single-diode pv model parameters. *IEEE Transactions on Sustainable Energy*, 7(2):504–512, 2016.

[127] KAG Kählig Antriebstechnik GmbH. *DC-Motor M48x60/I datasheet*. KAG Kählig Antriebstechnik GmbH.

[128] MARS ROCK. *Water pump RD9024 datasheet*. MARS ROCK.

[129] Padmanaban Sanjeevikumar, Gabriele Grandi, Patrick W Wheeler, Frede Blaabjerg, and Jelena Loncarski. A simple mppt algorithm for novel pv power generation system by high output voltage dc-dc boost converter. In *2015 IEEE 24th International Symposium on Industrial Electronics (ISIE)*, pages 214–220. IEEE, 2015.

[130] Rajan Kumar and Bhim Singh. Buck-boost converter fed bldc motor drive for solar pv array based water pumping. In *2014 IEEE International Conference on Power Electronics, Drives and Energy Systems (PEDES)*, pages 1–6. IEEE, 2014.

[131] Gerardo Escobar, Arjan J. van der Schaft, and Romeo Ortega. A hamiltonian viewpoint in the modeling of switching power converters. *Automatica*, 35(3):445 – 452, 1999.

[132] Chen-Chi Chu and Chieh-Li Chen. Robust maximum power point tracking method for photovoltaic cells: A sliding mode control approach. *Solar Energy*, 83(8):1370 – 1378, 2009.

[133] A. Kchaou, A. Naamane, Y. Koubaa, and N. M'sirdi. Second order sliding mode-based mppt control for photovoltaic applications. *Solar Energy*, 155:758 – 769, 2017.

[134] ZHIWANG. *Photovoltaic module ZW-7W-6V-1 datasheet*. ZHIWANG.

[135] SPEKTRON. *Irradiation sensor SPEKTRON-210 datasheet*. SPEKTRON.

[136] Benedict R. Gaster, Lee Howes, David R. Kaeli, Perhaad Mistry, and Dana Schaa. *Chapter 3 - OpenCL Device Architectures*. Morgan Kaufmann, Boston, second edition, 2013.

[137] CELLEVIA POWER. *Photovoltaic module CL-SM30M datasheet*. CELLEVIA POWER.

[138] VOLTCRAFT. *Solar light meter PL-110SM datasheet*. VOLTCRAFT.

[139] VICTRON. *Solar charger controller MPPT 75/15 datasheet*. VICTRON.

[140] Kenji Fujimoto and Toshiharu Sugie. Canonical transformation and stabilization of generalized hamiltonian systems. *Systems & Control Letters*, 42(3):217–227, 2001.

[141] Kenji Fujimoto, Kazunori Sakurama, and Toshiharu Sugie. Trajectory tracking control of port-controlled hamiltonian systems via generalized canonical transformations. *Automatica*, 39(12):2059–2069, 2003.

[142] Badur M. Alharbi, Majid A. Alhomim, and Roy A. McCann. An efficient high voltage gain using two-stage cascaded interleaved boost converter for solar pv system with mppt technique. In *2020 IEEE Power & Energy Society Innovative Smart Grid Technologies Conference (ISGT)*, pages 1–4, 2020.

[143] Hussain Attia, Suleyman Ulusoy, and Al Khaimah Ras Al Khaimah. A new perturb and observe mppt algorithm based on two steps variable voltage control. *International Journal of Power Electronics and Drive Systems (IJPEDS)*, 12:2201–2208, 12 2021.

[144] Muhammad Kamran, Muhammad Mudassar, Muhammad Rayyan Fazal, Muhammad Usman Asghar, Muhammad Bilal, and Rohail Asghar. Implementation of improved perturb & observe mppt technique with confined search space for standalone photovoltaic system. *Journal of King Saud University - Engineering Sciences*, 32(7):432–441, 2020. Photovoltaic Materials, Devices and Systems.

[145] Muralidhar Killi and Susovon Samanta. Modified perturb and observe mppt algorithm for drift avoidance in photovoltaic systems. *IEEE Transactions on Industrial Electronics*, 62(9):5549–5559, 2015.

[146] Alivarani Mohapatra, Byamakesh Nayak, and Chidurala Saiprakash. Adaptive perturb & observe mppt for pv system with experimental validation. In *2019 IEEE International Conference on Sustainable Energy Technologies and Systems (ICSETS)*, pages 257–261, 2019.

[147] Gautam A. Raiker, Umanand Loganathan, and Subba Reddy B. Current control of boost converter for pv interface with momentum-based perturb and observe mppt. *IEEE Transactions on Industry Applications*, 57(4):4071–4079, 2021.

[148] Nashwa Ahmad Kamal, Ahmad Taher Azar, Ghada Said Elbasuony, Khaled Mohamad Almustafa, and Dhafer Almakhles. Pso-based adaptive perturb and observe mppt technique for photovoltaic systems. In Aboul Ella Hassanien, Khaled Shaalan, and Mohamed Fahmy Tolba, editors, *Proceedings of the International Conference on Advanced Intelligent Systems and Informatics 2019*, pages 125–135, Cham, 2020. Springer International Publishing.

[149] Niraja Swaminathan, N. Lakshminarasamma, and Yue Cao. A fixed zone perturb and observe mppt technique for a standalone distributed pv system. *IEEE Journal of Emerging and Selected Topics in Power Electronics*, 10(1):361–374, 2022.

[150] Shivendra Singh, Saibal Manna, Mohd Imam Hasan Mansoori, and A.K. Akella. Implementation of perturb & observe mppt technique using boost converter in pv system. In *2020 International Conference on Computational Intelligence for Smart Power System and Sustainable Energy (CISPSSE)*, pages 1–4, 2020.

[151] P. Motsoeneng, J. Bamukunde, and S. Chowdhury. Comparison of perturb & observe and hill climbing mppt schemes for pv plant under cloud cover and varying load. In *2019 10th International Renewable Energy Congress (IREC)*, pages 1–6, 2019.

[152] J K Udavalakshmi and Mohammed S Sheik. Comparative study of perturb & observe and look -up table maximum power point tracking techniques using matlabisimulink. In *2018 International Conference on Current Trends towards Converging Technologies (ICCTCT)*, pages 1–5, 2018.

[153] Chua-Chin Wang, Oliver Lexter July A. Jose, Po-Kai Su, Lean Karlo S. Tolentino, Ralph Gerard B. Sangalang, Jessica S. Velasco, and Tzung-Je Lee. An adaptive constant current and voltage mode p&o-based maximum power point tracking controller ic using 0.5-μm hv cmos. *Microelectronics Journal*, 118:105295, 2021.

[154] Julio López Seguel, S.I Seleme Jr, and Lenin M.F Morais. Comparison of the performance of MPPT methods applied in converters Buck and Buck-Boost for autonomous photovoltaic systems. *Ingeniare. Revista chilena de ingeniería*, 29:229 – 244, 06 2021.

[155] Javad Farzaneh, Reza Keypour, and Mojtaba Ahmadieh Khanesar. A new maximum power point tracking based on modified firefly algorithm for pv system under partial shading conditions. *Technology and Economics of Smart Grids and Sustainable Energy*, 3:9, 2018.

[156] Mohammad Agung Dirmawan, Suhariningsih, and Renny Rakhmawati. The comparison performance of mppt perturb and observe, fuzzy logic controller, and flower pollination algorithm in normal and partial shading condition. In *2020 International Electronics Symposium (IES)*, pages 7–13, 2020.

[157] Suyanto Suyanto, Luthfansyah Mohammad, Iwan Cony Setiadi, and Roekmono Roekmono. Analysis and evaluation performance of mppt algorithms: Perturb & observe (p&o), firefly, and flower pollination (fpa) in smart microgrid solar panel systems. In *2019 International Conference on Technologies and Policies in Electric Power & Energy*, pages 1–6, 2019.

[158] Shraiya Pant and R. P. Saini. Comparative study of mppt techniques for solar photovoltaic system. In *2019 International Conference on Electrical, Electronics and Computer Engineering (UPCON)*, pages 1–6, 2019.

[159] Mahmoud N. Ali, Karar Mahmoud, Matti Lehtonen, and Mohamed M. F. Darwish. An efficient fuzzy-logic based variable-step incremental conductance mppt method for grid-connected pv systems. *IEEE Access*, 9:26420–26430, 2021.

[160] Ankur Kumar Gupta, Rupendra Kumar Pachauri, Tanmoy Maity, Yogesh K. Chauhan, Om Prakash Mahela, Baseem Khan, and Pankaj Kumar Gupta. Effect of various incremental conductance mppt methods on the charging of battery load feed by solar panel. *IEEE Access*, 9:90977–90988, 2021.

[161] Isaac Owusu-Nyarko, Mohamed A. Elgenedy, Ibrahim Abdelsalam, and Khaled H. Ahmed. Modified variable step-size incremental conductance mppt technique for photovoltaic systems. *Electronics*, 10(19), 2021.

[162] GUIZA Dhaouadi, OUNNAS Djamel, SOUFI Youcef, and CHENIKHE Salah. Implementation of incremental conductance based mppt algorithm for photovoltaic system. In *2019 4th International Conference on Power Electronics and their Applications (ICPEA)*, pages 1–5, 2019.

[163] Muhammad Abu Bakar Siddique, Adeel Asad, Rao M. Asif, Ateeq Ur Rehman, Muhammad Tariq Sadiq, and Inam Ullah. Implementation of incremental conductance mppt algorithm with integral regulator by using boost converter in grid-connected pv array. *IETE Journal of Research*, 0(0):1–14, 2021.

[164] Salah Necaibia, Mounia Samira Kelaiaia, Hocine Labar, Ammar Necaibia, and Edgardo D. Castronuovo. Enhanced auto-scaling incremental conductance mppt method, implemented on low-cost microcontroller and sepic converter. *Solar Energy*, 180:152–168, 2019.

[165] Stm Journals, Vishal Chauhan, Shoyab Ali, and Pramod Sharma. Mathematical modelling and design of improved maximum power point tracking system for solar photovoltaic system for renewable energy applications. *Journal of Electronic Design Technology*, 12:2021, 03 2022.

[166] Vibhu Jately, Brian Azzopardi, Jyoti Joshi, Balaji Venkateswaran V, Abhinav Sharma, and Sudha Arora. Experimental analysis of hill-climbing mppt algorithms under low irradiance levels. *Renewable and Sustainable Energy Reviews*, 150:111467, 2021.

[167] Claude Bertin Nzoundja Fapi, Patrice Wira, Martin Kamta, Abderrezak Badji, and Hyacinthe Tchakounte. Real-Time Experimental Assessment of Hill Climbing MPPT Algorithm Enhanced by Estimating a Duty Cycle for PV System. *International Journal of Renewable Energy Research*, June 2019.

[168] Yuhang Liu, Xiangxin Liu, Duofeng Shi, Yufeng Zhang, Qiuchen Wu, Ziyao Zhu, and Xinlu Lin. An mppt approach using improved hill climbing and double closed loop control. In *2019 IEEE 46th Photovoltaic Specialists Conference (PVSC)*, pages 2935–2941, 2019.

[169] Gerardo D. Guerrero-Cabarcas, Rachid Darbali-Zamora, Eduardo I. Ortiz-Rivera, and Jason C. Neely. The integral mean value method approach to obtaining the optimal operating conditions of a photovoltaic system. In *2019 IEEE Power and Energy Conference at Illinois (PECI)*, pages 1–6, 2019.

[170] Rachid Darbali-Zamora, Jimmy E. Quiroz, Javier Hernández-Alvidrez, Jay Johnson, and Eduardo I. Ortiz-Rivera. Viability assessment of a real-time simulation model for a residential dc microgrid network to compensate electricity disturbances in puerto rico. In *2018 IEEE ANDESCON*, pages 1–6, 2018.

[171] Catalina González-Castaño, Leandro L. Lorente-Leyva, Javier Muñoz, Carlos Restrepo, and Diego H. Peluffo-Ordóñez. An mppt strategy based on a surface-based polynomial fitting for solar photovoltaic systems using real-time hardware. *Electronics*, 10(2), 2021.

[172] Zhihong Yan, Ying Huang, Li Wang, Siew-Chong Tan, Chuyang Tang, and S. Y. Ron Hui. Optimization of self-adaptive inr-mppt for r-mode red stacks. In *2022 IEEE Applied Power Electronics Conference and Exposition (APEC)*, pages 1311–1316, 2022.

[173] Zhihong Yan, Ying Huang, Siew-Chong Tan, Chuyang Y. Tang, and Shu Yuen Hui. A self-adaptive-step-size incremental-resistance-mppt technique for reverse-electrodialysis system. *IEEE Transactions on Industrial Electronics*, 70(4):3814–3824, 2023.

[174] Mujahed Aldhaifallah, Abdul-Wahid A. Saif, Uthman Baroudi, Hegazy Rezk, and Ahmed Mohamed. Fractional incremental resistance based mppt for thermoelectric generation systems. In *2021 18th International Multi-Conference on Systems, Signals & Devices (SSD)*, pages 902–907, 2021.

[175] R. Geethamani, C. Pavithra, B. Niranjana, V. Gomathy, and P. Chitra. A noval improved variable step-size incremental resistance maximum power point tracking controller for photo voltaic system under partial shading condition. *Journal of Computational and Theoretical Nanoscience*, 16(2):740–744, 2019.

[176] Xingshuo Li, Huiqing Wen, and Chenhao Zhao. Improved beta parameter based mppt method in photovoltaic system. In *2015 9th International Conference on Power Electronics and ECCE Asia (ICPE-ECCE Asia)*, pages 1405–1412, 2015.

[177] Xingshuo Li, Huiqing Wen, Lin Jiang, Eng Gee Lim, Yang Du, and Chenhao Zhao. Photovoltaic modified β-parameter-based mppt method with fast tracking. *Journal of Power Electronics*, 16:9–17, 1 2016.

[178] Dingyi Lin, Xingshuo Li, Shuye Ding, Huiqing Wen, Yang Du, and Weidong Xiao. Self-tuning mppt scheme based on reinforcement learning and beta parameter in photovoltaic power systems. *IEEE Transactions on Power Electronics*, 36(12):13826–13838, 2021.

[179] Xingshuo Li, Huiqing Wen, Lin Jiang, Weidong Xiao, Yang Du, and Chenhao Zhao. An improved mppt method for pv system with fast-converging speed and zero oscillation. *IEEE Transactions on Industry Applications*, 52(6):5051–5064, 2016.

[180] Xingshuo Li, Huiqing Wen, Lin Jiang, Yihua Hu, and Chenhao Zhao. An improved beta method with autoscaling factor for photovoltaic system. *IEEE Transactions on Industry Applications*, 52(5):4281–4291, 2016.

[181] G. Spiazzi, S. Buso, and P. Mattavelli. Analysis of mppt algorithms for photovoltaic panels based on ripple correlation techniques in presence of parasitic components. In *2009 Brazilian Power Electronics Conference*, pages 88–95, 2009.

[182] Hasan Abed Al Kader Hammoud and Ali M. Bazzi. Model-based mppt with corrective ripple correlation control. In *2020 IEEE Power and Energy Conference at Illinois (PECI)*, pages 1–6, 2020.

[183] Ghias Farivar, Behzad Asaei, and Siamak Mehrnami. An analytical solution for tracking photovoltaic module mpp. *IEEE Journal of Photovoltaics*, 3(3):1053–1061, 2013.

[184] Ghias Farivar, Behzad Asaei, and Mohammad Ali Rezaei. A novel analytical solution for the pv-arrays maximum power point tracking problem. In *2010 IEEE International Conference on Power and Energy*, pages 917–922, 2010.

[185] Ehsan Moshksar and Teymoor Ghanbari. A model-based algorithm for maximum power point tracking of pv systems using exact analytical solution of single-diode equivalent model. *Solar Energy*, 162:117–131, 2018.

[186] Mert Turhan, Baris Dai, and Deniz Yildirim. Analytical mppt solution using thevenin approach for solar panels. In *Eurocon 2013*, pages 803–808, 2013.

[187] Masoud Etezadi Nezhad, Behzad Asaei, and Shahrokh Farhangi. Modified analytical solution for tracking photovoltaic module maximum power point under partial shading condition. In *2013 13th International Conference on Environment and Electrical Engineering (EEEIC)*, pages 182–187, 2013.

[188] S. Malathy and R. Ramaprabha. Maximum power point tracking based on look up table approach. In *Energy Efficient Technologies for Sustainability*, volume 768 of *Advanced Materials Research*, pages 124–130. Trans Tech Publications Ltd, 10 2013.

[189] Vipin Kumar, Sandip Ghosh, N.K. Swami Naidu, Shyam Kamal, R.K. Saket, and S.K. Nagar. Load voltage-based mppt technique for standalone pv systems using adaptive step. *International Journal of Electrical Power & Energy Systems*, 128:106732, 2021.

[190] Seyedkazem Hosseini, Shamsodin Taheri, Masoud Farzaneh, and Hamed Taheri. A high-performance shade-tolerant mppt based on current-mode control. *IEEE Transactions on Power Electronics*, 34(10):10327–10340, 2019.

[191] S.M. Sousa, L.S. Gusman, T.A.S. Lopes, H.A. Pereira, and J.M.S. Callegari. Mppt algorithm in single loop current-mode control applied to dc–dc converters with input current source characteristics. *International Journal of Electrical Power & Energy Systems*, 138:107909, 2022.

[192] David de la Rosa Romo, Rodrigo Loera-Palomo, Michel Rivero, and Francisco S Sellschopp-Sánchez. Averaged current mode control for maximum power point tracking in high-gain photovoltaic applications. *Journal of Power Electronics*, 20:1650–1661, 2020.

[193] Andoni Urtasun, Javier Samanes, Ernesto L. Barrios, Pablo Sanchis, and Luis Marroyo. Control of a photovoltaic array interfacing current-mode-controlled boost converter based on virtual impedance emulation. *IEEE Transactions on Industrial Electronics*, 66(5):3496–3506, 2019.

[194] Amar Kapić, Žarko Zečević, and Božo Krstajić. An efficient mppt algorithm for pv modules under partial shading and sudden change in irradiance. In *2018 23rd International Scientific-Professional Conference on Information Technology (IT)*, pages 1–4, 2018.

[195] M. Vaigundamoorthi, R. Ramesh, V. Vasan Prabhu, and K. Arul Kumar. Mppt oscillations minimization in pv system by controlling non-linear dynamics in sepic dc-dc converter. *International Journal of Electrical and Computer Engineering (IJECE)*, 10:6268–6275, 12 2020.

[196] Matias Carandell, Daniel Mihai Toma, Joaquín del Río, and Manel Gasulla. Optimum mppt strategy for low-power pendulum-type wave energy converters. In *2020 IEEE SENSORS*, pages 1–4, 2020.

[197] Shahrokh Farhangi, Afshin Nazer, Gholam Reza Moradi, and Ehsan Asadi. Improved performance of solar array simulator based on constant voltage/constant current full-bridge converter. In *2020 11th Power Electronics, Drive Systems, and Technologies Conference (PEDSTC)*, pages 1–5, 2020.

[198] Mustafa Engin Başoğlu. An approximate short circuit strategy for transient mppt performance of uniformly irradiated photovoltaic modules. *Balkan Journal of Electrical and Computer Engineering*, 7(1):88 – 93, 2019.

[199] Zemin Liu, Yu-Pin Hsu, and Mona Mostafa Hella. A thermal/rf hybrid energy harvesting system with rectifying-combination and improved fractional-ocv mppt method. *IEEE Transactions on Circuits and Systems I: Regular Papers*, 67(10):3352–3363, 2020.

[200] Ali Hmidet, Umashankar Subramaniam, Rajvikram Madurai Elavarasan, Kannadasan Raju, Matias Diaz, Narottam Das, Kashif Mehmood, Alagar Karthick, M Muhibbullah, and Olfa Boubaker. Design of efficient off-grid solar photovoltaic water pumping system based on improved fractional open circuit voltage mppt technique. *International Journal of Photoenergy*, 2021:4925433, 2021.

[201] Eduardo Moreira Vicente, Paula dos Santos Vicente, Robson Luiz Moreno, and Enio Roberto Ribeiro. High-efficiency mppt method based on irradiance and temperature measurements. *IET Renewable Power Generation*, 14(6):986–995, 2020.

[202] Fethi Messaoudi, Fethi Farhani, and Abderrahmen Zaafouri. Overview and comparatif of maximum power point tracking methods of pv power system. In *2021 IEEE 2nd International Conference on Signal, Control and Communication (SCC)*, pages 119–125, 2021.

[203] Hwa-Dong Liu and Shiue-Der Lu. A high-performance mppt algorithm combining advanced three-point weight comparison and temporary stopped running strategy for pv systems. *IEICE Electronics Express*, 16(18):20190461–20190461, 2019.

[204] Ru-Min Chao, Shih-Hung Ko, Hung-Ku Lin, and I-Kai Wang. Evaluation of a distributed photovoltaic system in grid-connected and standalone applications by different mppt algorithms. *Energies*, 11(6), 2018.

[205] Karima Amara, Toufik Bakir, Ali Malek, Dalila Hocine, El bay Bourennane, Arezki Fekik, and Mustapha Zaouia. An optimized steepest gradient based maximum power point tracking for pv control systems. *International Journal on Electrical Engineering and Informatics*, 11:662–683, 12 2019. Copyright - © 2019. This work is published under https://creativecommons.org/licenses/by-nd/4.0 (the "License"). Notwithstanding the ProQuest Terms and Conditions, you may use this content in accordance with the terms of the License. Última actualización - 2020-01-28.

[206] Abbes Kihal, Fateh Krim, Abdelbaset Laib, Billel Talbi, and Hamza Afghoul. An improved mppt scheme employing adaptive integral derivative sliding mode control for photovoltaic systems under fast irradiation changes. *ISA Transactions*, 87:297–306, 2019.

[207] R. Ortega, J.A.L. Perez, P.J. Nicklasson, and H.J. Sira-Ramirez. *Passivity-based Control of Euler-Lagrange Systems: Mechanical, Electrical and Electromechanical Applications*. Communications and Control Engineering. Springer London, 2013.

[208] Abdelyazid Achour, Djamila Rekioua, Ahmed Mohammedi, Zahra Mokrani, Toufik Rekioua, and Seddik Bacha. Application of direct torque control to a photovoltaic pumping system with sliding-mode control optimization. *Electric Power Components and Systems*, 44(2):172–184, 2016.

[209] Sabir Ouchen, Sabrina Abdeddaim, Achour Betka, and Abdelkrim Menadi. Experimental validation of sliding mode-predictive direct power control of a grid connected photovoltaic system, feeding a nonlinear load. *Solar Energy*, 137:328 – 336, 2016.

[210] Nasrin Chatrenour, Hadi Razmi, and Hasan Doagou-Mojarrad. Improved double integral sliding mode mppt controller based parameter estimation for a stand-alone photovoltaic system. *Energy Conversion and Management*, 139:97–109, 2017.

[211] Bin Guo, Mei Su, Yao Sun, Hui Wang, Bin Liu, Xin Zhang, Josep Pou, Yongheng Yang, and Pooya Davari. Optimization design and control of single-stage single-phase pv inverters for mppt improvement. *IEEE Transactions on Power Electronics*, 35(12):13000–13016, 2020.

[212] Nidhal Khefifi, Azeddine Houari, Mohamed Machmoum, and Malek Ghanes. Interconnection and damping assignment passivity for the control of pv/battery hybrid power source in islanded microgrid. *International Journal of Renewable Energy Research (IJRER)*, 9(4):1790–1802, 2019.

[213] Rafaela Dizaró Silveira, Gabriel Pereira das Neves, Sérgio Augusto Oliveira da Silva, and Bruno Augusto Angélico. An enhanced mppt algorithm based on adaptive extremum-seeking control applied to photovoltaic systems operating under partial shading. *IET Renewable Power Generation*, 15(6):1227–1239, 2021.

[214] Ehsan Moshksar, Teymoor Ghanbari, Haidar Samet, and Martin Guay. Estimation-based extremum-seeking control: A real-time approach for improving energy efficiency in photovoltaic systems. *IEEE Systems Journal*, 13(3):3141–3152, 2019.

[215] Jayanta Kumar Sahu, Saroj Kumar Mishra, and Jyoti Prasad Patra. Mppt extremum seeking control algorithm for standalone pv system. In *2023 5th International Conference on Smart Systems and Inventive Technology (ICSSIT)*, pages 156–160, 2023.

[216] Carlos Restrepo, Catalina González-Castaño, Javier Muñoz, Andrii Chub, Enric Vidal-Idiarte, and Roberto Giral. An mppt algorithm for pv systems based on a simplified photo-diode model. *IEEE Access*, 9:33189–33202, 2021.

[217] Siddhartha Behera, Manoj Kumar Sahu, Twinkle Hazra, Rabindra Behera, Sunila Kumar Swain, Itishree Sahu, Sritam Parida, and Sarat Kumar Swain. Computation of maximum power point tracking of pv module using modified newton raphson technique. *International Journal of Power Electronics and Drive Systems*, 13:2478–2487, 12 2022. Copyright - Copyright IAES Institute of Advanced Engineering and Science 2022 Última actualización - 2023-02-01.

[218] Chinmay Das and Kuntal Mandal. Design and analysis of digitally controlled algorithm-in-loop newton-raphson method based pv emulator. In *2021 Innovations in Energy Management and Renewable Resources(52042)*, pages 1–6, 2021.

[219] Anusha Kumaresan, Hossein Dehghani Tafti, Nandha Kumar Kandasamy, Glen G. Farivar, Josep Pou, and Thangavel Subbaiyan. Flexible power point tracking for solar photovoltaic systems using secant method. *IEEE Transactions on Power Electronics*, 36(8):9419–9429, 2021.

[220] Anusha Kumaresan, Hossein DehghaniTafti, GlenG. Farivar, NandhaKumar Kandasamy, and Josep Pou. Secant-based flexible power point tracking algorithm for degraded photovoltaic systems. In *2021 IEEE Energy Conversion Congress and Exposition (ECCE)*, pages 925–930, 2021.

[221] Binhui Hu and Jianhua Wang. Research on flexible power limiting strategy of pv power generation system based on secant method. In *2022 4th International Conference on Electrical Engineering and Control Technologies (CEECT)*, pages 1137–1142, 2022.

[222] Cheng-Yu Tang, Hsueh-Ju Wu, Chun-Yen Liao, and Hsiu-Hsien Wu. An optimal frequency-modulated hybrid mppt algorithm for the llc resonant converter in pv power applications. *IEEE Transactions on Power Electronics*, 37(1):944–954, 2022.

[223] Nasrudin Abd Rahim, Aamir Amir, Asim Amir, and Jeyraj Selvaraj. Application of bisection search method for maximum power extraction. In *2018 International Conference on Intelligent and Advanced System (ICIAS)*, pages 1–4, 2018.

[224] Fahmi F. Muhammadsharif, Suhairul Hashim, Shilan S. Hameed, S.K. Ghoshal, Isam K. Abdullah, J.E. Macdonald, and Mohd Y. Yahya. Brent's algorithm based new computational approach for accurate determination of single-diode model parameters to simulate solar cells and modules. *Solar Energy*, 193:782–798, 2019.

[225] César G. Villegas-Mier, Juvenal Rodriguez-Resendiz, José M. Álvarez Alvarado, Hugo Rodriguez-Resendiz, Ana Marcela Herrera-Navarro, and Omar Rodríguez-Abreo. Artificial neural networks in mppt algorithms for optimization of photovoltaic power systems: A review. *Micromachines*, 12(10), 2021.

[226] Jenica Ileana Corcau and Liviu Dinca. Modeling and analysis of a fuzzy type mppt algorithm. In *2019 International Conference on Electrical Drives & Power Electronics (EDPE)*, pages 230–234, 2019.

[227] Mahmud Zain Abdullah, Indhana Sudiharto, and Rachma Prilian Eviningsih. Photovoltaic system mppt using fuzzy logic controller. In *2020 International Seminar on Application for Technology of Information and Communication (iSemantic)*, pages 378–383, 2020.

[228] Unal Yilmaz, Ali Kircay, and Selim Borekci. Pv system fuzzy logic mppt method and pi control as a charge controller. *Renewable and Sustainable Energy Reviews*, 81:994–1001, 2018.

[229] Parth Malhotra, Prabhav Kumar Yadav, Samyak Jain, and Dheeraj Joshi. Comparison of p&o and proposed fuzzy logic algorithm for mppt-based charger. In Ranganath M. Singari, Prashant Kumar Jain, and Harish Kumar, editors, *Advances in Manufacturing Technology and Management*, pages 225–235, Singapore, 2023. Springer Nature Singapore.

[230] Ayman Youssef, Mohammed El Telbany, and Abdelhalim Zekry. Reconfigurable generic fpga implementation of fuzzy logic controller for mppt of pv systems. *Renewable and Sustainable Energy Reviews*, 82:1313–1319, 2018.

[231] Mahmoud N. Ali, Karar Mahmoud, Matti Lehtonen, and Mohamed M. F. Darwish. Promising mppt methods combining metaheuristic, fuzzy-logic and ann techniques for grid-connected photovoltaic. *Sensors*, 21(4), 2021.

[232] Hegazy Rezk, Mokhtar Aly, Mujahed Al-Dhaifallah, and Masahito Shoyama. Design and hardware implementation of new adaptive fuzzy logic-based mppt control method for photovoltaic applications. *IEEE Access*, 7:106427–106438, 2019.

[233] Mhamed Fannakh, Mohamed Larbi Elhafyani, and Smail Zouggar. Hardware implementation of the fuzzy logic mppt in an arduino card using a simulink support package for pv application. *IET Renewable Power Generation*, 13(3):510–518, 2019.

[234] Khalid Nasser, Salam Yaqoob, and Zainab Hassoun. Improved dynamic performance of photovoltaic panel using fuzzy logic-mppt algorithm. *Indonesian Journal of Electrical Engineering and Computer Science*, 21, 02 2021.

[235] Kunal Sandip Garud, Simon Jayaraj, and Moo-Yeon Lee. A review on modeling of solar photovoltaic systems using artificial neural networks, fuzzy logic, genetic algorithm and hybrid models. *International Journal of Energy Research*, 45(1):6–35, 2021.

[236] Žarko Zečević and Maja Rolevski. Neural network approach to mppt control and irradiance estimation. *Applied Sciences*, 10(15), 2020.

[237] Saroj Kumar Mishra, Debidatta Mohanty, Jayanta Kumar Sahu, and Shuvankar Mohanty. Artificial neural network based mppt controller for stand-alone solar pv system. In *2021 International Conference on System, Computation, Automation and Networking (ICSCAN)*, pages 1–6, 2021.

[238] Lakshmi P.N Jyothy and M R Sindhu. An artificial neural network based mppt algorithm for solar pv system. In *2018 4th International Conference on Electrical Energy Systems (ICEES)*, pages 375–380, 2018.

[239] Mahmoud Nour Ali. Improved design of artificial neural network for mppt of grid-connected pv systems. In *2018 Twentieth International Middle East Power Systems Conference (MEPCON)*, pages 97–102, 2018.

[240] Adedayo Farayola, Ali Hasan, and Ahmed Ali. Efficient photovoltaic mppt system using coarse gaussian support vector machine and artificial neural network techniques. *International journal of innovative computing, information & control: IJICIC*, 14:323–339, 02 2018.

[241] R. Divyasharon, R. Narmatha Banu, and D. Devaraj. Artificial neural network based mppt with cuk converter topology for pv systems under varying climatic conditions. In *2019 IEEE International Conference on Intelligent Techniques in Control, Optimization and Signal Processing (INCOS)*, pages 1–6, 2019.

[242] Salwa Assahout, Hayat Elaissaoui, Abdelghani El Ougli, Belkassem Tidhaf, and Hafida Zrouri. A neural network and fuzzy logic based mppt algorithm for photovoltaic pumping system. *International Journal of Power Electronics and Drive Systems (IJPEDS)*, 9:1823–1833, 12 2018.

[243] Rajib Baran Roy, Md. Rokonuzzaman, Nowshad Amin, Mahmuda Khatun Mishu, Sanath Alahakoon, Saifur Rahman, Nadarajah Mithulananthan, Kazi Sajedur Rahman, Mohammad Shakeri, and Jagadeesh Pasupuleti. A comparative performance analysis of ann algorithms for mppt energy harvesting in solar pv system. *IEEE Access*, 9:102137–102152, 2021.

[244] Shoeb Azam Farooqui, Rashid Ahmed Khan, Noorul Islam, and Naeem Ahmed. Cuckoo search algorithm and artificial neural network-based mppt: A comparative analysis. In *2021 IEEE 8th Uttar Pradesh Section International Conference on Electrical, Electronics and Computer Engineering (UPCON)*, pages 1–5, 2021.

[245] Zarko Zečević and Maja Rolevski. Neural network approach to mppt control and irradiance estimation. *Applied Sciences*, 10(15), 2020.

[246] Ammar A. Aldair, Adel A. Obed, and Ali F. Halihal. Design and implementation of anfis-reference model controller based mppt using fpga for photovoltaic system. *Renewable and Sustainable Energy Reviews*, 82:2202–2217, 2018.

[247] Karima Amara, Arezki Fekik, D. Hocine, Mohamed Lamine Bakir, El-Bay Bourennane, Toufik Ali Malek, and Ali Malek. Improved performance of a pv solar panel with adaptive neuro fuzzy inference system anfis based mppt. In *2018 7th International Conference on Renewable Energy Research and Applications (ICRERA)*, pages 1098–1101, 2018.

[248] S R Revathy, V Kirubakaran, M Rajeshwaran, T Balasundaram, V S Chandra Sekar, Saad Alghamdi, Bodour S Rajab, Ahmad O Babalghith, and Endalkachew Mergia Anbese. Design and analysis of anfis – based mppt method for solar photovoltaic applications. *International Journal of Photoenergy*, 2022:9625564, 2022.

[249] Ranganai T. Moyo, Pavel Y. Tabakov, and Sibusiso Moyo. Design and Modeling of the ANFIS-Based MPPT Controller for a Solar Photovoltaic System. *Journal of Solar Energy Engineering*, 143(4), 11 2020. 041002.

[250] Muhammad Rameez Javed, Aashir Waleed, Umar Siddique Virk, and Syed Zain ul Hassan. Comparison of the adaptive neural-fuzzy interface system (anfis) based solar maximum power point tracking (mppt) with other solar mppt methods. In *2020 IEEE 23rd International Multitopic Conference (INMIC)*, pages 1–5, 2020.

[251] S. Shabaan, Mohamed I. Abu El-Sebah, and Pierre Bekhit. Maximum power point tracking for photovoltaic solar pump based on anfis tuning system. *Journal of Electrical Systems and Information Technology*, 5(1):11–22, 2018.

[252] Saba Javed and Kashif Ishaque. A comprehensive analyses with new findings of different pso variants for mppt problem under partial shading. *Ain Shams Engineering Journal*, 13(5):101680, 2022.

[253] Hegazy Rezk, Abeer Mera, and Mohamed A. Tolba. Performance analysis of solar pv system under shading condition. In *2020 International Youth Conference on Radio Electronics, Electrical and Power Engineering (REEPE)*, pages 1–5, 2020.

[254] Aman Nusaif and Anas Lateef. Mppt algorithms (pso, fa, and mfa) for pv system under partial shading condition, case study: Bts in algazalia, baghdad. *International Journal of Smart Grid*, 4:100 – 110, 09 2020.

[255] Farag K. Abo-Elyousr, Alaaeldin M. Abdelshafy, and Almoataz Y. Abdelaziz. *MPPT-Based Particle Swarm and Cuckoo Search Algorithms for PV Systems*, pages 379–400. Springer International Publishing, Cham, 2020.

[256] Vahid Moradzadeh Tehrani, Amirhossein Rajaei, and Mohammad Ali Loghavi. Mppt controller design using tlbo algorithm for photovoltaic systems under partial shading conditions. In *2021 12th Power Electronics, Drive Systems, and Technologies Conference (PEDSTC)*, pages 1–5, 2021.

[257] Manel Merchaoui, Anis Sakly, and Mohamed Faouzi Mimouni. Improved fast particle swarm optimization based pv mppt. In *2018 9th International Renewable Energy Congress (IREC)*, pages 1–7, 2018.

[258] A P Yoganandini and G S Anitha. A modified particle swarm optimization algorithm to enhance mppt in the pv array. *International Journal of Electrical and Computer Engineering*, 10:5001–5008, 10 2020. Copyright - Copyright IAES Institute of Advanced Engineering and Science Oct 2020 Última actualización - 2020-07-01.

[259] Libin Xu, Ruofa Cheng, Zhen Xia, and Ziliang Shen. Improved particle swarm optimization (pso)-based mppt method for pv string under partially shading and uniform irradiance condition. In *2020 Asia Energy and Electrical Engineering Symposium (AEEES)*, pages 771–775, 2020.

[260] Ali M. Eltamaly, M.S. Al-Saud, Ahmed G. Abokhalil, and Hassan M.H. Farh. Simulation and experimental validation of fast adaptive particle swarm optimization strategy for photovoltaic global peak tracker under dynamic partial shading. *Renewable and Sustainable Energy Reviews*, 124:109719, 2020.

[261] Prisma Megantoro, Hafidz Faqih Aldi Kusuma, Lilik Jamilatul Awalin, Yusrizal Afif, Dimas Febriyan Priambodo, and Pandi Vigneshwaran. Comparative analysis of evolutionary-based maximum power point tracking for partial shaded photovoltaic. *International Journal of Electrical and Computer Engineering*, 12:5717–5729, 12 2022. Copyright - Copyright IAES Institute of Advanced Engineering and Science 2022 Última actualización - 2023-01-19.

[262] Prisma Megantoro, Yabes Dwi Nugroho, Fajar Anggara, Aji Pakha, and Brahmantya Aji Pramudita. The implementation of genetic algorithm to mppt technique in a dc/dc buck converter under partial shading condition. In *2018 3rd International Conference on Information Technology, Information System and Electrical Engineering (ICITISEE)*, pages 308–312, 2018.

[263] Prisma Megantoro, Yabes Dwi Nugroho, Fajar Anggara, Suhono, and Emmy Yuniarti Rusadi. Simulation and characterization of genetic algorithm implemented on mppt for pv system under partial shading condition. In *2018 3rd International Conference on Information Technology, Information System and Electrical Engineering (ICITISEE)*, pages 74–78, 2018.

[264] Xuan Yang, Weide Li, Lili Su, Yaling Wang, and Ailing Yang. An improved evolution fruit fly optimization algorithm and its application. *Neural Computing and Applications*, 32:9897–9914, 2020.

[265] Yu-Pei Huang, Ming-Yi Huang, and Cheng-En Ye. A fusion firefly algorithm with simplified propagation for photovoltaic mppt under partial shading conditions. *IEEE Transactions on Sustainable Energy*, 11(4):2641–2652, 2020.

[266] MADHUSMITA MOHANTY, SANKAR SELVAKUMAR, CHANDRASEKARAN KOODALSAMY, and SISHAJ PULIKOTTIL SIMON. Global maximum operating point tracking for pv system using fast convergence firefly algorithm. *Turkish Journal of Electrical Engineering and Computer Sciences*, 27:4640–4658, 1 2019.

[267] L N Palupi, T Winarno, A Pracoyo, and L Ardhenta. Adaptive voltage control for mppt-firefly algorithm output in pv system. *IOP Conference Series: Materials Science and Engineering*, 732(1):012048, jan 2020.

[268] Rodrigo Bairros Watanabe, Oswaldo Hideo Ando Junior, Paulo Gabriel Martins Leandro, Fabiano Salvadori, Marlon Felipe Beck, Katiane Pereira, Marcelo Henrique Manzque Brandt, and Fernando Marcos de Oliveira. Implementation of the bio-inspired metaheuristic firefly algorithm (fa) applied to maximum power point tracking of photovoltaic systems. *Energies*, 15(15), 2022.

[269] CH Hussaian Basha, Viraj Bansal, C. Rani, R. M. Brisilla, and S. Odofin. Development of cuckoo search mppt algorithm for partially shaded solar pv sepic converter. In Kedar Nath Das, Jagdish Chand Bansal, Kusum Deep, Atulya K. Nagar, Ponnambalam Pathipooranam, and Rani Chinnappa Naidu, editors, *Soft Computing for Problem Solving*, pages 727–736, Singapore, 2020. Springer Singapore.

[270] Mohamed I. Mosaad, M. Osama abed el-Raouf, Mahmoud A. Al-Ahmar, and Fahd A. Banakher. Maximum power point tracking of pv system based cuckoo search algorithm; review and comparison. *Energy Procedia*, 162:117–126, 2019. Emerging and Renewable Energy: Generation and Automation.

[271] Ali M. Eltamaly. An improved cuckoo search algorithm for maximum power point tracking of photovoltaic systems under partial shading conditions. *Energies*, 14(4), 2021.

[272] A Radhika, G Soundradevi, and R Mohan Kumar. An effective compensation of power quality issues using mppt-based cuckoo search optimization approach. *Soft Computing*, 24:16719–16725, 2020.

[273] Ahmed Fathy, Ibrahim Ziedan, and Dina Amer. Improved teaching–learning-based optimization algorithm-based maximum power point trackers for photovoltaic system. *Electrical Engineering*, 100:1773–1784, 2018.

[274] T. Nagadurga, P. V. R. L. Narasimham, and V. S. Vakula. Global maximum power point tracking of solar pv strings using the teaching learning based optimisation technique. *International Journal of Ambient Energy*, 43(1):1883–1894, 2022.

[275] Kenia Yadira Gómez Díaz, Susana Estefany De León Aldaco, Jesus Aguayo Alquicira, Mario Ponce-Silva, and Víctor Hugo Olivares Peregrino. Teaching–learning-based optimization algorithm applied in electronic engineering: A survey. *Electronics*, 11(21), 2022.

[276] Ke Guo, Lichuang Cui, Mingxuan Mao, Lin Zhou, and Qianjin Zhang. An improved gray wolf optimizer mppt algorithm for pv system with bfbic converter under partial shading. *IEEE Access*, 8:103476–103490, 2020.

[277] A. Darcy Gnana Jegha, M. S. P. Subathra, Nallapaneni Manoj Kumar, Umashankar Subramaniam, and Sanjeevikumar Padmanaban. A high gain dc-dc converter with grey

wolf optimizer based mppt algorithm for pv fed bldc motor drive. *Applied Sciences*, 10(8), 2020.

[278] Zemmit Abderrahim, Kameleddine Heraguemi, and Messalti Sabir. A new improved variable step size mppt method for photovoltaic systems using grey wolf and whale optimization technique based pid controller. *Journal Européen des Systèmes Automatisés*, 54:175–185, 02 2021.

[279] Saad Motahhir, Smail Chtita, Aissa Chouder, and Aboubakr El Hammoumi. Enhanced energy output from a pv system under partial shaded conditions through grey wolf optimizer. *Cleaner Engineering and Technology*, 9:100533, 2022.

[280] D Suhardi, L Syafaah, M Irfan, M Yusuf, M Effendy, and I Pakaya. Improvement of maximum power point tracking (mppt) efficiency using grey wolf optimization (gwo) algorithm in photovoltaic (pv) system. *IOP Conference Series: Materials Science and Engineering*, 674(1):012038, nov 2019.

[281] Satheesh Krishnan G, Sundareswaran Kinattingal, Sishaj P Simon, and Panugothu Srinivasa Rao Nayak. Mppt in pv systems using ant colony optimisation with dwindling population. *IET Renewable Power Generation*, 14(7):1105–1112, 2020.

[282] Neeraj Priyadarshi, Vigna K. Ramachandaramurthy, Sanjeevikumar Padmanaban, and Farooque Azam. An ant colony optimized mppt for standalone hybrid pv-wind power system with single cuk converter. *Energies*, 12(1), 2019.

[283] Rakesh Kumar Phanden, Lalit Sharma, Jatinder Chhabra, and Halil İbrahim Demir. A novel modified ant colony optimization based maximum power point tracking controller for photovoltaic systems. *Materials Today: Proceedings*, 38:89–93, 2021. 2nd International Conference on Future Learning Aspects of Mechanical Engineering.

[284] Marwa Hannachi, Omessaad Elbeji, Mouna Benhamed, and Lassaad Sbita. Comparison between abc and aco: Tunning of on-off mppt for wind systems. *Wind Engineering*, 45(6):1601–1612, 2021.

[285] Farid Dwi Murdianto, Ainur Rofiq Nansur, Alfis Syah Laili Hermawan, Era Purwanto, Arman Jaya, and Mochammad Machmud Rifadil. Modeling and simulation of mppt sepic - buck converter series using flower pollination algorithm (fpa) - pi controller in dc microgrid isolated system. In *2018 International Electrical Engineering Congress (iEECON)*, pages 1–4, 2018.

[286] Luthfansyah, Mohammad, Suyanto, Suyanto, and Bakarr Momodu Bangura, Abu. Evaluation and comparison of dc-dc power converter variations in solar panel systems using maximum power point tracking (mppt) flower pollination algorithm (fpa) control. *E3S Web Conf.*, 190:00026, 2020.

[287] Dalia Yousri, Thanikanti Sudhakar Babu, Dalia Allam, Vigna K. Ramachandaramurthy, and Magdy B Etiba. A novel chaotic flower pollination algorithm for global maximum power point tracking for photovoltaic system under partial shading conditions. *IEEE Access*, 7:121432–121445, 2019.

[288] Ainur Rofiq Nansur, Farid Dwi Murdianto, and Alfis Syah Laili Hermawan. Improving the performance of mppt coupled inductor sepic converter using flower pollination algorithm (fpa) under partial shading condition. In *2018 International Electronics Symposium on Engineering Technology and Applications (IES-ETA)*, pages 1–7, 2018.

[289] Tingting Pei, Xiaohong Hao, and Qun Gu. A novel global maximum power point tracking strategy based on modified flower pollination algorithm for photovoltaic systems under non-uniform irradiation and temperature conditions. *Energies*, 11(10), 2018.

[290] Cihan Demircan, Ali Keçebaş, and Hilmi Cenk Bayrakçı. *Artificial Bee Colony-Based GMPPT for Non-homogeneous Operating Conditions in a Bifacial CPVT System*, pages 331–353. Springer International Publishing, Cham, 2020.

[291] Mehmet Fatih Tefek. Artificial bee colony algorithm based on a new local search approach for parameter estimation of photovoltaic systems. *Journal of Computational Electronics*, 20:2530–2562, 2021.

[292] Hartono Hartono, Yusraini Muharni, Wahid Diana Tasdik, Alief Maulana, and Irma Saraswati. Solar panel optimization using maximum power point tracking based on artificial bee colony algorithm. *Journal of Systems Engineering and Management*, 1(1):7–14, 2022.

[293] Kok Soon Tey, Saad Mekhilef, Mehdi Seyedmahmoudian, Ben Horan, Amanullah Than Oo, and Alex Stojcevski. Improved differential evolution-based mppt algorithm using sepic for pv systems under partial shading conditions and load variation. *IEEE Transactions on Industrial Informatics*, 14(10):4322–4333, 2018.

[294] Ade Pradana Firmanza, Muhammad Nizar Habibi, Novie Ayub Windarko, and Diah Septi Yanaratri. Differential evolution-based mppt with dual mutation for pv array under partial shading condition. In *2020 10th Electrical Power, Electronics, Communications, Controls and Informatics Seminar (EECCIS)*, pages 198–203, 2020.

[295] Peng Zhang and Huibin Sui. Maximum power point tracking technology of photovoltaic array under partial shading based on adaptive improved differential evolution algorithm. *Energies*, 13(5), 2020.

[296] Nurul Izyan Kamaruddin, Ahmad Razani Haron, Min Keng Tan, Soo Siang Yang, Hui Hwang Goh, and Kenneth Tze Kin Teo. Adapting perturbation voltage in pv array with power point tracking and differential evolution. In *2019 IEEE 6th International Conference on Engineering Technologies and Applied Sciences (ICETAS)*, pages 1–6, 2019.

[297] Ali M. Eltamaly, M. S. Al-Saud, and Ahmed G. Abokhalil. A novel bat algorithm strategy for maximum power point tracker of photovoltaic energy systems under dynamic partial shading. *IEEE Access*, 8:10048–10060, 2020.

[298] Kok Soon Tey, Saad Mekhilef, and Mehdi Seyedmahmoudian. Implementation of bat algorithm as maximum power point tracking technique for photovoltaic system under

partial shading conditions. In *2018 IEEE Energy Conversion Congress and Exposition (ECCE)*, pages 2531–2535, 2018.

[299] Mehdi Seyedmahmoudian, Tey Kok Soon, Elmira Jamei, Gokul Sidarth Thirunavukkarasu, Ben Horan, Saad Mekhilef, and Alex Stojcevski. Maximum power point tracking for photovoltaic systems under partial shading conditions using bat algorithm. *Sustainability*, 10(5), 2018.

[300] Zhongqiang Wu and Danqi Yu. Application of improved bat algorithm for solar pv maximum power point tracking under partially shaded condition. *Applied Soft Computing*, 62:101–109, 2018.

[301] Mohammed H. Qais, Hany M. Hasanien, and Saad Alghuwainem. Enhanced whale optimization algorithm for maximum power point tracking of variable-speed wind generators. *Applied Soft Computing*, 86:105937, 2020.

[302] Nadim Rana, Muhammad Shafie Abd Latiff, Shafi'i Muhammad Abdulhamid, and Haruna Chiroma. Whale optimization algorithm: a systematic review of contemporary applications, modifications and developments. *Neural Computing and Applications*, 32:16245–16277, 2020.

[303] D. E. Zabia, H. Afghoul, and O. Kraa. Maximum power point tracking of a photovoltaic system under partial shading condition using whale optimization algorithm. In Mustapha Hatti, editor, *Artificial Intelligence and Heuristics for Smart Energy Efficiency in Smart Cities*, pages 121–132, Cham, 2022. Springer International Publishing.

[304] B. Maniraj and A. Peer Fathima. Pv output power enhancement using whale optimization algorithm under normal and shading conditions. *International Journal of Renewable Energy Research*, 10:1542–1543, 1 2020.

[305] Merna M. Eshak, Mohamed A. Khafagy, Peter Makeen, and Sameh O. Abdellatif. Optimizing the performance of a stand-alone pv system under non-uniform irradiance using gray-wolf and hybrid neural network ai-mppt algorithms. In *2020 2nd Novel Intelligent and Leading Emerging Sciences Conference (NILES)*, pages 600–605, 2020.

[306] Bhukya Laxman, Anil Annamraju, and Nandiraju Venkata Srikanth. A grey wolf optimized fuzzy logic based mppt for shaded solar photovoltaic systems in microgrids. *International Journal of Hydrogen Energy*, 46(18):10653–10665, 2021.

[307] Shahriar Farajdadian and S.M.Hassan Hosseini. Optimization of fuzzy-based mppt controller via metaheuristic techniques for stand-alone pv systems. *International Journal of Hydrogen Energy*, 44(47):25457–25472, 2019.

[308] Jinan Abdulhasan Salim, Baraa M. Albaker, Muwafaq Shyaa Alwan, and M. Hasanuzzaman. Hybrid mppt approach using cuckoo search and grey wolf optimizer for pv systems under variant operating conditions. *Global Energy Interconnection*, 5(6):627–644, 2022.

[309] Dimas Aji Nugraha, K. L. Lian, and Suwarno. A novel mppt method based on cuckoo search algorithm and golden section search algorithm for partially shaded pv system. *Canadian Journal of Electrical and Computer Engineering*, 42(3):173–182, 2019.

[310] S Sheik Mohammed, D Devaraj, and T P Imthias Ahamed. Ga-optimized fuzzy-based mppt technique for abruptly varying environmental conditions. *Journal of The Institution of Engineers (India): Series B*, 102:497–508, 2021.

[311] Aakash Hassan, Octavian Bass, and Mohammad A.S. Masoum. An improved genetic algorithm based fractional open circuit voltage mppt for solar pv systems. *Energy Reports*, 9:1535–1548, 2023.

[312] S H Sheikh Ahmadi, M Karami, M Gholami, and R Mirzaei. Improving mppt performance in pv systems based on integrating the incremental conductance and particle swarm optimization methods. *Iranian Journal of Science and Technology, Transactions of Electrical Engineering*, 46:27–39, 2022.

[313] Badreddine Babes, Amar Boutaghane, and Noureddine Hamouda. A novel nature-inspired maximum power point tracking (mppt) controller based on aco-ann algorithm for photovoltaic (pv) system fed arc welding machines. *Neural Computing and Applications*, 34:299–317, 2022.

[314] Hossam Hassan Ammar, Ahmad Taher Azar, Raafat Shalaby, and M I Mahmoud. Metaheuristic optimization of fractional order incremental conductance (fo-inc) maximum power point tracking (mppt). *Complexity*, 2019:7687891, 2019.

[315] Jun-Ming Huang, Rong-Jong Wai, and Geng-Jie Yang. Design of hybrid artificial bee colony algorithm and semi-supervised extreme learning machine for pv fault diagnoses by considering dust impact. *IEEE Transactions on Power Electronics*, 35(7):7086–7099, 2020.

[316] D.J. Krishna Kishore, M.R. Mohamed, K. Sudhakar, and K. Peddakapu. Swarm intelligence-based mppt design for pv systems under diverse partial shading conditions. *Energy*, 265:126366, 2023.

[317] Deepthi Pilakkat and S. Kanthalakshmi. An improved p&o algorithm integrated with artificial bee colony for photovoltaic systems under partial shading conditions. *Solar Energy*, 178:37–47, 2019.

[318] Majid Abdullateef Abdullah, Tawfik Al-Hadhrami, Chee Wei Tan, and Abdul Halim Yatim. Towards green energy for smart cities: Particle swarm optimization based mppt approach. *IEEE Access*, 6:58427–58438, 2018.

[319] Ziad M. Ali, Thamer Alquthami, Salem Alkhalaf, Hojat Norouzi, Sajjad Dadfar, and Kengo Suzuki. Novel hybrid improved bat algorithm and fuzzy system based mppt for photovoltaic under variable atmospheric conditions. *Sustainable Energy Technologies and Assessments*, 52:102156, 2022.

[320] Hong Li, Duo Yang, Wenzhe Su, Jinhu Lü, and Xinghuo Yu. An overall distribution particle swarm optimization mppt algorithm for photovoltaic system under partial shading. *IEEE Transactions on Industrial Electronics*, 66(1):265–275, 2019.

[321] Dalia Yousri, Thanikanti Sudhakar Babu, Dalia Allam, Vigna. K. Ramachandaramurthy, Eman Beshr, and Magdy. B. Eteiba. Fractional chaos maps with flower pollination algorithm for partial shading mitigation of photovoltaic systems. *Energies*, 12(18), 2019.

[322] J. Prasanth Ram, Dhanup S. Pillai, Amer M.Y.M. Ghias, and N. Rajasekar. Performance enhancement of solar pv systems applying p&o assisted flower pollination algorithm (fpa). *Solar Energy*, 199:214–229, 2020.

[323] Kuei-Hsiang Chao and Muhammad Nursyam Rizal. A hybrid mppt controller based on the genetic algorithm and ant colony optimization for photovoltaic systems under partially shaded conditions. *Energies*, 14(10), 2021.

[324] Samira Ghorbanpour, Mingyu Seo, Jeong-Ju Park, Musu Kim, Yuwei Jin, and Sekyung Han. Unified evolutionary algorithm framework for hybrid power converter. *Applied Sciences*, 12(21), 2022.

[325] Sanjeevikumar Padmanaban, Neeraj Priyadarshi, Mahajan Sagar Bhaskar, Jens Bo Holm-Nielsen, Vigna K. Ramachandaramurthy, and Eklas Hossain. A hybrid anfis-abc based mppt controller for pv system with anti-islanding grid protection: Experimental realization. *IEEE Access*, 7:103377–103389, 2019.

[326] Javad Farzaneh. A hybrid modified fa-anfis-p&o approach for mppt in photovoltaic systems under pscs. *International Journal of Electronics*, 107(5):703–718, 2020.

[327] Ahmed G. Abo-Khalil, Walied Alharbi, Abdel-Rahman Al-Qawasmi, Mohammad Alobaid, and Ibrahim M. Alarifi. Maximum power point tracking of pv systems under partial shading conditions based on opposition-based learning firefly algorithm. *Sustainability*, 13(5), 2021.

[328] Yu-Pei Huang, Xiang Chen, and Cheng-En Ye. A hybrid maximum power point tracking approach for photovoltaic systems under partial shading conditions using a modified genetic algorithm and the firefly algorithm. *International Journal of Photoenergy*, 2018:7598653, 2018.

[329] N. Abd Rahim, A. Amir, and J. Selvaraj. Maximum energy extraction for pv system using closed bracket technique. *IET Conference Proceedings*, pages 52 (5 pp.)–52 (5 pp.)(1), January 2018.

[330] Chih Yu Liao, Ramadhani Kurniawan Subroto, Ibrahim Saiful Millah, Kuo Lung Lian, and Wei-Tzer Huang. An improved bat algorithm for more efficient and faster maximum power point tracking for a photovoltaic system under partial shading conditions. *IEEE Access*, 8:96378–96390, 2020.

[331] Carlos Restrepo, Nicolas Yanẽz Monsalvez, Catalina González-Castaño, Samir Kouro, and Jose Rodriguez. A fast converging hybrid mppt algorithm based on abc and p&o techniques for a partially shaded pv system. *Mathematics*, 9(18), 2021.

[332] Ahmed A. Zaki Diab. *MPPT of PV System Under Partial Shading Conditions Based on Hybrid Whale Optimization-Simulated Annealing Algorithm (WOSA)*, pages 355–378. Springer International Publishing, Cham, 2020.

[333] Hai Tao, Mehrdad Ghahremani, Faraedoon Waly Ahmed, Wang Jing, Muhammad Shahzad Nazir, and Kentaro Ohshima. A novel mppt controller in pv systems with hybrid whale optimization-ps algorithm based anfis under different conditions. *Control Engineering Practice*, 112:104809, 2021.

[334] Sally Sajadian, Reza Ahmadi, and Hassan Zargarzadeh. Extremum seeking-based model predictive mppt for grid-tied z-source inverter for photovoltaic systems. *IEEE Journal of Emerging and Selected Topics in Power Electronics*, 7(1):216–227, 2019.

[335] Seyyed Majid Fatemi, Milad Samady Shadlu, and Amin Talebkhah. A new method for maximum power point tracking in solar pv systems by combining extremum seeking method (esm) and model predictive control (mpc). In *2020 11th Power Electronics, Drive Systems, and Technologies Conference (PEDSTC)*, pages 1–5, 2020.

[336] Mohammad Mohammadinodoushan, Rabeh Abbassi, Houssem Jerbi, Faraedoon Waly Ahmed, Halkawt Abdalqadir kh ahmed, and Alireza Rezvani. A new mppt design using variable step size perturb and observe method for pv system under partially shaded conditions by modified shuffled frog leaping algorithm- smc controller. *Sustainable Energy Technologies and Assessments*, 45:101056, 2021.

[337] Abdallah Aldosary, Ziad M. Ali, Mohammed M. Alhaider, Mehrdad Ghahremani, Sajjad Dadfar, and Kengo Suzuki. A modified shuffled frog algorithm to improve mppt controller in pv system with storage batteries under variable atmospheric conditions. *Control Engineering Practice*, 112:104831, 2021.

[338] Lionnel Mazuba Itetshi, Michel Matalatala Tamasala, and Vital Angelo Kuti Lusala. Combined p&o mppt and cc-cv algorithms for the design of a portable and efficient solar charging system. In *2022 International Conference on Electrical, Computer, Communications and Mechatronics Engineering (ICECCME)*, pages 01–06, 2022.

[339] Hayat Elaissaoui, Mohammed Zerouali, Abdelghani El Ougli, and Belkassem Tidhaf. Mppt algorithm based on fuzzy logic and artificial neural network (ann) for a hybrid solar/wind power generation system. In *2020 Fourth International Conference On Intelligent Computing in Data Sciences (ICDS)*, pages 1–6, 2020.

[340] Milad Fathi and Jafar Amiri Parian. Intelligent mppt for photovoltaic panels using a novel fuzzy logic and artificial neural networks based on evolutionary algorithms. *Energy Reports*, 7:1338–1348, 2021.

[341] Adrian S. T. Tan and S. Iqbal. Implementation of inc mppt and cv charging using llc resonant converter for solar streetlight system. *Journal of Circuits, Systems and Computers*, 27(03):1850043, 2018.

[342] Sadeq D. Al-Majidi, Maysam F. Abbod, and Hamed S. Al-Raweshidy. A modified p&o-mppt based on pythagorean theorem and cv-mppt for pv systems. In *2018 53rd International Universities Power Engineering Conference (UPEC)*, pages 1–6, 2018.

[343] Sanjeevikumar Padmanaban, C. Dhanamjayulu, and Baseem Khan. Artificial neural network and newton raphson (ann-nr) algorithm based selective harmonic elimination in cascaded multilevel inverter for pv applications. *IEEE Access*, 9:75058–75070, 2021.

[344] J. L. Carvalho and L. C. Kretly. Modified newton-raphson method to achieve variable step hill-climbing algorithm for maximum power point tracking. In *2021 IEEE International Conference on Microwaves, Antennas, Communications and Electronic Systems (COMCAS)*, pages 442–447, 2021.

[345] Saber Arabi Nowdeh, Mohammad Jafar Hadidian Moghaddam, Manoochehr Babanezhad, Iraj Faraji Davoodkhani, Akhtar Kalam, Abdollah Ahmadi, and Almoataz Y. Abdelaziz. *A Novel Maximum Power Point Tracking Method for Photovoltaic Application Using Secant Incremental Gradient Based on Newton Raphson*, pages 71–96. Springer Singapore, Singapore, 2019.

[346] Kulu. Amadu. Amalo, Sabo Ibrahim Birninkudu, Bala Boyi Bukata, Ahmed Tijani Salawudeen, and Ashraf Adam Ahmad. Cultured bat algorithm for optimized mppt tracking under different shading conditions. In *2020 International Conference in Mathematics, Computer Engineering and Computer Science (ICMCECS)*, pages 1–8, 2020.

[347] Li Shengqing, Li Fujun, Zheng Jian, Chen Wen, and Zhang Donghui. An improved mppt control strategy based on incremental conductance method. *Soft Computing*, 24:6039–6046, 2020.

[348] Tao Hai, Jincheng Zhou, Ammar K. Alazzawi, and Kengo Muranaka. Modelling and simulation of photovoltaic system using hybrid improved shuffled frog leaping algorithm -fuzzy controller under partial shaded condition. *Simulation Modelling Practice and Theory*, 122:102684, 2023.

[349] Miao Zhang, Keyu Zhuang, Tong Zhao, Jingze Xue, Yunlong Gao, Shuai Cui, and Zheng Qiao. Mppt control algorithm based on particle swarm optimization and adaptive linear active disturbance rejection control. *Energies*, 15(23), 2022.

[350] Lieping Zhang, Zhengzhong Wang, Peng Cao, and Shenglan Zhang. A maximum power point tracking algorithm of load current maximization-perturbation and observation method with variable step size. *Symmetry*, 12(2), 2020.

[351] Ehsan Norouzzadeh, Ahmad Ale Ahmad, Meysam Saeedian, Gholamreza Eini, and Edris Pouresmaeil. Design and implementation of a new algorithm for enhancing mppt performance in solar cells. *Energies*, 12(3), 2019.

[352] Zhen Pan, Nguyen Vu Quynh, Ziad M. Ali, Sajjad Dadfar, and Tetsuya Kashiwagi. Enhancement of maximum power point tracking technique based on pv-battery system using hybrid bat algorithm and fuzzy controller. *Journal of Cleaner Production*, 274:123719, 2020.

[353] Sy Ngo, Chian-Song Chiu, and Phuong-Tra Nguyen. Mppt design using the hybrid method for the pv system under partial shading conditions. In Raghvendra Kumar, Nguyen Ho Quang, Vijender Kumar Solanki, Manuel Cardona, and Prasant Kumar Pattnaik, editors, *Research in Intelligent and Computing in Engineering*, pages 77–87, Singapore, 2021. Springer Singapore.

[354] Mohammed Salah Bouakkaz, Ahcen Boukadoum, Omar Boudebbouz, Issam Attoui, Nadir Boutasseta, and Ahmed Bouraiou. Fuzzy logic based adaptive step hill climbing mppt algorithm for pv energy generation systems. In *2020 International Conference on Computing and Information Technology (ICCIT-1441)*, pages 1–5, 2020.

[355] Xingshuo Li, Huiqing Wen, Yihua Hu, and Lin Jiang. A novel beta parameter based fuzzy-logic controller for photovoltaic mppt application. *Renewable Energy*, 130:416–427, 2019.

[356] Rahul Bisht and Afzal Sikander. An improved method based on fuzzy logic with beta parameter for pv mppt system. *Optik*, 259:168939, 2022.

[357] Claude Bertin Nzoundja Fapi, Patrice Wira, Martin Kamta, Abderrezak Badji, and Hyacinthe Tchakounte. Real-time experimental assessment of hill climbing mppt algorithm enhanced by estimating a duty cycle for pv system. *International Journal of Renewable Energy Research*, 9:1180–1189, 2019.

[358] Fekkak bouazza, Menaa Mohamed, Boussahoua Bouziane, and Djoudi Abdelhak. Photovoltaic generator modeling based on look up table approach and implementation on stm32f407 board of the perturb&observe algorithm based mppt. In *2018 International Conference on Applied Smart Systems (ICASS)*, pages 1–7, 2018.

[359] Mahmoud Aref, Ismaiel Ahmed, Vladislav Oboskalov, Anatolijs Mahnitko, and Aleksandrs Gavrilovs. Microcontroller look-up table of digital control mppt of pv system. In *2018 IEEE 59th International Scientific Conference on Power and Electrical Engineering of Riga Technical University (RTUCON)*, pages 1–5, 2018.

[360] Mustafa Engin Başoğlu and Bekir Çakir. An improved incremental conductance based mppt approach for pv modules. *Turkish Journal of Electrical Engineering and Computer Sciences*, 23:1687–1697, 1 2015.

[361] Linjuan Gong, Guolian Hou, and Congzhi Huang. A two-stage mppt controller for pv system based on the improved artificial bee colony and simultaneous heat transfer search algorithm. *ISA Transactions*, 132:428–443, 2023.

[362] R.W. Robinson, W.A. Cronje, and K.J. Nixon. The design of a hybrid mppt methodology to mitigate the effects of partial shading in pv systems. In *2022 30th Southern African Universities Power Engineering Conference (SAUPEC)*, pages 1–6, 2022.

[363] Shubhajit Roy Chowdhury and Hiranmay Saha. Maximum power point tracking of partially shaded solar photovoltaic arrays. *Solar Energy Materials and Solar Cells*, 94(9):1441 – 1447, 2010. PVSEC 18.

[364] Nora Kacimi; Said Grouni; Abdelhakim Idir; Mohamed Seghir Boucherit. New improved hybrid mppt based on neural network-model predictive control-kalman filter for photovoltaic system. *Institute of Advanced Engineering and Science*, Vol 20, No 3: December 2020, 2020.

[365] Khusnul Hidavat, Rini Nur Hasanah, and Hadi Suyono. Hybrid improved differential evolution and spline-based jaya for photovoltaic mppt technique. In *2019 6th International Conference on Electrical Engineering, Computer Science and Informatics (EECSI)*, pages 344–351, 2019.

[366] Vijay Muniyandi, Saravanan Manimaran, and Ashok Kumar Balasubramanian. Improving the Power Output of a Partially Shaded Photovoltaic Array Through a Hybrid Magic Square Configuration With Differential Evolution-Based Adaptive P&O MPPT Method. *Journal of Solar Energy Engineering*, 145(5), 01 2023. 051001.

[367] Ali Moghassemi, Shayan Ebrahimi, Sanjeevikumar Padmanaban, Massimo Mitolo, and Jens Bo Holm-Nielsen. Two fast metaheuristic-based mppt techniques for partially shaded photovoltaic system. *International Journal of Electrical Power & Energy Systems*, 137:107567, 2022.

[368] Dokala Janandra Krishna Kishore, Mohd Rusllim Mohamed, Kumarasamy Sudhakar, and Kurukuri Peddakapu. Grey wolf optimization and differential evolution-based maximum power point tracking controller for photovoltaic systems under partial shading conditions. *Energy Sources, Part A: Recovery, Utilization, and Environmental Effects*, 44(3):6286–6302, 2022.

[369] Dileep Krishna Mathi and Ramulu Chinthamalla. A hybrid global maximum power point tracking of partially shaded pv system under load variation by using adaptive salp swarm and differential evolution – perturb & observe technique. *Energy Sources, Part A: Recovery, Utilization, and Environmental Effects*, 43(20):2471–2495, 2021.

[370] Maykon Vichoski da Rocha, Leonardo Poltronieri Sampaio, and Sergio Augusto Oliveira da Silva. Comparative analysis of mppt algorithms based on bat algorithm for pv systems under partial shading condition. *Sustainable Energy Technologies and Assessments*, 40:100761, 2020.

[371] K Khalil Hassan et al. Nonlinear systems. *Departement of Electrical and computer Engineering, Michigan State University*, 2002.

[372] Joseph La Salle and Solomon Lefschetz. *Stability by Liapunov's Direct Method*. Academis Press Inc., 1962.